

Politecnico di Milano

Facoltà di Ingegneria Industriale

Corso di Laurea Magistrale in Ingegneria Aeronautica



**Non-modal stability of laminar channel
flow over porous walls**

Relatore: Prof. Maurizio Quadrio

Correlatore: Prof. Luca Cortelezzi

Tesi di laurea di:
Davide Scarselli
Matr. 765155

Anno Accademico 2011 - 2012

Contents

1	Introduction	1
2	Flow through porous media	7
2.1	Darcy's law	8
2.2	Volume Averaged Navies-Stokes	11
2.2.1	Darcy's law	15
2.2.2	LES analogy	16
2.3	Interface conditions	16
2.3.1	The Beavers and Joseph condition	18
2.3.2	The Brinkman condition	19
2.3.3	The momentum transfer conditions of Ochoa-Tapia and Whitaker	20
3	Problem definition	23
3.1	Non-dimensional equations	24
3.1.1	Navier-Stokes equations	24
3.1.2	Volume Averaged Navier-Stokes equations	24
3.1.3	Boundary and interface momentum transfer conditions	25
3.2	v - η formulation	25
3.2.1	Navier-Stokes equations	26
3.2.2	Volume Averaged Navier-Stokes equations	27
3.2.3	Boundary and interface momentum transfer conditions	28
4	Non-modal stability	31
4.1	Disturbances equations	31
4.1.1	Base flow	31
4.1.2	Linearized equations	32
4.1.3	Modal equations	34
4.2	Non-modal analysis	38
4.2.1	Energy of the disturbances	38
4.2.2	Maximum energy growth	39
4.3	Numerical implementation	40
4.3.1	Chebyshev collocation method	41

4.3.2	Error evaluation	46
4.3.3	Structure of the program	47
4.3.4	Validation	47
5	Results	51
5.1	A reference case	52
5.1.1	Maximum amplification in wavespace	52
5.1.2	Transient growth function	53
5.1.3	Optimal initial condition	57
5.2	Effects of permeability	59
5.3	Effects of the momentum transfer coefficient	61
5.4	Effects of porosity	63
6	Conclusions and future work	67
	Bibliography	75

List of Figures

2.1	Sketch of a porous medium with a wide range of length scales. l_f and l_s are the pore and particle diameters of the pore-like structures.	7
2.2	Filtration of water through a layer of sand.	8
2.3	Darcy's experiment data. The solid line are the fit of the experimental data.	9
2.4	Sketch of a porous layer.	10
2.5	Sketch of porous medium with position vectors.	11
2.6	Interface between a porous region and a purely fluid region.	17
2.7	Velocity profiles of the flow through a porous medium, not to scale. Figure (b) shows the velocity profile obtained with the Beavers and Joseph condition.	17
2.8	Fluid velocity profile at the interface between a porous region and a purely fluid region.	20
3.1	Sketch of the channel geometry.	23
4.1	Flowchart of the algorithm implemented in the program for the non-modal stability study.	48
4.2	For parameters $Re = 500$, $\alpha = 1$, $\beta = 1.5$, $h = 1$, $\varepsilon = 0.6$ and $\tau = 0$, (a) A comparison between the transient energy growth for channel flow over porous walls with $\sigma_1 = \sigma_2 = 0.02, 0.014, 0.008, 0.002$ (red solid line) and of Poiseuille flow at the same Reynolds number (black dashed line). (b) Corresponding values of δG .	49
5.1	For parameters $Re = 500$, $h_p = 1$, $\sigma = 0.0155$, $\varepsilon = 0.4$, $\tau = 0$, (a) contour levels of G^{max} for the flow over porous walls (red solid line) and Poiseuille flow at the same Reynolds number (black dotted line) and (b), corresponding contour levels of δG .	53
5.2	Spectrum for porous flow $Re = 500$, $\alpha = 1.3$, $\beta = 0.7$, $h_p = 1$, $\sigma = 0.0155$, $\varepsilon = 0.4$, $\tau = 0$ (red dots), and for Poiseuille flow at the same Reynolds number (black circles). (a) Upper part of the spectrum, with A, the 22nd mode. (b) Lower part of the spectrum, with coupling modes B and porous modes C.	54

-
- 5.3 A comparison between the the growth function $G_K(t)$ for $\text{Re} = 500$, $\alpha = 1.3$, $\beta = 0.7$, $h_p = 1$, $\sigma = 0.0155$, $\varepsilon = 0.4$, $\tau = 0$ (red solid line) with the one of Poiseuille flow at the same Reynolds number (black dash-dotted line). 54
- 5.4 For parameters $\text{Re} = 500$, $\alpha = 1.3$, $\beta = 0.7$, $h = 1$, $\sigma = 0.0155$, $\varepsilon = 0.4$, $\tau = 0$, (a) successive approximations of G^{max} obtained with increasing dimension K of the reduced base, comparison between flow over porous walls (red points), and Poiseuille flow at the same Reynolds number (black circles). (b) Corresponding values of δ_K . 55
- 5.5 Eigenfunctions of mode A, modulus (solid line), real part(dotted line) and imaginary part(dashed line). A comparison between the flow over porous walls, for $\text{Re} = 500$, $\alpha = 1.3$, $\beta = 0.7$, $h = 1$, $\sigma = 0.0155$, $\varepsilon = 0.4$, $\tau = 0$ (left column), and Poiseuille flow for at the same Reynolds number (right column). 56
- 5.6 Optimal initial condition, modulus (solid line), real part(dotted line) and imaginary part(dashed line). A comparison between flow over porous walls, for $\text{Re} = 500$, $\alpha = 1.3$, $\beta = 0.7$, $h = 1$, $\sigma = 0.0155$, $\varepsilon = 0.4$, $\tau = 0$ (left column), and Poiseuille flow at the same Reynolds number (right column). 58
- 5.7 For parameters $\text{Re} = 500$, $h = 1$, $\varepsilon = 0.4$, $\tau = 0$, (a) and (c) contours of G^{max} , with $\sigma = 0.0065, 0.02$, respectively. (b) and (d) contour levels of δG , with $\sigma = 0.0065, 0.02$, respectively. Red solid line denotes flow over porous walls, while black dash dotted line denotes Poiseuille flow at the same Reynolds number. The gray area marks the linearly unstable region. 60
- 5.8 For parameters $\text{Re} = 500$, $\alpha = 1.3$, $\beta = 0.7$, $h_p = 1$, $\varepsilon = 0.4$, $\tau = 0$, (a) the effects of permeability on the transient growth function, and (b), the effects of permeability on the modulus of the optimal initial normal velocity. Permeability are $\sigma = 0.0065$ (dotted line), $\sigma = 0.0155$ (solid line) and $\sigma = 0.02$ (dash-dotted line). 61
- 5.9 For parameters $h_p = 1$, $\varepsilon = 0.4$, the contour levels of G^{max} using $\tau = 0$ (solid line), $\tau = 1$ (dashed line) and $\tau = -1$ (dotted line). Shaded areas are linearly unstable regions for $\tau = -1$ (darkest gray), 0,1 (lightest gray). Permeability and Reynolds number are: (a) $\sigma = 0.0155$, $\text{Re} = 500$; (b) $\sigma = 0.0155$, $\text{Re} = 750$; (c) $\sigma = 0.02$, $\text{Re} = 500$; (d) $\sigma = 0.02$, $\text{Re} = 750$ 62
- 5.10 For parameters $\text{Re} = 500$, $\alpha = 1.3, \beta = 0.7$, $h_p = 1$, $\sigma = 0.0155$, $\varepsilon = 0.4$, (a) the effects of τ on the transient growth function, and (b), the effects of τ on the magnitude of the optimal initial normal velocity. The values of the interface coefficient are $\tau = -1$ (dotted line), $\tau = 0$ (solid line) and $\tau = 1$ (dashed line). 63

5.11	For parameters $h_p = 1$, $\tau = 0$, the contour levels of G^{max} using $\varepsilon = 0.4$ (solid line), $\varepsilon = 0.8$ (dashed line) and $\varepsilon = 0.3$ (dotted line). Shaded areas are linearly unstable regions for $\varepsilon = 0.3$ (lightest gray), $0.4, 0.8$ (darkest gray). Permeability and Reynolds number are: (a) $\sigma = 0.0155$, $Re = 500$; (b) $\sigma = 0.0155$, $Re = 750$; (c) $\sigma = 0.02$, $Re = 500$; (d) $\sigma = 0.02$, $Re = 750$	64
5.12	For parameters $Re = 500$, $\alpha = 1.3, \beta = 0.7$, $h_p = 1$, $\sigma = 0.0155$, $\tau = 0$, (a) the effects of the porosity on the transient growth function, and (b), the effects of the porosity on the magnitude of the optimal initial normal velocity. The values of the porosity are $\varepsilon = 0.3$ (dotted line), $\varepsilon = 0.4$ (solid line) and $\varepsilon = 0.8$ (dashed line).	65

List of Tables

2.1	Some typical values of permeability taken from [2].	10
2.2	Some typical values of permeability together with the coefficient α_{BJ} determined experimentally by Beavers and Joseph [3], and the momentum transfer coefficient τ determined by Ochoa-Tapia and Whitaker [30] assuming $\varepsilon = 0.4$	18

Abstract

We perform a non-modal stability analysis of a fully-developed and laminar flow of an incompressible fluid through a channel bounded by flat, homogeneous, isotropic porous layers. We model the flow in the purely fluid region using the Navier-Stokes equations, and the flow through the porous layers using a volume-averaged version of the Navier-Stokes equations derived by Whitaker (1994). We restrict our study to flows through porous materials in which inertial effects can be considered negligible. We assume an exponential temporal dependence of the perturbations and derive the modal equations. We discretize the modal equations by means of the Chebyshev collocation spectral method, solve the related linear stability problem, and compute the maximum energy amplification among all the possible perturbations. We use an adaptive algorithm to carry out a parametric study in which we vary Reynolds number, streamwise and spanwise wavenumbers, permeability, porosity and a coefficient which represents the momentum transfer process at the interface between the fluid region and the porous material. We validate our methodology by comparing our eigenvalues with the ones reported by previous linear stability studies, as well as by recovering the transient energy growth of the plane Poiseuille flow, in the limit of zero permeability. We report that in well defined regions of the wavenumber space, permeability can increase the maximum value of the energy growth up to 40% with respect of plane Poiseuille flow. We show that this increase is associated to an optimal initial condition in which there is a significant flow across the interface. Moreover, we discover that the modes associated with the equations governing the fluid motion in the porous layers and with the momentum transfer conditions, do not contribute significantly to reported amplification of the maximum value of the energy growth function. We find that porosity and momentum transfer coefficient have a weaker influence on the transient growth than permeability does, while they alter significantly the linearly unstable regions in the wavenumber space.

Key Words

Transient growth - Non-modal Stability - Porosity - Permeability

Sommario

Si effettua uno studio sulla stabilità non modale di un flusso incomprimibile, laminare e stazionario che attraversa un canale piano, indefinito e delimitato da pareti in materiale poroso. Il mezzo poroso è permeabile ed è caratterizzata da una porosità omogenea e isotropa. Si modella il comportamento del flusso nella regione puramente fluida con le equazioni di Navier-Stokes, mentre il flusso negli strati porosi viene modellato con le equazioni di Navier-Stokes mediate nel volume, derivate da Whitaker (1994). In questa tesi si considerano solo flussi in materia porosa in cui è lecito trascurare il contributo dei termini inerziali. Si considerano perturbazioni con forma d'onda spaziale, che dipendono dal tempo tramite un esponenziale complesso e si derivano le equazioni modali. Si discretizzano le equazioni modali utilizzando il metodo spettrale di Chebyshev, si risolve numericamente il conseguente problema agli autovalori e si calcola la funzione di crescita transitoria, dalla quale si estrae il valore massimo. Si usa un algoritmo adattivo per fare uno studio parametrico nel quale si sono variati il numero di Reynolds, i numeri d'onda delle perturbazioni, la permeabilità, la porosità e il coefficiente che modella lo scambio di quantità di moto all'interfaccia tra regione fluida e strato poroso. Si valida il programma sia confrontando gli autovalori con quelli riportati da studi precedenti sulla stabilità lineare, sia recuperando la crescita transitoria per il flusso nel canale piano, nel limite di permeabilità tendente a zero. Si riporta che per determinati valori dei numeri d'onda delle perturbazioni, la presenza di pareti permeabili è in grado di amplificare fino al 40% il massimo della crescita transitoria, rispetto al canale piano con pareti impermeabili. Si mostra che questa amplificazione è associata ad una condizione ottima iniziale in cui è presente un considerevole flusso che attraversa lo strato poroso in direzione normale. Si riporta che la porosità e il coefficiente di scambio di quantità di moto modificano il massimo della crescita transitoria in maniera meno incisiva della permeabilità, mentre modificano significativamente le regioni linearmente instabili nello spazio dei numeri d'onda.

Parole Chiave

Crescita transitoria - Stabilità non modale - Porosità - Permeabilità

Estratto della tesi in lingua italiana

Questo studio è giustificato dal crescente interesse verso i materiali porosi in molti campi della fisica, che spaziano dalla ricerca pura ad applicazioni ingegneristiche. Tra i fenomeni naturali in cui vi è un'interazione tra fluido e materia porosa troviamo, ad esempio, i flussi sotterranei attraverso rocce sedimentarie, lo scorrimento di acqua sopra gli alvei dei fiumi o sui fondali marini, e anche flussi in tessuti organici come arterie, vene e polmoni. Esempi di applicazioni tecnologiche che coinvolgono mezzi porosi sono l'estrazione di petrolio dai giacimenti, lo studio della penetrazione di inquinanti all'interno di falde acquifere, sistemi di riscaldamento che sfruttano la porosità per migliorare la capacità di scambio termico di un materiale, i processi di filtraggio, in cui la materia porosa è usata per separare le diverse fasi di un fluido e l'uso di pareti traspiranti per il controllo di vene fluide.

Vi è evidenza sperimentale (Beavers et al. 1970, Sparrow et al. 1973) che dimostra che l'uso di pareti permeabili, piuttosto che impermeabili, può indurre il flusso nel canale piano a manifestare una transizione anticipata al regime turbolento. Per la precisione, Beavers *et al.* [4], e Sparrow *et al.* [46] hanno studiato sperimentalmente la transizione per un flusso laminare, parallelo, unidirezionale in un canale delimitato da pareti piane, delle quali una è porosa, e hanno dimostrato che il numero di Reynolds critico si riduce considerevolmente rispetto al canale con due pareti impermeabili. Inoltre, Sparrow *et al.* hanno confermato numericamente, con un'analisi di stabilità lineare bidimensionale, che la presenza di una parete permeabile ha un forte effetto destabilizzante. Tilton e Cortelezzi hanno sviluppato ulteriormente questo lavoro, eseguendo un'analisi di stabilità lineare tridimensionale di un canale delimitato da due pareti rigide, e caratterizzate da una porosità omogenea e isotropa [50, 51]. Nel dettaglio, essi hanno fatto uno studio parametrico nel quale hanno variato i parametri che modellano il flusso negli strati porosi, e hanno mostrato che piccoli valori di permeabilità sono sufficienti ad abbassare il numero di Reynolds critico del 90% rispetto al medesimo flusso tra pareti impermeabili. Un altro campo in cui la permeabilità di una parete ha mostrato effetti destabilizzanti, è l'aspirazione asintotica di strato limite. Tilton ha studiato la stabilità lineare di uno strato limite laminare completamente sviluppato su una parete permeabile, soggetto ad aspirazione costante lungo tutta la parete [49]. Tilton ha dimostrato che il numero di Reyn-

olds critico ricavato in studi analoghi in cui veniva trascurata la porosità, può ridursi fino al 20%. Le superfici porose hanno un notevole impatto anche su i flussi turbolenti. Breugem and Boersma [9, 10], e Breugem *et al.* [11, 12] hanno effettuato numerose simulazioni di flusso turbolento in canali con pareti porose simulate attraverso grigli di cubi, e hanno mostrato che l'uso di superfici permeabili determina notevoli aumenti nella resistenza e negli sforzi locali.

Questi risultati aprono diverse possibilità di impiego dei materiali porosi in applicazioni che coinvolgono problemi di transizione e turbolenza. Citiamo ad esempio il controllo attivo delle caratteristiche di una vena fluida, meccanismi per anticipare o ritardare la transizione, utilizzati per migliorare la similitudine dinamica in galleria del vento, il miglioramento delle capacità di mescolamento di un flusso, la laminarizzazione di un flusso per evitare la separazione. In quest'ottica, il nostro lavoro mira a contribuire nell'indagine delle dinamiche che regolano la transizione alla turbolenza di flussi su pareti porose, in modo da fornire uno scenario più completo a ricercatori e ingegneri coinvolti nelle sopracitate applicazioni.

In questo lavoro si studia numericamente la stabilità non modale di un flusso viscoso, incomprimibile, uniforme, parallelo e laminare che attraversa un canale delimitato da pareti piatte caratterizzate da porosità omogenea e isotropa. Si è fatto uno studio parametrico nel quale si è calcolato il massimo della crescita transitoria dell'energia delle perturbazioni sovrapposte al flusso laminare. Per particolari scelte dei parametri, si discutono gli effetti che i parametri del materiale poroso hanno sulla crescita transitoria e sulla condizione iniziale ottima che genera il valore massimo.

Un'analisi di stabilità lineare consiste nello studiare il comportamento asintotico di perturbazioni sovrapposte ad un flusso base laminare. Se le perturbazioni sono sufficientemente piccole, le equazioni di governo possono essere linearizzate, così da ottenere equazioni lineari per le perturbazioni. In seguito si trasforma il problema secondo Fourier, si assume che l'ampiezza delle perturbazioni dipenda dal tempo tramite un esponenziale complesso e infine si scrive il conseguente problema agli autovalori. Se sono presenti autovalori per i quali la parte reale delle perturbazioni diverge temporalmente, allora il flusso base è definito instabile. Questo tipo di approccio presenta il limite di considerare solamente il comportamento delle perturbazioni con orizzonte temporale infinito. Infatti, è noto che per problemi, tra i quali quello del flusso nel canale piano indefinito, i disturbi possono subire una crescita transitoria prima di decadere [19, 37, 38]. Se tale crescita è considerevole, allora le perturbazioni possono essere sufficientemente grandi da rendere importanti i termini non lineari che erano stati trascurati, invalidando l'analisi di stabilità lineare. L'analisi di stabilità non modale studia l'evoluzione temporale della massima amplificazione dell'energia cinetica delle perturbazioni, tra tutte le condizioni iniziali possibili. Questo tipo di analisi è in grado di mostrare se sono presenti dinamiche che potrebbero instabilizzare il flusso base, sebbene al di sotto della soglia del numero di Reynolds critico della stabilità

lineare.

I materiali porosi hanno una struttura interna molto complicata, che rende proibitivo una simulazione esatta del moto fluido al loro interno, sia per l'elevato onere computazionale, sia per la difficoltà di rappresentare numericamente un dominio complicato. Un primo approccio per superare questa difficoltà consiste nel ridurre gli effetti della parete porosa ad un'adeguata condizione al bordo, come effettuato negli studi di Hahn *et al.*, in cui è stata effettuata una simulazione di un flusso turbolento in un canale con pareti porose modellate imponendo nulla solo la componente normale di velocità a parete [21], e quelli di Wagner e Friedrich, nei quali è stato simulato il flusso turbolento in un tubo con parete porosa, imponendo che sul bordo le velocità tangenti fossero nulle [54]. Questi approcci, sebbene computazionalmente economici, hanno lo svantaggio di perdere informazioni sul moto fluido all'interno dello strato poroso, e di come questo interagisca con la vena fluida soprastante. In letteratura si trovano altre due soluzioni. La prima consiste nel simulare numericamente il flusso all'interno dello strato poroso, che viene modellato con una geometria estremamente semplificata, ad esempio, reticoli di cubi, cilindri e sfere [60, 27, 9, 10, 11, 12]. La seconda soluzione consiste nel modellare matematicamente il moto all'interno dello strato poroso. Whitaker propone un modello basato sulle equazioni di Navier-Stokes mediate su volumi sufficientemente piccoli rispetto alle dimensioni macroscopiche del mezzo poroso, e sufficientemente grandi rispetto alle scale che caratterizzano la complicata microstruttura [55, 56, 57]. Il risultato delle operazioni di media genera un contributo di resistenza all'avanzamento del fluido e un contributo che esprime la resistenza dovuta ad effetti inerziali. Questo ultimo termine non è in forma chiusa e deve essere modellato in base alla struttura interna del materiale poroso. Per semplificare le equazioni si adotta l'ipotesi di materiale con porosità omogenea e isotropa, ed inoltre si ritiene che la permeabilità sia sufficientemente piccola da poter trascurare gli effetti inerziali. Con queste ipotesi, le equazioni di Whitaker assumono una forma chiusa, e possono essere accoppiate con le equazioni di Navier-Stokes, a patto di porre opportune condizioni all'interfaccia che modellino lo scambio di quantità di moto.

In questo lavoro si modella il flusso nella regione centrale del canale utilizzando le equazioni di Navier-Stokes per un fluido viscoso e incomprimibile, e il flusso negli strati porosi utilizzando le equazioni di Navier-Stokes mediate nel volume derivate da Whitaker, sotto l'ipotesi di porosità omogenea e isotropa, e di effetti inerziali trascurabili. Le velocità mediate nel volume soddisfano la condizione di perfetta adesione sulle pareti e sono accoppiate alle grandezze della regione puramente fluida dalle condizioni di interfaccia di Ochoa-Tapia e Whitaker [29, 30, 31]. Si definisce come lunghezza di riferimento la semi altezza della regione fluida del canale, e come velocità di riferimento la velocità media del flusso base all'interno del canale. Successivamente, si adimensionalizzano le equazioni e le condizioni al bordo, si riscrivono le medesime nelle variabili di velocità e vorticità normali al canale, e si ricavano le equazioni linearizzate per le perturbazioni, assumendo il

profilo base laminare derivato da Tilton e Cortelezzi [51]. La geometria indefinita del canale permette di esprimere le perturbazioni in forma d'onda nelle direzioni parallela e trasversale al flusso. Si assume che l'ampiezza delle perturbazioni dipenda dal tempo tramite un esponenziale complesso, permettendo di riscrivere le equazioni di governo e le condizioni al contorno in forma modale, l'insieme delle quali costituisce un problema agli autovalori generalizzato, in cui la frequenza temporale delle onde è l'autovalore. Successivamente, si presenta la metodologia alla base dell'analisi di stabilità non modale. Si definisce l'energia cinetica delle perturbazioni per unità di apertura e di lunghezza del canale, il prodotto scalare associato e la conseguente norma indotta, e infine si scrive la definizione della funzione di crescita transitoria. Successivamente si discute la formulazione discreta del problema. Si esprimono le perturbazioni tramite un'espansione finita di polinomi di Chebyshev, e si collocano le equazioni di governo per ciascuno strato su una griglia di nodi di Gauss-Lobatto. Si assembla il problema agli autovalori discreto e si spiega la metodologia per l'imposizione delle condizioni al bordo e all'interfaccia. Infine si discute il programma adattivo usato per studiare il massimo della crescita transitoria nello spazio dei parametri. Nel dettaglio, il programma è in grado di scegliere il numero di polinomi di Chebyshev e la dimensione del sottospazio dei modi del problema agli autovalori necessari a calcolare la crescita transitoria in modo che soddisfi una certa tolleranza sull'errore fissata a priori.

In questa tesi si è preso in considerazione un canale delimitato da due strati porosi identici. Nello studio parametrico effettuato sono stati fatti variare il numero di Reynolds Re , i numeri d'onda longitudinale e trasversali, rispettivamente α e β , la permeabilità adimensionale σ , la porosità ε e il coefficiente che modella lo scambio di quantità di moto all'interfaccia τ . Per ciascun caso è stato calcolato il massimo G^{max} della funzione di crescita transitoria $G(t)$. Data la natura 6-dimensionale dello spazio dei parametri, è possibile tracciare l'andamento della funzione $G^{max}(Re, \alpha, \beta, h_p, \sigma, \varepsilon, \tau)$ fissando almeno tre parametri alla volta. In questa tesi si è tracciata la funzione $G^{max}(\alpha, \beta)$ per permettere il confronto con il canale piano con pareti impermeabili, e in questo spazio si è studiata l'influenza degli altri parametri.

Si presentano i risultati prendendo in considerazione il caso di riferimento $Re = 500$, $h_p = 1$, $\sigma = 0.0155$, $\varepsilon = 0.4$, $\tau = 0$. Si introduce la differenza δG , tra il valore di G^{max} nel del nostro problema e quella del flusso di Poiseuille, normalizzata rispetto a questo ultimo. Nel complesso, si riporta che, nello spazio dei numeri d'onda considerato $(\alpha, \beta) \in [0, 2] \times [0, 4]$, la presenza di pareti permeabili amplifica la crescita transitoria, fino ad un massimo del 40%, localizzato nel punto $\alpha = 1.3$, $\beta = 0.7$. Per questo punto si confronta la crescita transitoria $G(t)$ con quella del canale impermeabile, e si discute il numero di modi da includere nella base ridotta necessari per calcolare accuratamente $G(t)$. Si rileva che non è necessario includere né i modi associati agli strati porosi, né quelli associati alle condizioni di interfaccia. Infine, si costruisce la condizione iniziale ottima che

genera G^{max} . Si osserva che il profilo della velocità normale ottima assume valori all'interfaccia dello stesso ordine di grandezza di quelli vicino alla regione centrale del canale fluido, mentre il profilo della velocità normale rimane pressoché inalterato, rispetto al canale con le pareti impermeabili.

Si è variata la permeabilità delle pareti mantenendo costanti $h_p = 1$, $\varepsilon = 0.4$, $\tau = 0$ e si è rilevato che per $\sigma = 0.0065$ la massima amplificazione δG diminuisce al 7% ed è localizzata ancora in $\alpha = 1.3, \beta = 0.7$, mentre per $\sigma = 0.02$ il flusso diventa linearmente instabile, e si raggiungono massimi con $\delta G = 80\%$. Per il punto ($\alpha = 1.3, \beta = 0.7$) si costruisce la condizione iniziale ottima e si osserva che la permeabilità modifica considerevolmente il valore che la velocità normale assume all'interfaccia.

Si discutono gli effetti del coefficiente di scambio di quantità di moto rispetto al caso con $h_p = 1$, $\sigma = 0.0155$, $\varepsilon = 0.4$, $\tau = 0$. Teoricamente, Ochoa-Tapia e Whitaker hanno stimato che $|\tau| \approx 1$ [29], tuttavia esso rimane da determinarsi sperimentalmente. Perciò si è deciso di fare variare τ nell'intervallo $[-1,1]$ per ottenere una banda di dispersione dei dati. Si è osservato che il coefficiente d'interfaccia ha un impatto su G^{max} di minore importanza rispetto alla permeabilità. La banda di dispersione aumenta con il numero d'onda α , e globalmente nello spazio dei numeri d'onda aumentando il numero di Reynolds o la permeabilità. Il maggiore contributo alla dispersione è dato passando da $\tau = 0$ a $\tau = 1$. Il coefficiente τ modifica la stabilità lineare del canale. In particolare, per $\tau = 1$ la regione instabile nello spazio dei numeri d'onda è meno estesa rispetto al caso con $\tau = 0$, mentre quella risultante da $\tau = -1$ è sostanzialmente coincidente con quella ottenuta usando $\tau = 0$. Infine, osservando la condizione iniziale ottima per ($\alpha = 1.3, \beta = 0.7$), si rileva che τ modifica in modo trascurabile il valore della velocità all'interfaccia.

Gli effetti della porosità vengono discussi rispetto al caso con $h_p = 1$, $\sigma = 0.0155$, $\varepsilon = 0.4$, $\tau = 0$. Osservando le curve di livello per $\varepsilon = 0.3, 0.4, 0.8$, si constata che il valore di G^{max} subisce cambiamenti in misura inferiore rispetto a quanto osservato con il coefficiente τ . Anche per la porosità, si osserva che gli effetti sul massimo della crescita transitoria aumentano con l'aumentare del numero d'onda α , e nel complesso si intensificano con l'aumentare della permeabilità e del numero di Reynolds. Si rileva che la porosità è in grado di modificare le proprietà di stabilità lineare. Nel dettaglio, la regione dello spazio dei numeri d'onda linearmente instabile si estende aumentando il valore della porosità. Analizzando la condizione iniziale ottima per ($\alpha = 1.3, \beta = 0.7$), si constata che maggiori valori di porosità determinano maggiori valori del profilo di velocità normale ottima all'interfaccia.

In questo lavoro è stata fatta l'ipotesi che gli effetti inerziali fossero trascurabili. Seguendo Tilton e Cortelezzi [51], un criterio per verificare la legittimità dell'ipotesi è controllare che $u_i < 0.05$, essendo u_i la velocità adimensionale del flusso base all'interfaccia. Nei casi discussi in questa tesi, il vincolo è stato sempre rispettato, con l'eccezione di $\tau = 1$ e $\varepsilon = 0.4$, quando $\sigma = 0.0155, 0.02$, dove

$u_i = 0.069, 0.096$, rispettivamente. Tuttavia, come è stato mostrato sperimentalmente da Costa *et al.*, gli effetti inerziali diventano importanti in modo graduale con l'aumentare della velocità del flusso negli strati porosi o della permeabilità [14]. Pertanto, il criterio sopra menzionato è da considerarsi in linea di massima, essendo difficile definire un valore critico per u_i .

Questa tesi ha mostrato che, in ben precise zone dello spazio dei numeri d'onda, la crescita di energia transitoria di un flusso che scorre in un canale con pareti porose e permeabili è superiore a quanto accade per il caso in cui si le pareti sono impermeabili. Questo incremento è collegato ad un significativo flusso che attraversa normalmente l'interfaccia che separa lo strato poroso da quello puramente fluido. Se l'energia, prima di decadere, raggiunge un livello tale da rendere importanti i termini non lineari, i risultati dell'analisi lineare possono non essere più validi, e si possono innescare meccanismi di transizione al flusso turbolento. Si confida che quanto riportato in questo lavoro possa contribuire a migliorare la comprensione dei fenomeni che innescano la transizione di un flusso che scorre sopra una superficie porosa, e che inoltre, possa avere risvolti in applicazioni tecnologiche quali il controllo di strato limite laminare mediante aspirazione. Braslow riporta l'uso tecniche di aspirazione di strato limite in ambito aeronautico in cui venivano usate superficie forate o inserti porosi veri e propri [8]. Si cita inoltre un brevetto per il controllo della qualità della vena fluida in galleria del vento che utilizza un dispositivo di aspirazione tramite strato poroso [6]. Lo sviluppo di queste tecnologie è effettuato principalmente in modo sperimentale. Si confida nell'utilità di questa analisi di stabilità nel migliorare le stime numeriche del numero di Reynolds al quale avviene la transizione, così da limitare i costi delle campagne sperimentali.

A causa dell'elevato numero di parametri implicati nel modellare il problema considerato, si sono considerati solo casi simmetrici, e inoltre, l'altezza dello strato poroso non è stata variata. Inoltre, si sono studiati gli effetti della porosità e del coefficiente di scambio di quantità di moto all'interfaccia separatamente. Sviluppi futuri dovrebbero concentrarsi su una più profonda esplorazione dello spazio dei parametri, e sullo studio di come essi agiscono sulla stabilità non modale quando sono variati simultaneamente. Poiché in questo lavoro si sono considerati solo flussi in materia porosa in cui gli effetti inerziali fossero trascurabili, i materiali ad alta porosità sono esclusi. Un possibile sviluppo di questa ricerca potrebbe essere l'introduzione di questi effetti almeno nelle condizioni al contorno, poiché è noto che gli effetti inerziali diventano importanti prima nell'interfaccia con la vena fluida, piuttosto che nello strato poroso [49].

Chapter 1

Introduction

This work is the result of a collaboration between myself, Mr. Marco Edoardo Rosti, Professor Maurizio Quadrio of the Politecnico di Milano and Professor Luca Cortelezzi of McGill university, who visited the Politecnico di Milano during a sabbatical leave.

We investigate the stability of a fluid flow over porous walls because of the increasing interest in such materials in many research fields, ranging from theoretical physics to engineering applications. Porous materials are involved in many natural phenomena, for example, fluid flows through sedimentary rocks, such as sandstones, conglomerates and shales, and over seabeds and riverbeds. Many organic tissues are porous, and the mass transfer processes between blood, air and tissue occur over their surfaces. Properties of such materials have also attracted the attention of engineers because of their potential applications. Relevant examples of engineering applications are the extraction of oil from ground reservoirs, management of water ground basins and filtration of pollutants through aquifers, transpiration cooling (in which the porosity is used to enhance the heat exchange capability of the material), filtration processes used to separate solids from fluids, and the use of wall transpiration to control of wall-bounded flows, such as laminar boundary layers over wings.

There is experimental evidence (Beavers *et al.* 1970, Sparrow *et al.* 1973) that shows that permeable walls can induce a channel flow to experience an anticipated transition to turbulence, with respect of the same flow over impermeable surfaces. More precisely, Beavers *et al.* [4], and Sparrow *et al.* [46], investigated experimentally the transitional behavior of a parallel, unidirectional, fully developed laminar flow in a channel bounded by flat walls, one of whose is a porous wall, and they discovered that transition occurs at lower critical Reynolds number, with respect to the case characterized by two impermeable walls. In addition, Sparrow *et al.* compared their experimental data with the predictions resulting by a two-dimensional linear stability analysis [46]. They used Darcy's law to model the flow in the porous region, and the Beavers and Joseph (1967) condition to couple the flow at the interface between the fluid and the porous

layer. They confirmed numerically that permeability linearly destabilize the flow, lowering the critical Reynolds number. Tilton and Cortelezzi performed a three-dimensional linear stability analysis of a fully-developed, laminar flow bounded by two flat, rigid, homogeneous and isotropic permeable walls [50, 51]. More precisely, they carried out a parametric study where parameters that model the porous medium are varied simultaneously. By considering permeable walls, they found that the critical Reynolds number can drop to the 10% of the corresponding value for the plane Poiseuille flow. Another field in which wall permeability has been showing a strong effect is the asymptotic suction boundary layer. Tilton studied the linear stability of a parallel, fully-developed, laminar velocity profile over a rigid, homogeneous and isotropic porous surface, and subjected to constant aspiration [49]. In order to model the suction, a semi-infinite, plenum chamber is located above the porous walls and it is maintained at a constant pressure lower than the free-stream one. Tilton found that the wall permeability can reduce up to the 20% the critical Reynolds number, with respect to previous studies on the asymptotic suction boundary layer. Porous materials influence also turbulent flows. Breugem and Boersma [9, 10], and Breugem *et al.* [11, 12], have performed many turbulent simulations modelling the porous layers with grid of cubes, and they showed that drag and local stresses considerably increase with respect the same flow over a flat an impermeable wall.

These results suggest that porous materials may play a significant role in applications involving transition and turbulence, such as flow control, drag reduction and increase, transition triggering and delaying, and enhancing mixing properties of turbulent flow. In this perspective, our study aims to achieve a better understanding of the instability and transition phenomena that occur when considering flows over porous media, and provide knowledge for researches who are interest in technology and applications that involve these materials.

In this work we investigate numerically the non-modal stability of a uniform, parallel, fully-developed laminar flow of an incompressible fluid through a channel bounded by flat, homogeneous, isotropic porous layers. We perform a parametric study in which we compute the maximum possible energy amplification of disturbances superimposed to the base flow. For significant parameter choices, we discuss how the parameters of the porous material modify the maximum value of the transient growth and the optimal initial condition.

In nature, there are many flows, such as jets, mixing layers, natural convection circulations and shear flows, which exhibit a great sensitivity to external disturbances. More precisely, when perturbations are sufficiently large, fluid motion deviates from an ordered and well defined state, the laminar flow, to a more complex behavior, which is referred to as turbulence. Turbulent flows are characterized by unpredictable and unsteady changes of local physical quantities, and moreover, they show very good mixing properties and a huge increase of the drag experienced by bodies moving through such flows. Fluid dynamics stability theory investigates why and how laminar flows undergo transition to turbulence.

The first scientific approach to hydrodynamic stability is experimental, and it is acknowledged to Reynolds [39]. In his famous experiment, he studied the transition of pipe flow by introducing a liquid dye through the inlet of the pipe. The transition occurred when the dye streak experienced a sudden break down, resulting in a chaotic motion and mixing with the other fluid. Reynolds observed that transition depends on the magnitude of the disturbance and the flow rate considered. Moreover, he introduced a non-dimensional parameter, the so called Reynolds number, to distinguish stable from unstable flows. Theoretically, Rayleigh was the first to establish a criterion to determine the stability properties of a base flow [36]. In particular, he considered a uniform, parallel and inviscid flow through an indefinite channel, and he found that unstable velocity profiles must have an inflection point. Orr and Sommerfeld developed further the Rayleigh's model and formulate the viscous stability problem for shear flows [32, 45]. These works were based on a technique, the so called normal-mode analysis, which studies the stability of the initial value problem arising from the linearized equations that govern the hydrodynamic problem. In particular, the normal-mode analysis assumes wave-like disturbances which depend exponentially on time, and then reformulates the initial value problem as an eigenvalue problem. The eigenvalues are related to the growth rate of the perturbations and the base flow is said to be unstable if there exists an eigenvalue that lies in the unstable complex semi-plane. Orszag succeeded in computing precisely and economically the eigenvalues for plane Poiseuille flow [33], allowing for an accurate prediction of the critical Reynolds number. However, the normal-mode analysis is limiting, because it focuses on the asymptotic behavior of the perturbations only, while it has been acknowledged that disturbances can experience a short-time significant growth, which can be sufficiently large to make the neglected non-linear terms important [19, 37, 38]. Non-modal stability analysis consists in computing the maximum amplification of the perturbation energy, for all the possible non-zero initial conditions. This method, differently from the normal-mode analysis, does not allow for a precise definition of stable or unstable flows, because there is no critical energy amplification over which transition occurs. However, the non-modal stability analysis provides a better understanding of the mechanisms that cause transition for many wall bounded shear flows, including the flow over porous walls.

Porous medium have a complicated internal structure that makes prohibitive to simulate the fluid motion inside the medium, because the huge computational cost and the difficulty in representing numerically complex domains. Therefore, different approaches have been developed to avoid the above mentioned problems. First, we can reduce all the effects induced by the presence of the porous layers to an adequate boundary condition. This method is the simplest and allow for simple and economical computations, since one does not have to consider the fluid inside the porous region. Hahn *et al.* performed a direct numerical simulation of turbulent channel over porous walls flow using a boundary condition which sets

to zero the wall-normal velocity components [21]. On the contrary, Wagner and Friedrich studied a turbulent pipe flow over permeable walls using a permeability condition for the radial velocity component and no-slip conditions for the other two velocity components [54]. The above-mentioned methods simulate the effects of permeability and they do not provide any information about the fluid motion in the porous layer. At this point, in literature we find two completely different alternatives to model the flow through the internal structure of porous materials. On one hand, we have numerical simulations of flows over porous surfaces modeled as grids of geometrically simple elements, such as cylinders, cubes, and spheres [60, 27, 9, 10, 11, 12]. On the other hand, we have mathematical equations modeling the flow through the medium. In Whitaker's volume-averaged Navier Stokes equations [55, 56, 57], the porous medium is treated as a continuum, so that fluid quantities are locally defined independently of the liquid or solid phase. Whitaker introduces a procedure consisting in averaging the microscopic flow field over a small spatial volume, resulting in an averaged macroscopic flow field. At the interface between the fluid region and the porous medium, velocity and pressure are continuous and must satisfy to relations which couple the Navier-Stokes equations with the Volume-Averaged Navier-Stokes.

Organization of the thesis

Chapter 2 provides a review of the theory of flow through porous media pertinent to our work. We explain the reasons that discourage to model in detail the flow through a porous medium, and in addition, we present the main models that have been developed in order to describe such a complex flow. More precisely, we discuss Darcy's law and we derive the Volume-Averaged Navier-Stokes equations. Next, we present a review of the conditions which couple the fluid quantities at the boundary between the fluid and porous region.

Chapter 3 presents the equations and the conventions used in the subsequent parts of this thesis. We first define precisely the geometry of our problem, together with the reference length and velocity. Then, we make the governing equations and the related boundary conditions non-dimensional, and finally, we reformulate our problem in terms of normal velocity and normal vorticity.

In chapter 4 we present the methodology concerned with non-modal stability analysis. We first define the laminar flow and then we derive the linearized equations for the disturbances. Next, we exploit the periodicity in the stream-wise and spanwise direction of the channel to rewrite our problem in wavenumber space and then, we derive the modal equations by assuming that the disturbances depend exponentially on time. Subsequently, we define the kinetic energy of the perturbations for the layered geometry of the channel, and the related transient growth function. Next, we introduce the Chebyshev collocation spectral method, and we derive the discretized version of the modal equations. Also, we present

the adaptive algorithm that we used to explore the parameter space, together with the errors used to control the accuracy of our results. Finally, we validate our program by recovering the energy growth function of the plane Poiseuille problem, as the permeability approximates zero.

In chapter 5 we present the results obtained for selected parameter combinations. We start presenting our results by focusing on a representative point of the parameter space, to allow us for significant comparisons when we vary the parameters. For this point, we follow the standard practice to plot the contour levels of the maximum of the transient growth as a function of the streamwise and spanwise wavenumbers. Subsequently, we discuss the effects that permeability, interface momentum transfer coefficient and porosity have on the non-modal stability.

Chapter 6 summarizes the results. We briefly review the methodologies used throughout this thesis and we report the most significant results. We discuss the validity of the hypotheses underlying the model equations and finally, we present some technological implications of this thesis and possible future work.

As a consequence of the collaboration with Mr. Rosti, my thesis shares two chapters with his thesis. In particular, the review of flow through porous media, performed in Chapter 2, and the definition of the mathematical model of the flow over porous media, presented in Chapter 3, are in common.

Chapter 2

Flow through porous media

This chapter succinctly reviews the theory of flow through porous media. The flow of an incompressible viscous fluid within the pore-like structure of a porous medium is governed by the Navier-Stokes equations

$$\frac{\partial \mathbf{u}}{\partial t} + \nabla \cdot (\mathbf{u} \otimes \mathbf{u}) = -\frac{1}{\rho} \nabla p + \nu \nabla^2 \mathbf{u}, \quad (2.1)$$

$$\nabla \cdot \mathbf{u} = 0, \quad (2.2)$$

with no-slip and no-penetration boundary conditions on the solid surfaces and an appropriate initial condition, where \mathbf{u} is the velocity, p the pressure, ρ the density and ν the kinematic viscosity of the fluid, respectively.

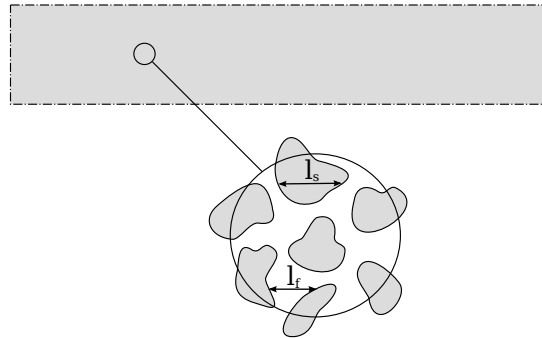


Figure 2.1: Sketch of a porous medium with a wide range of length scales. l_f and l_s are the pore and particle diameters of the pore-like structures.

In general, porous media have very complex structure which is not known in full details. Therefore, in most cases, the boundary conditions are nearly impossible to impose. Secondly, the flow inside a porous medium is characterized by a wide range of length scales, see figure 2.1. Porous media can be sponge-like porous foams and porous layers of packed particles. The smallest scales, l_f and l_s , represent the pore and particle diameters of the pore-like structures, while the

largest scale is the characteristic macroscopic porous length L . These aspects make prohibitively difficult and costly a direct numerical simulation of flows in porous medium. Consequently, in order to study these kind of flows, different techniques have been proposed so far.

2.1 Darcy's law

One of the first studies on flow through porous media was published by Darcy in 1856 [16]; he investigated the flow of water filtering through a layer of sand, in connection with the fountains of the city of Dijon in France, as illustrated in figure 2.2. He concluded that, for creeping flows, the average flow rate passing

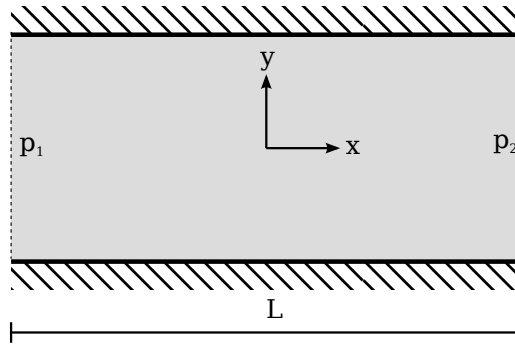


Figure 2.2: Filtration of water through a layer of sand.

through a layer of sand is proportional to the pressure gradient across the layer. Based on the result of his experiments, he proposed the following relation

$$Q = -kA \frac{p_2 - p_1}{\rho g L}, \quad (2.3)$$

where Q is the volumetric flow rate through the layer, A is the cross sectional area normal to the flow, g the gravitational acceleration, p_1 and p_2 the measured pressures, L the length of the sand layer over which the pressure difference is measured and k is the hydraulic conductivity. The previous equation was originally written as

$$Q = -kA \frac{\Delta H}{L}, \quad (2.4)$$

where ΔH is the hydraulic head. Figure 2.3 shows the Darcy velocity $u_D = Q/A$ versus $\Delta H/L$. Darcy's data clearly show the linearity between the average discharge rate of fluid and the pressure gradient.

The hydraulic conductivity depends on the kinematic viscosity ν [2]

$$k = \frac{gK}{\nu}, \quad (2.5)$$

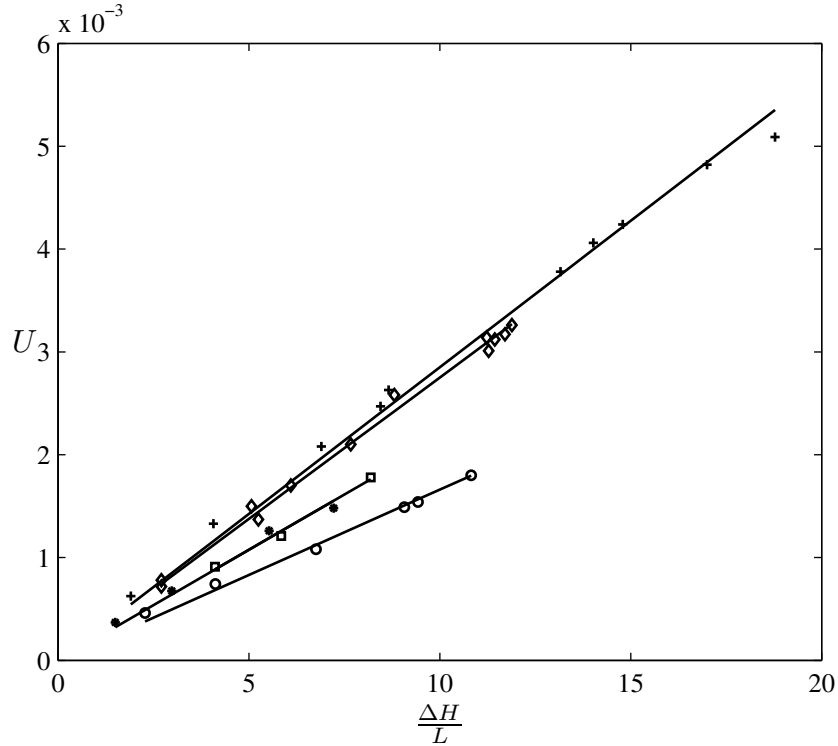


Figure 2.3: Darcy's experiment data. The solid line are the fit of the experimental data.

where K is the permeability. So Darcy's law becomes

$$Q = -\frac{KA}{\mu} \frac{p_2 - p_1}{L}, \quad (2.6)$$

where μ is the dynamic fluid viscosity.

Permeability represents the ease with which fluid passes through a porous material, and is a property of the material. Typical values are reported in table 2.1. We can now define a Reynolds number characteristic of the porous flow as

$$\text{Re}_p = \frac{\sqrt{K} u_D}{\nu}. \quad (2.7)$$

For the flow illustrated in figure 2.4, equation (2.6) can be written for the Darcy velocity, or filtering velocity, in a differential form as:

$$u_D = \frac{Q}{A} = -\frac{K}{\mu} \frac{dp}{dx}. \quad (2.8)$$

Writing Darcy's law as

$$\frac{dp}{dx} + \frac{\mu}{K} u_D = 0, \quad (2.9)$$

Material	$-\log_{10} K$
Clean gravel	7 ÷ 9
Clean sand	9 ÷ 12
Very fine sand	12 ÷ 16
Peat	11 ÷ 13
Stratified clay	13 ÷ 15
Unweathered clay	16 ÷ 20
Oil rocks	11 ÷ 14
Sandstone	14 ÷ 16
Dolomite	16 ÷ 18
Granite	18 ÷ 20

Table 2.1: Some typical values of permeability taken from [2].

Figure 2.4: Sketch of a porous layer.

the second term can be interpreted as an average drag felt by the fluid as it passes through the porous medium, which is balanced by the pressure gradient [55, 22]. For the low porous Reynolds number for which Darcy's law hold $Re_p \ll 1$, the flow is governed by Stokes' equation

$$\nabla p - \mu \nabla^2 \mathbf{u} = 0. \quad (2.10)$$

Therefore, the viscous term in Stokes' equation is responsible for the Darcy drag.

As Re increases we observe a deviation from the linear relationship. To the best of our knowledge, Forchheimer was the first to suggest a nonlinear relationship, adding a quadratic drag term which provides a better fit with experimental data. The new equation is called Forchheimer equation and reads

$$\frac{dp}{dx} + \frac{\mu}{K} u_D + C u_D^2 = 0, \quad (2.11)$$

where C is a coefficient which depends both on the fluid and material properties. Recent studies have confirmed that this term is due to inertial effects in the flow within the pores [22, 55, 56, 57, 17, 24]. When the flow is no more governed by the Stokes equation the quadratic drag term is due to the convective term, $(\mathbf{u} \cdot \nabla) \mathbf{u}$, in the Navier-Stokes equations.

Subsequently, Brinkman [24] suggested to extend Darcy's law to high permeable materials, adding a sort of viscous term in the Stokes' equation. This results in the following equation

$$\nabla p + \frac{\mu}{K} \mathbf{u}_D - \mu_e \nabla^2 \mathbf{u}_D = 0, \quad (2.12)$$

where μ_e is the effective Brinkman viscosity, which must be determined experimentally, and \mathbf{u}_D is the multidimensional Darcy velocity a sort of locally averaged quantity.

From an historical point of view Darcy's law was born by experiments, but theoretical support for its validity has been obtained quite recently by Whitaker [56] by means of the method of Volume Averaging [55]. The procedure consists in averaging the microscopic flow field over a small spatial volume to obtain the macroscopic or volume-averaged flow field. Whitaker showed that Darcy's law can be deduced applying the volume averaging technique to the Stokes' equation.

2.2 Volume Averaged Navies-Stokes

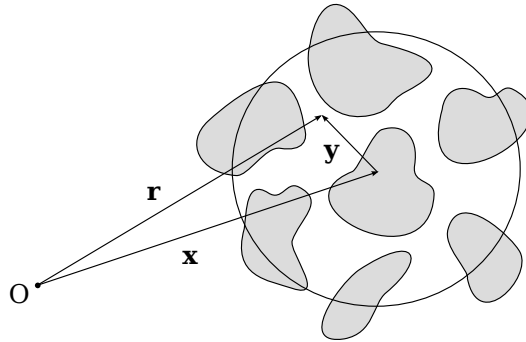


Figure 2.5: Sketch of porous medium with position vectors.

The method of volume averaging have been formally derived by Whitaker [55, 56, 57]. The technique considers only the large scale behaviour of the flow, i.e. , the macroscopic behaviour. This is obtained by averaging the governing equations over a small volume V of radius $r \ll L_p$, and solving for the volume averaged unknowns. A general assumption is that the length scales are well separated, $l_s \sim l_f \ll r \ll L_p$. The radius r should be large enough so that volume-averaged quantities result in smooth functions and are free of small scale fluctuations. The method involves to treat the porous medium as a continuum, so fluid quantities are defined in every point, notwithstanding it corresponds to fluid or solid phase.

Following [56, 57, 9], the first step in the derivation of the Volume Averaged Navies-Stokes (VANS) equations is the introduction of the averages. For an arbitrary quantity ϕ , the *superficial volume average* is defined as [57, 35]

$$\langle \phi \rangle_{\mathbf{x}}^s = \frac{1}{V} \int_{V_f(\mathbf{x})} \phi(\mathbf{x} + \mathbf{y}) dV_f, \quad (2.13)$$

where $V_f < V$ is the volume of fluid contained within the averaging volume V , the subscript \mathbf{x} means that $\langle \phi \rangle^s$ is evaluated at the centroid \mathbf{x} of the averaging

volume V , and $\mathbf{y} = \mathbf{r} - \mathbf{x}$ is the relative position vector. The position vectors used in (2.13) are identified in figure 2.5.

We can define another volume average, the *intrinsic volume average*, as

$$\langle \phi \rangle_{\mathbf{x}}^f = \frac{1}{V_f} \int_{V_f(\mathbf{x})} \phi(\mathbf{x} + \mathbf{y}) dV_f, \quad (2.14)$$

The difference between the two averages is that the superficial average (2.13) is averaged over the entire averaging volume V , while the intrinsic average (2.14) is averaged over only the volume of fluid V_f . The two averages are related by

$$\langle \phi \rangle^s = \frac{V_f}{V} \langle \phi \rangle^f = \varepsilon \langle \phi \rangle^f, \quad (2.15)$$

where $\varepsilon = V_f/V$ is the porosity, or volume-fraction of the fluid and it is generally a function of position \mathbf{x} in a heterogeneous porous media.

To derive the volume averaged form of the Navier-Stokes equations it is necessary to find the relations between the volume average of a derivative and the derivative of the volume average, both for time and spatial derivatives. The relationship for the volume average of a time derivative is known as *general transport theorem* [44, 35]

$$\left\langle \frac{\partial \phi}{\partial t} \right\rangle^s = \frac{\partial \langle \phi \rangle^s}{\partial t} - \frac{1}{V} \int_A \mathbf{n} \cdot \mathbf{w} \phi dA, \quad (2.16)$$

where A is the interface area between the fluid and the solid phase inside the averaging volume V , \mathbf{n} is the unit normal at A that points from the fluid into the solid phase, and $\mathbf{n} \cdot \mathbf{w}$ is the local speed of displacement of the surface A . Since we restrict ourselves to rigid porous media, it holds that $\mathbf{w} = \mathbf{0}$. Consequently, for rigid porous media, the volume average of a time derivative is equal to the time derivative of the volume average. The relation for the volume average of spatial derivatives is known as the *spatial averaging theorem* [58, 34]

$$\langle \nabla \phi \rangle^s = \nabla \langle \phi \rangle^s + \frac{1}{V} \int_A \mathbf{n} \phi dA, \quad (2.17)$$

A useful relation for the porosity's spatial derivatives is obtained from the substitution of $\phi = 1$ in equation (2.17)

$$0 = \nabla \langle 1 \rangle^s + \frac{1}{V} \int_A \mathbf{n} dA = \nabla (\varepsilon \langle 1 \rangle^f) + \frac{1}{V} \int_A \mathbf{n} dA \implies \nabla \varepsilon = -\frac{1}{V} \int_A \mathbf{n} dA. \quad (2.18)$$

A generalization of equation (2.17) is [35]

$$\nabla \langle \mathbf{M} \rangle^s = -\frac{1}{V} \int_A \mathbf{n} \mathbf{M} dA, \quad (2.19)$$

where \mathbf{M} is a tensor of n^{th} order rank.

In order to obtain the VANS we apply the volume-averaging operator $\langle \dots \rangle^s$ to the Navier-Stokes equations, (2.1) and (2.2), for an incompressible, Newtonian fluid

$$\left\langle \frac{\partial \mathbf{u}}{\partial t} \right\rangle^s + \langle \nabla \cdot (\mathbf{u} \otimes \mathbf{u}) \rangle^s = \left\langle -\frac{1}{\rho} \nabla p \right\rangle^s + \langle \nu \nabla^2 \mathbf{u} \rangle^s, \quad (2.20)$$

$$\langle \nabla \cdot \mathbf{u} \rangle^s = 0. \quad (2.21)$$

Application of the general transport theorem (2.16) yields

$$\left\langle \frac{\partial \mathbf{u}}{\partial t} \right\rangle^s = \frac{\partial \langle \mathbf{u} \rangle^s}{\partial t} - \frac{1}{V} \int_A \mathbf{n} \cdot \mathbf{w} \mathbf{u} dA = \frac{\partial \langle \mathbf{u} \rangle^s}{\partial t}, \quad (2.22)$$

where we have used that $\mathbf{w} = 0$ for rigid porous media, while the application of the spatial averaging theorem (2.17) yields

$$\langle \nabla \cdot \mathbf{u} \otimes \mathbf{u} \rangle^s = \nabla \cdot \langle \mathbf{u} \otimes \mathbf{u} \rangle^s + \frac{1}{V} \int_A \mathbf{n} \cdot \mathbf{u} \otimes \mathbf{u} dA = \nabla \cdot \langle \mathbf{u} \otimes \mathbf{u} \rangle^s, \quad (2.23)$$

$$\left\langle -\frac{1}{\rho} \nabla p \right\rangle^s = -\frac{1}{\rho} \nabla \langle p \rangle^s - \frac{1}{V} \int_A \mathbf{n} \frac{p}{\rho} dA, \quad (2.24)$$

$$\begin{aligned} \langle \nu \nabla^2 \mathbf{u} \rangle^s &= \nu \nabla \cdot \langle \nabla \mathbf{u} \rangle^s + \nu \frac{1}{V} \int_A \mathbf{n} \cdot \nabla \mathbf{u} dA = \\ &= \nu \nabla^2 \langle \mathbf{u} \rangle^s + \nu \frac{1}{V} \int_A \mathbf{n} \cdot \nabla \mathbf{u} dA + \nu \nabla \cdot \frac{1}{V} \int_A \mathbf{n} \otimes \mathbf{u} dA = \\ &= \nu \nabla^2 \langle \mathbf{u} \rangle^s + \nu \frac{1}{V} \int_A \mathbf{n} \cdot \nabla \mathbf{u} dA, \end{aligned} \quad (2.25)$$

$$\langle \nabla \cdot \mathbf{u} \rangle^s = \nabla \cdot \langle \mathbf{u} \rangle^s + \frac{1}{V} \int_A \mathbf{n} \cdot \mathbf{u} dA = \nabla \cdot \langle \mathbf{u} \rangle^s, \quad (2.26)$$

where some integrals vanish since $\mathbf{u} = \mathbf{0}$ at the interface area A . The continuity equation (2.26) underlines the difference between the superficial and intrinsic volume averages; in fact in case of spatially varying porosity, only the superficial velocity is divergence free. So, we obtain

$$\begin{aligned} \frac{\partial \langle \mathbf{u} \rangle^s}{\partial t} + \nabla \cdot \langle \mathbf{u} \otimes \mathbf{u} \rangle^s &= -\frac{1}{\rho} \nabla \langle p \rangle^s + \nu \nabla^2 \langle \mathbf{u} \rangle^s + \\ &+ \frac{1}{V} \int_A \mathbf{n} \cdot \left(-\frac{p}{\rho} \mathbf{I} + \nu \nabla \mathbf{u} \right) dA, \end{aligned} \quad (2.27)$$

$$\nabla \cdot \langle \mathbf{u} \rangle^s = 0. \quad (2.28)$$

The problem defined by equations (2.27) and (2.28) lack of closure because the convective and integral terms involve not averaged quantities. The system can

be written more generally as

$$\frac{\partial \langle \mathbf{u} \rangle^s}{\partial t} + \nabla \cdot \left[\frac{\langle \mathbf{u} \rangle^s \otimes \langle \mathbf{u} \rangle^s}{\varepsilon} \right] + \nabla \cdot \boldsymbol{\tau} = -\frac{1}{\rho} \nabla \langle p \rangle^s + \nu \nabla^2 \langle \mathbf{u} \rangle^s + \mathbf{f}, \quad (2.29)$$

$$\nabla \cdot \langle \mathbf{u} \rangle^s = 0, \quad (2.30)$$

where $\boldsymbol{\tau}$ is the subfilter-scale stress and \mathbf{f} is the drag force that the solid phase exerts on the fluid phase. The definition for $\boldsymbol{\tau}$ and \mathbf{f} are

$$\boldsymbol{\tau} \equiv \langle \mathbf{u} \otimes \mathbf{u} \rangle^s - \frac{\langle \mathbf{u} \rangle^s \langle \mathbf{u} \rangle^s}{\varepsilon}, \quad (2.31)$$

$$\mathbf{f} \equiv \frac{1}{V} \int_A \mathbf{n} \cdot \left(-\frac{p}{\rho} \mathbf{I} + \nu \nabla \mathbf{u} \right) dA. \quad (2.32)$$

Performing the following decomposition:

$$p = \langle p \rangle^f + \tilde{p} = \frac{1}{\varepsilon} \langle p \rangle^s + \tilde{p}, \quad (2.33)$$

$$\mathbf{u} = \langle \mathbf{u} \rangle^f + \tilde{\mathbf{u}} = \frac{1}{\varepsilon} \langle \mathbf{u} \rangle^s + \tilde{\mathbf{u}}, \quad (2.34)$$

the integral term can be developed further

$$\begin{aligned} \mathbf{f} &= \frac{1}{V} \int_A \mathbf{n} \cdot \left(-\frac{p}{\rho} \mathbf{I} + \nu \nabla \mathbf{u} \right) dA = \\ &= \frac{1}{V} \int_A \mathbf{n} \cdot \left[-\frac{(\langle p \rangle^f + \tilde{p})}{\rho} \mathbf{I} + \nu \nabla (\langle \mathbf{u} \rangle^f + \tilde{\mathbf{u}}) \right] dA = \\ &= \frac{1}{V} \int_A \mathbf{n} \cdot \left(-\frac{\langle p \rangle^f}{\rho} \mathbf{I} + \nu \nabla \langle \mathbf{u} \rangle^f \right) dA + \frac{1}{V} \int_A \mathbf{n} \cdot \left(-\frac{\tilde{p}}{\rho} \mathbf{I} + \nu \nabla \tilde{\mathbf{u}} \right) dA = \\ &= -\nabla \varepsilon \cdot \left(-\frac{\langle p \rangle^f}{\rho} \mathbf{I} + \nu \nabla \langle \mathbf{u} \rangle^f \right) dA + \frac{1}{V} \int_A \mathbf{n} \cdot \left(-\frac{\tilde{p}}{\rho} \mathbf{I} + \nu \nabla \tilde{\mathbf{u}} \right) dA. \end{aligned} \quad (2.35)$$

Exploiting (2.35) and

$$-\frac{1}{\rho} \nabla \langle p \rangle^s = -\frac{1}{\rho} \nabla (\langle p \rangle^f \varepsilon) = -\frac{\varepsilon}{\rho} \nabla \langle p \rangle^f - \frac{1}{\rho} \langle p \rangle^f \nabla \varepsilon, \quad (2.36)$$

the Volume Averaged Navier-Stokes (VANS) equations become

$$\begin{aligned} \frac{\partial \langle \mathbf{u} \rangle^s}{\partial t} + \nabla \cdot \left[\frac{\langle \mathbf{u} \rangle^s \otimes \langle \mathbf{u} \rangle^s}{\varepsilon} \right] + \nabla \cdot \boldsymbol{\tau} &= -\frac{\varepsilon}{\rho} \nabla \langle p \rangle^f + \nu \nabla^2 \langle \mathbf{u} \rangle^s + \\ &\quad -\nu \nabla \varepsilon \cdot \nabla \langle \mathbf{u} \rangle^s + \frac{1}{V} \int_A \mathbf{n} \cdot \left(-\frac{\tilde{p}}{\rho} \mathbf{I} + \nu \nabla \tilde{\mathbf{u}} \right) dA, \end{aligned} \quad (2.37)$$

$$\nabla \cdot \langle \mathbf{u} \rangle^s = 0. \quad (2.38)$$

The first viscous term $\nu \nabla^2 \langle \mathbf{u} \rangle^s$ is the Brinkman correction and it is often included in the analysis of flow in the boundary region between a porous medium and a homogeneous fluid. In such regions the second viscous term $\nu \nabla \varepsilon \cdot \nabla \langle \mathbf{u} \rangle^s$ has the same order of magnitude as the Brinkman correction, and, generally, it can not be neglected. The latter is referred to as the second Brinkman correction. A key point about equations (2.37) and (2.38) is that they are valid everywhere since no length scale constraints have been imposed.

It has been shown [56] that the integral term

$$\frac{1}{V_f} \int_A \mathbf{n} \cdot (-\tilde{p} \mathbf{I} + \mu \nabla \tilde{\mathbf{u}}) dA = -\mu \phi, \quad (2.39)$$

has an especially simple form in a homogeneous porous medium $\nabla \varepsilon = 0$, where it can be written as

$$-\mu \phi = -\mu \mathbf{K}^{-1} \cdot \langle \mathbf{u} \rangle^s - \mu \mathbf{K}^{-1} \cdot \mathbf{F} \cdot \langle \mathbf{u} \rangle^s, \quad (2.40)$$

where \mathbf{K} is the second-order permeability tensor. The first term is called Darcy drag, while the second is the Forchheimer term. \mathbf{F} is a second-order tensor whose exact form depends on the structure of the porous medium. Experimentally, it is usually found to be a linear function of the volume averaged velocity $\langle \mathbf{u} \rangle^s$, producing a Forchheimer term that is quadratic [5, 22, 57, 17]. Moreover, Whitaker [57] found that the convective terms generated by the nonlinear part of the Navier-Stokes equations are of the same order of magnitude and are both usually negligible in comparison with the dominant Forchheimer term. The latter is negligible when the inertial effects are small.

In the homogeneous region, where $\nabla \varepsilon = 0$, and for an isotropic porous material with small inertial effects, the VANS equations become

$$\frac{\partial \langle \mathbf{u} \rangle^s}{\partial t} = -\frac{\varepsilon}{\rho} \nabla \langle p \rangle^f + \nu \nabla^2 \langle \mathbf{u} \rangle^s - \frac{\nu}{K} \varepsilon \langle \mathbf{u} \rangle^s, \quad (2.41)$$

$$\nabla \cdot \langle \mathbf{u} \rangle^s = 0. \quad (2.42)$$

So far we have adopted the convention of preferring the superficial volume-averaged velocity $\langle \mathbf{u} \rangle$ and the intrinsic volume averaged pressure $\langle p \rangle^f$. When dealing with VANS equations, the superficial volume-averaged velocity $\langle \mathbf{u} \rangle$ is the preferred representation of the velocity since it is always solenoidal, while the intrinsic volume-averaged velocity $\langle \mathbf{u} \rangle^f$ is only solenoidal in the case of constant porosity. However for the pressure the intrinsic volume average $\langle p \rangle^f$ is preferred, because it is the one measured by a probe in an experimental apparatus.

2.2.1 Darcy's law

Whitaker [56] and Ochoa-Tapia and Whitaker [29] have shown that volume averaging the Stokes' equations for a stationary, incompressible, viscous flow

through a rigid homogeneous porous medium (2.10) produces Darcy's law with the Brinkman term

$$-\nabla\langle p\rangle^f + \frac{\mu}{\varepsilon}\nabla^2\langle\mathbf{u}\rangle - \mu\mathbf{K}^{-1}\cdot\langle\mathbf{u}\rangle = 0. \quad (2.43)$$

Note that volume averaging produces a Brinkman term, $\mu/\varepsilon\nabla^2\langle\mathbf{u}\rangle$, without an effective viscosity. Ochoa-Tapia and Whitaker [29] found also that the Brinkman term is usually negligible in comparison with the dominant pressure and Darcy terms. The exception is near the interface between a porous region and a purely fluid region.

2.2.2 LES analogy

The VANS procedure can be considered as a generalization of the LES procedure. The volume-averaging operator (2.13) acts as a filter which passes only information on the large scale structures of the flow field. It can be generalized defining a filter operator analogous to the one used in Large Eddy Simulations [34, 35, 25, 9] as it follows

$$\langle\phi\rangle_{\mathbf{x}}^s = \int_V m(\mathbf{y})\gamma(\mathbf{r})\phi(\mathbf{r})dV, \quad (2.44)$$

where γ is the phase-indicator function and m is a weighting function. γ equals unity when \mathbf{r} points in the fluid phase and zero when \mathbf{r} points in the solid phase. The weighting function must satisfy the following normalization condition

$$\int_V m(\mathbf{y})dV = 1. \quad (2.45)$$

The LES equations can be obtained from the VANS equations (2.29) and (2.30) for a purely homogeneous fluid region, where $\varepsilon = 1$, and observing that, because of the absence of a solid phase the drag force is zero $\mathbf{f} = 0$

$$\frac{\partial\langle\mathbf{u}\rangle^s}{\partial t} + \nabla\cdot(\langle\mathbf{u}\rangle^s\otimes\langle\mathbf{u}\rangle^s) + \nabla\cdot\boldsymbol{\tau} = -\frac{1}{\rho}\nabla\langle p\rangle^s + \nu\nabla^2\langle\mathbf{u}\rangle^s, \quad (2.46)$$

$$\nabla\cdot\langle\mathbf{u}\rangle^s = 0. \quad (2.47)$$

2.3 Interface conditions

The problem of momentum transport at the boundary between a porous medium and a homogeneous fluid, see figure 2.6, occurs in a wide variety of technological applications, and has been the object of a great deal of study in the porous flow community. In order to study the problem, we consider a flat channel delimited by an upper impermeable wall and a lower, semi-infinite porous wall, as illustrated in

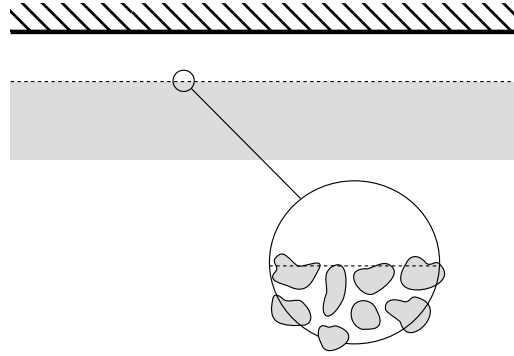


Figure 2.6: Interface between a porous region and a purely fluid region.

figure 2.7(a). In particular, porous layers are fluid saturated, rigid, homogeneous and isotropic. A uniform longitudinal pressure gradient dp/dx drives a steady fully developed laminar flow in both the channel and porous region.

At the interface, the fluid velocity must decrease from its interface value to the Darcy velocity. This is achieved in the so called Brinkman layer. This small region is where mass and momentum transfer take place.

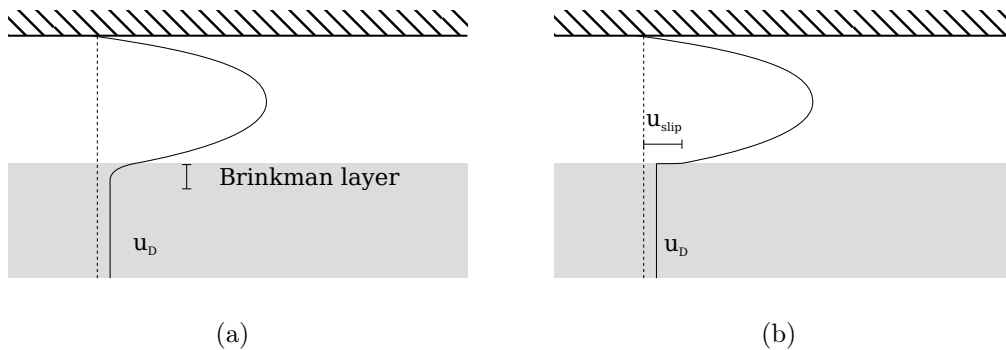


Figure 2.7: Velocity profiles of the flow through a porous medium, not to scale. Figure (b) shows the velocity profile obtained with the Beavers and Joseph condition.

The interface can be treated mainly in two ways, as smooth (within a single-domain model) or sharp (within a two-domain model). In the single-domain approach, the composite region is considered as a continuum and one set of general governing equations is applied for the whole domain. All averaged flow variables are continuous and the change in flow physics is simulated by varying porosity. In the two-domain approach, two sets of governing equations are applied to describe the flow in the two regions and additional boundary conditions are applied at the interface to close the two sets of equations. The interface region is replaced with an interface of zero height, and both the free-fluid and porous regions are extrapolated over the interface region, resulting in step change of some

flow variables across the interface. This method is more reliable, since it tries to simulate the flow behaviour at the interface and it will be used in this work.

For a systematic analysis of the variance among different boundary conditions see Alazmi and Vafai [1]. In this work, the authors concluded that, in most of the cases, the variances between the different models have negligible effect on the results.

2.3.1 The Beavers and Joseph condition

To the best of our knowledge, Beavers and Joseph [3] were the first to prove that when a viscous fluid flows at the interface of a porous medium, the effects of viscous shear will penetrate beneath the permeable surface, to form what is effectively a boundary layer, the Brinkman layer. They performed a series of experiments and they observed that the slip velocity at the interface differs from the Darcy velocity u_D . In fact Darcy's law is not compatible with the existence of a boundary layer region, because no macroscopic shear term is associated with this equation. They proposed to model the effects of the Brinkman layer on the external flow by introducing a discontinuous slip velocity, u_{slip} , as shown in figure 2.7(b). They postulated that this slip velocity is proportional to the shear rate, du/dy , at the permeable boundary

Material	$10^{-5}\mathbf{K} [in^2]$	α	τ
Foametal A	1.5	0.78	0.70
Foametal B	6.1	1.45	0.00
Foametal C	12.7	4.00	-1.00
Aloxite	0.1	0.10	1.47

Table 2.2: Some typical values of permeability together with the coefficient α_{BJ} determined experimentally by Beavers and Joseph [3], and the momentum transfer coefficient τ determined by Ochoa-Tapia and Whitaker [30] assuming $\varepsilon = 0.4$.

$$\frac{du}{dy} = \frac{\alpha_{BJ}}{\sqrt{K}} (u_{slip} - u_D) \quad (2.48)$$

where α_{BJ} is a dimensionless coefficient which depends on the structure of the porous material in the boundary region, and that must be determined by experiments. Beavers and Joseph calculated it for the materials reported in table 2.2.

Beavers, Sparrow and Magnuson [4] confirmed the Beavers and Joseph condition experimentally, while Saffman [41] further justified it theoretically. Saffman also found that, as the permeability tends to small but finite values, the Darcy velocity in the Beavers and Joseph interface condition may be ignored.

Taylor [48] and Richardson [40] collaborated in order to perform an experiment with a particular porous material for which both K and α could be calculated analytically, and they compared the results of calculation with experiments. The geometry of the porous media is called Taylor brush configuration, and it has been further studied by other authors, as in [43].

Other authors determined the values of the slip coefficient α_{BJ} for other materials and other geometries. Liu, Chen and Wang [26] performed an experimental and numerical estimation of slip coefficient in a partially porous cavity. Their paper reported an experimental investigation of natural convection flow in a two-dimensional cavity, partially filled with a vertical porous layer.

2.3.2 The Brinkman condition

The Beavers and Joseph condition does not provide information on the structure of the Brinkman layer within the porous region. Neale and Nader [28] reconsidered the channel problem and modelled the flow in the porous region using the Brinkman equation

$$\frac{dp}{dx} = -\frac{\mu}{K}u_D + \mu_e \frac{d^2 u_d}{dy^2}. \quad (2.49)$$

Thanks to the macroscopic shear term, the Brinkman equation is fully compatible with the presence of a boundary layer region within the porous medium; outside the Brinkman layer, the Brinkman term is very small, indicating that Darcy's law is valid everywhere except at the boundaries.

In order to couple the flow through the porous material and through the fluid region, they imposed continuity of velocity and its derivative at the interface, using the following interface conditions

$$u = u_D \quad \mu \frac{du}{dy} = \mu_e \frac{du_D}{dy}. \quad (2.50)$$

While these conditions were first proposed by Neale and Nader, they are also commonly referred to as Brinkman interface conditions.

Neale and Nader discovered that their conditions (2.50) produce the same interface velocity as the slip velocity predicted by the Beavers and Joseph condition (2.50), provided that

$$\mu_e = \mu \alpha_{BJ}^2. \quad (2.51)$$

It is useful to define the Brinkman layer thickness δ_B as the distance measured from the interface into the porous region at which the fluid velocity first approaches within 1 of the Darcy velocity; the Brinkman conditions also predict that the Brinkman layer thickness δ_B is of the order of the square root of the permeability, $\delta_B \sim \sqrt{k}$.

We have observed that in order to agree with the experimental data of Beaver and Joseph, the effective viscosity must satisfy relation (2.51). However, in order

to agree with Whitaker's derivation of VANS, it must satisfy

$$\mu_e = \frac{\mu}{\varepsilon}, \quad (2.52)$$

see equations (2.12) and (2.43). Generally, it is not possible to satisfy all these relationships simultaneously.

2.3.3 The momentum transfer conditions of Ochoa-Tapia and Whitaker

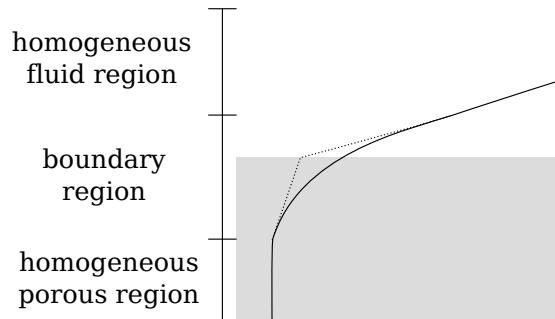


Figure 2.8: Fluid velocity profile at the interface between a porous region and a purely fluid region.

Figure 2.8 illustrates a hypothetical fluid velocity profile at the interface between a porous region and a purely fluid region. In this region the flow is governed by equations (2.37) and (2.38),

$$\frac{\partial \langle \mathbf{u} \rangle^s}{\partial t} + \nabla \cdot \left[\frac{\langle \mathbf{u} \rangle^s \otimes \langle \mathbf{u} \rangle^s}{\varepsilon} \right] + \nabla \cdot \boldsymbol{\tau} = -\frac{\varepsilon}{\rho} \nabla \langle p \rangle^f + \nu \nabla^2 \langle \mathbf{u} \rangle^s + \quad (2.53)$$

$$-\nu \nabla \varepsilon \cdot \nabla \langle \mathbf{u} \rangle^s - \nu \varepsilon \mathbf{K}^{-1} \cdot \langle \mathbf{u} \rangle^s - \nu \varepsilon \mathbf{K}^{-1} \cdot \mathbf{F} \cdot \langle \mathbf{u} \rangle^s,$$

$$\nabla \cdot \langle \mathbf{u} \rangle^s = 0, \quad (2.54)$$

which have been obtained without imposing any length scale constraints. Solution of the problem requires the knowledge of the variation of porosity within the transition region; moreover, suitable models are necessary to evaluate nonlinear terms and Forchheimer tensor. For recent developments on this approach, we refer the reader to Valdes, Goycau and Ochoa-Tapia [53] and Breugem [9]. Usually, the variation of the porosity in the transition region is not known in advance, so the problem requires closure. Providing a suitable profile for ε is difficult even experimentally. This problem can be avoided if an acceptable jump condition is constructed.

In a region sufficiently below the interface, we assume the porous material is homogeneous and the flow is governed by the VANS and continuity equations (2.41) and (2.42),

$$\frac{\partial \langle \mathbf{u} \rangle^s}{\partial t} = -\frac{\varepsilon}{\rho} \nabla \langle p \rangle^f + \nu \nabla^2 \langle \mathbf{u} \rangle^s - \frac{\nu}{K} \varepsilon \langle \mathbf{u} \rangle^s, \quad (2.55)$$

$$\nabla \cdot \langle \mathbf{u} \rangle^s = 0. \quad (2.56)$$

This region is called the homogeneous porous region. Previous equations are not valid in a small heterogenous transition layer adjacent to the interface, where the structure of the porous material undergoes rapid changes. For exemple, the porosity increase rapidly from its value in the homogeneous porous region ε to unity slightly above the interface.

We extend validity of equations (2.55) and (2.56) to the interface, even if the porous material is heterogeneous. As consequence, this assumption produces an error in the local averaged velocity $\langle \mathbf{v} \rangle^s$ and pressure $\langle p \rangle^f$. However, the error will be corrected by means of an additional condition, the so-called jump condition, which ensures that equations (2.53) and (2.54) are satisfied on average in the boundary region.

The conditions created by Ochoa-Tapia and Whitaker couple the Navier-Stokes equations (2.1) and (2.2) directly to the Volume Averaged Navier-Stokes equations (2.55) and (2.56). The velocity and the pressure are forced to be continuous at the interface and generally produce a discontinuity in the shear stress. In figure 2.8 the dashed line illustrates a hypothetical velocity profile generated by the interface conditions of Ochoa-Tapia and Whitaker; note that the conditions may not predict the profile of the Brinkman layer as accurately as equations (2.53) and (2.54).

When the porous region is homogeneous and isotropic, and the permeability is sufficiently small to neglect inertial effects, the momentum transfer conditions are [29]

$$u = \langle u \rangle^s, \quad (2.57a)$$

$$v = \langle v \rangle^s, \quad (2.57b)$$

$$w = \langle w \rangle^s, \quad (2.57c)$$

$$p = \langle p \rangle, \quad (2.57d)$$

$$\frac{1}{\varepsilon} \frac{\partial \langle u \rangle^s}{\partial y} - \frac{\partial u}{\partial y} = \pm \frac{\tau}{\sqrt{K}} u, \quad (2.57e)$$

$$\frac{1}{\varepsilon} \frac{\partial \langle w \rangle^s}{\partial y} - \frac{\partial w}{\partial y} = \pm \frac{\tau}{\sqrt{K}} w. \quad (2.57f)$$

In equations (2.57) positive sign is used when the purely fluid region is above a porous interface, while the negative sign denotes the converse. Symbol τ has been

introduced as constant coefficient which accounts for the distribution of momentum at the interface and depends on the manner in which a porous material's structure varies in the transition layer. While there is work on determining τ theoretically [53], it must usually be determined experimentally. Analytically, Ochoa-Tapia and Whitaker [29] estimated that τ is of the order of one and may be either positive or negative.

Ochoa-Tapia and Whitaker [30] found that conditions (2.57) showed good agreement with the experimental data of Beavers and Joseph [3]. The results for τ are summarized in table 2.2.

When inertial effects are significant in the porous region the jump condition is more complicated. Ochoa-Tapia and Whitaker [31] extended the stress condition to include inertial effects

$$\frac{1}{\varepsilon} \frac{\partial \langle u \rangle^s}{\partial y} - \frac{\partial u}{\partial y} = \pm \frac{\tau}{\sqrt{K}} u \pm \frac{\gamma}{\nu} u^2, \quad (2.58)$$

where γ , which accounts for the effects of inertia in the momentum transfer process, is a dimensionless coefficient of order one that must be determined experimentally; anyway there are currently no published experimental data for it.

The stress jump boundary conditions (2.57) has been studied and used by many reserchers.

Kuznetsov [23] investigated the dependence of the velocity on the adjustable coefficient in the stress jump boundary condition. He obtained analytical solutions for three different types of channels partially filled with a porous medium and the stress jump boundary condition is utilized at the interface. He showed that accounting for a jump in the shear stress at the interface essentially influences velocity profiles.

Tan and Pillai [47] considered the interface between a porous medium and a clear fluid. Their results have shown that, when the porosity of the porous media is high, the stress jump condition yields a result significantly different from the one provided by the stress-continuity condition. It is also shown that when the porosity of the porous medium is high, the stress continuity condition results in a much larger boundary layer as compared to the stress jump condition. However, the two interfacial conditions tend to yield similar results as the porosity decreases.

Yu, Lee, Zeng and Low [59] and Chen, Yu, Winoto and Low [13] developed a numerical method for flows involving an interface between a homogeneous fluid and a porous medium. The Brinkman-Forchheimer extended model was used to govern the flow in the porous medium region. At its interface, the flow boundary condition imposed is a shear stress jump, which includes the inertial effect, together with a continuity of normal stress.

Costa, Oliveira and Baliga [15] implemented the stress jump condition simulating laminar coupled flows in adjacent open and porous domains.

Chapter 3

Problem definition

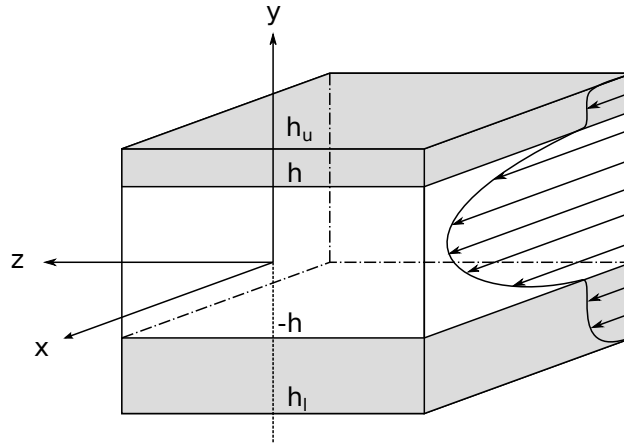


Figure 3.1: Sketch of the channel geometry.

We consider the flow of an incompressible viscous fluid through a channel with flat porous walls, as sketched in fig 3.1. We assume the porous layers to be fluid saturated, rigid, homogeneous and isotropic. We model the fluid flow through the porous medium using the Volume Averaged Navier-Stokes equations (2.41) and (2.42). The momentum transfer at each interface between the purely fluid region and porous layer is described by the conditions derived by Ochoa-Tapia and Whitaker (2.57). At the walls, we impose the no-penetration and no-slip conditions and assume the flow to be periodic in the streamwise and spanwise directions.

We consider the cartesian coordinate system shown in figure 3.1, where x , y and z denote the streamwise, wall-normal and spanwise coordinates, while u , v and w denote the respective components of the velocity vector field. The lower and upper interfaces are located at $y = -h$ and $y = h$, respectively, while the lower and upper impermeable walls are located at $y = h_l = -h - 2hh_1$ and

$y = h_u = h + 2hh_2$, respectively. In the following, we will refer to the lower and upper porous layers with the subscripts 1 and 2, respectively.

3.1 Non-dimensional equations

We formulate the mathematical problem and make it dimensionless. Note that non-dimensional quantities are identified by the superscript "-".

We define as a characteristic length one-half the height of the central purely fluid layer

$$L^* = h, \quad (3.1)$$

and as characteristic velocity U^*

$$U^* = U_b = \frac{1}{2h} \int_{-h}^h U dy, \quad (3.2)$$

where $U(y)$ can be either the laminar or turbulent mean velocity profile. Therefore, the Reynolds number is defined as

$$\text{Re} = \frac{U^* L^*}{\nu}. \quad (3.3)$$

3.1.1 Navier-Stokes equations

To make the Navier-Stokes equations (2.1) and (2.2) nondimensional, we use the reference length L^* , the reference velocity U^* and define as reference time $T^* = L^*/U^*$. Then, writing $u = U^* \bar{u}$ and $p = \rho U^{*2} \bar{p}$ and dividing the two equations respectively by U^{*2}/L^* and U^*/L^* , we obtain the non-dimensional Navier-Stokes equations

$$\frac{\partial \bar{\mathbf{u}}}{\partial \bar{t}} + \nabla \cdot (\bar{\mathbf{u}} \otimes \bar{\mathbf{u}}) = -\nabla \bar{p} + \frac{1}{\text{Re}} \nabla^2 \bar{\mathbf{u}}, \quad (3.4)$$

$$\nabla \cdot \bar{\mathbf{u}} = 0. \quad (3.5)$$

3.1.2 Volume Averaged Navier-Stokes equations

In this study we model the flow through the porous media with equations (2.41) and (2.42), that we report here for convenience

$$\frac{\partial \langle \mathbf{u} \rangle^s}{\partial t} = -\frac{\varepsilon}{\rho} \nabla \cdot \langle p \rangle^f + \nu \nabla^2 \langle \mathbf{u} \rangle^s - \frac{\nu}{K} \varepsilon \langle \mathbf{u} \rangle^s, \\ \nabla \cdot \langle \mathbf{u} \rangle^s = 0.$$

To make the above equations nondimensional, we use the reference length L^* , the reference velocity U^* and define as reference time $T^* = L^*/U^*$. Then, writing $u =$

$U^*\bar{u}$ and $p = \rho U^{*2}\bar{p}$ and dividing the two equations respectively by U^{*2}/L^* and U^*/L^* , we obtain the non-dimensional Volume-Averaged Navier-Stokes equations

$$\frac{\partial \langle \bar{\mathbf{u}} \rangle^s}{\partial t} = -\varepsilon \nabla \langle \bar{p} \rangle^f + \frac{1}{\text{Re}} \nabla^2 \langle \bar{\mathbf{u}} \rangle^s - \frac{\varepsilon}{\sigma^2 \text{Re}} \langle \bar{\mathbf{u}} \rangle^s, \quad (3.6)$$

$$\nabla \cdot \langle \bar{\mathbf{u}} \rangle^s = 0, \quad (3.7)$$

where $\sigma = \frac{\sqrt{K}}{L^*}$ is the non-dimensional permeability.

3.1.3 Boundary and interface momentum transfer conditions

At the solid walls, no-slip and no-penetration conditions hold. These boundary conditions written in non-dimensional form are

$$\langle \bar{u} \rangle^s = 0, \quad (3.8a)$$

$$\langle \bar{v} \rangle^s = 0, \quad (3.8b)$$

$$\langle \bar{w} \rangle^s = 0. \quad (3.8c)$$

When the porous region is homogeneous and isotropic, and the permeability is sufficiently small to neglect inertial effects, the momentum transfer conditions at the interface with the fluid region are (2.57). Their non-dimensional form is

$$\bar{u} = \langle \bar{u} \rangle^s, \quad (3.9a)$$

$$\bar{v} = \langle \bar{v} \rangle^s, \quad (3.9b)$$

$$\bar{w} = \langle \bar{w} \rangle^s, \quad (3.9c)$$

$$\bar{p} = \langle \bar{p} \rangle, \quad (3.9d)$$

$$\frac{\sigma}{\varepsilon} \frac{\partial \langle \bar{u} \rangle^s}{\partial \bar{y}} - \sigma \frac{\partial \bar{u}}{\partial \bar{y}} = \pm \tau \bar{u}, \quad (3.9e)$$

$$\frac{\sigma}{\varepsilon} \frac{\partial \langle \bar{w} \rangle^s}{\partial \bar{y}} - \sigma \frac{\partial \bar{w}}{\partial \bar{y}} = \pm \tau \bar{w}. \quad (3.9f)$$

where we use the \pm symbol with the positive sign to refer to an interface below the purely fluid region, and with the negative sign to refer to an interface above the purely fluid region. From now on, we will consider only non-dimensional quantities and we will omit, for simplicity, the superscript " - ".

3.2 v - η formulation

In this section, we rewrite the two pairs of equations (3.4) and (3.5), and (3.6) and (3.7) in the primitive variables \mathbf{u} and p with another set of equations, where pressure formally disappears and is replaced by the normal component of vorticity η .

3.2.1 Navier-Stokes equations

The wall-normal component of the vorticity vector η is defined as

$$\eta = \frac{\partial u}{\partial z} - \frac{\partial w}{\partial x}, \quad (3.10)$$

A one-dimensional, second-order, evolution equation for η can be obtained subtracting the x -derivative of the z -component of momentum equation from the z -derivative of the x -component of the same equation. We have

$$\frac{\partial^2 u}{\partial z \partial t} - \frac{\partial^2 w}{\partial x \partial t} = \frac{\partial^2 p}{\partial z \partial x} - \frac{\partial^2 p}{\partial x \partial z} + \frac{1}{\text{Re}} \frac{\partial \nabla^2 u}{\partial z} - \frac{1}{\text{Re}} \frac{\partial \nabla^2 w}{\partial x} + \frac{\partial HU}{\partial z} - \frac{\partial HW}{\partial x}, \quad (3.11)$$

where

$$HU = -\frac{\partial(uu)}{\partial x} - \frac{\partial(uv)}{\partial y} - \frac{\partial(uw)}{\partial z}, \quad (3.12)$$

$$HW = -\frac{\partial(wu)}{\partial x} - \frac{\partial(wv)}{\partial y} - \frac{\partial(ww)}{\partial z}. \quad (3.13)$$

Using the definition (3.10), the equation for the normal vorticity (3.11) can be rewritten as

$$\frac{\partial \eta}{\partial t} = \frac{\partial HU}{\partial z} - \frac{\partial HW}{\partial x} + \frac{1}{\text{Re}} \nabla^2 \eta. \quad (3.14)$$

To obtain an equation for the wall-normal velocity component v free of pressure, we take the laplacian of the y -component of momentum equation (3.4)

$$\frac{\partial \nabla^2 v}{\partial t} = -\frac{\partial \nabla^2 p}{\partial y} + \frac{1}{\text{Re}} \nabla^2 \nabla^2 v + \nabla^2 HV, \quad (3.15)$$

where

$$HV = -\frac{\partial(vu)}{\partial x} - \frac{\partial(vv)}{\partial y} - \frac{\partial(vw)}{\partial z}. \quad (3.16)$$

In order to eliminate the pressure term in (3.15), we use the Poisson equation obtained by taking the divergence of the momentum equation (3.4)

$$\nabla^2 p = \frac{\partial HU}{\partial x} + \frac{\partial HV}{\partial y} + \frac{\partial HW}{\partial z}. \quad (3.17)$$

Therefore, we obtain

$$\frac{\partial \nabla^2 v}{\partial t} = -\frac{\partial^2 HU}{\partial y \partial x} - \frac{\partial^2 HW}{\partial y \partial z} + \frac{\partial^2 HV}{\partial x^2} + \frac{\partial^2 HV}{\partial z^2} + \frac{1}{\text{Re}} \nabla^2 \nabla^2 v. \quad (3.18)$$

Finally, continuity equation (3.5)

$$\frac{\partial u}{\partial x} + \frac{\partial w}{\partial z} = -\frac{\partial v}{\partial y}, \quad (3.19)$$

and the definition of η (3.10)

$$\frac{\partial u}{\partial z} - \frac{\partial w}{\partial x} = \eta, \quad (3.20)$$

form a 4×4 system with equations (3.14) and (3.18) in the unknowns u , v , w and η .

3.2.2 Volume Averaged Navier-Stokes equations

Analogously to the definition (3.10), the wall-normal component of the volume averaged vorticity $\langle \eta \rangle^s$ is defined as

$$\langle \eta \rangle^s = \frac{\partial \langle u \rangle^s}{\partial z} - \frac{\partial \langle w \rangle^s}{\partial x}. \quad (3.21)$$

We apply the same procedure described in sub-section (3.2.1). We subtract the x -derivative of the z -component of momentum equation (3.6) from the z -derivative of the x -component of the same equation. We obtain

$$\frac{\partial^2 \langle u \rangle^s}{\partial z \partial t} - \frac{\partial^2 \langle w \rangle^s}{\partial x \partial t} = \frac{1}{\text{Re}} \left(\frac{\partial \nabla^2 \langle u \rangle^s}{\partial z} - \frac{\partial \nabla^2 \langle w \rangle^s}{\partial x} \right) - \frac{\varepsilon}{\sigma^2 \text{Re}} \left(\frac{\partial \langle u \rangle^s}{\partial z} - \frac{\partial \langle w \rangle^s}{\partial x} \right). \quad (3.22)$$

Exploiting the definition of the wall-normal component of the volume averaged vorticity $\langle \eta \rangle^s$ 3.21, the above equation can be rewritten as follows

$$\frac{\partial \langle \eta \rangle^s}{\partial t} = \frac{1}{\text{Re}} \nabla^2 \langle \eta \rangle^s - \frac{\varepsilon}{\sigma^2 \text{Re}} \langle \eta \rangle^s. \quad (3.23)$$

Note that, differently from equation (3.14), the above equation does not contain any non-linear terms. This is due to the fact that we have considered negligible inertial effects in the porous layers. Moreover, in the above equation there is a zero-order term, $\langle \eta \rangle^s \varepsilon / (\sigma^2 \text{Re})$, which comes from the Darcy drag $\langle \mathbf{u} \rangle^s \varepsilon / (\sigma^2 \text{Re})$ of equation (3.6).

As described for the Navier-Stokes equations, in order to find an equation for $\langle v \rangle^s$ we take the laplacian of the y -component of momentum equation,

$$\frac{\partial \nabla^2 \langle v \rangle^s}{\partial t} = -\varepsilon \nabla^2 \frac{\partial \langle p \rangle}{\partial y} + \frac{1}{\text{Re}} \nabla^2 \nabla^2 \langle v \rangle^s - \frac{\varepsilon}{\sigma^2 \text{Re}} \nabla^2 \langle v \rangle^s \quad (3.24)$$

Average pressure is eliminated from the previous equation by using the Poisson equation

$$\varepsilon \nabla^2 \langle p \rangle^f = 0. \quad (3.25)$$

Differently from equation (3.17), the above equation is homogeneous. Therefore, the volume-averaged pressure $\langle p \rangle^f$ is determined only by boundary conditions at the impermeable wall and by the momentum transfer condition at the interface

with the fluid region. Using equation (3.25), the normal velocity equation (3.24) becomes

$$\frac{\partial \nabla^2 \langle v \rangle^s}{\partial t} = \frac{1}{\text{Re}} \nabla^2 \nabla^2 \langle v \rangle^s - \frac{\varepsilon}{\sigma^2 \text{Re}} \nabla^2 \langle v \rangle^s. \quad (3.26)$$

Note that in the above equation, analogously to equation (3.23), non-linear terms are missing, while is present the laplacian Darcy drag term.

Continuity equation (3.7)

$$\frac{\partial \langle u \rangle^s}{\partial x} + \frac{\partial \langle w \rangle^s}{\partial z} = -\frac{\partial \langle v \rangle^s}{\partial y}, \quad (3.27)$$

and the definition of η (3.21)

$$\frac{\partial \langle u \rangle^s}{\partial z} - \frac{\partial \langle w \rangle^s}{\partial x} = \langle \eta \rangle^s, \quad (3.28)$$

form a 4×4 system with equations (3.23) and (3.26) in the unknowns $\langle u \rangle^s$, $\langle v \rangle^s$, $\langle w \rangle^s$ and $\langle \eta \rangle^s$.

3.2.3 Boundary and interface momentum transfer conditions

Once the equations in the new variables are obtained, next step is to express the boundary conditions (3.8) and (3.9) in the same set of variable. At the solid walls the no-slip and no-penetration conditions hold. Condition (3.8b) remains unchanged, as follows

$$\langle v \rangle^s = 0. \quad (3.29)$$

At the walls, streamwise and spanwise velocities, $\langle u \rangle^s$ and $\langle w \rangle^s$, are zero as their derivatives in x and z directions. Therefore, using the continuity equations (3.7) and the definition of $\langle \eta \rangle^s$ (3.21), we obtain two conditions at the walls, as

$$\frac{d \langle v \rangle^s}{dy} = 0, \quad (3.30)$$

$$\langle \eta \rangle^s = 0. \quad (3.31)$$

At each interface between the fluid region and the porous layers, the momentum transfer conditions (3.9) must be satisfied. The condition (3.9b) remains unchanged

$$v = \langle v \rangle^s, \quad (3.32)$$

while the other conditions need to be transformed. We begin by subtracting the x -derivative of the (3.9c) from the z -derivative of the (3.9a). We obtain

$$\frac{\partial u}{\partial z} - \frac{\partial w}{\partial x} = \frac{\partial \langle u \rangle^s}{\partial z} - \frac{\partial \langle w \rangle^s}{\partial x}, \quad (3.33)$$

which states that the normal vorticity at the interface is continuous, i.e.

$$\eta = \langle \eta \rangle^s. \quad (3.34)$$

Adding the z -derivative of the (3.9c) to the x -derivative of the (3.9a), gives

$$\frac{\partial u}{\partial x} + \frac{\partial w}{\partial z} = \frac{\partial \langle u \rangle^s}{\partial x} + \frac{\partial \langle w \rangle^s}{\partial z}. \quad (3.35)$$

Using the continuity equations (3.5) and (3.7), we obtain

$$\frac{\partial v}{\partial y} = \frac{\partial \langle v \rangle^s}{\partial y}, \quad (3.36)$$

which states that the normal derivative of the normal velocity is continuous at the interface. Next boundary condition is derived by subtracting the x -derivative of the (3.9f) from the z -derivative of the (3.9e). We have

$$\frac{\sigma}{\varepsilon} \frac{\partial^2 \langle u \rangle^s}{\partial y \partial z} - \sigma \frac{\partial^2 u}{\partial y \partial z} - \frac{\sigma}{\varepsilon} \frac{\partial^2 \langle w \rangle^s}{\partial y \partial x} + \sigma \frac{\partial^2 w}{\partial y \partial x} = \pm \tau \frac{\partial u}{\partial z} \mp \tau \frac{\partial w}{\partial x}, \quad (3.37)$$

which can be further simplified by using the definitions of the normal vorticity to

$$\frac{\sigma}{\varepsilon} \frac{\partial \langle \eta \rangle^s}{\partial y} - \sigma \frac{\partial \eta}{\partial y} = \pm \tau \eta. \quad (3.38)$$

adding x -derivative of the (3.9e) to the z -derivative of the (3.9f), we obtain

$$\frac{\sigma}{\varepsilon} \frac{\partial^2 \langle u \rangle^s}{\partial y \partial x} - \sigma \frac{\partial^2 u}{\partial y \partial x} + \frac{\sigma}{\varepsilon} \frac{\partial^2 \langle w \rangle^s}{\partial y \partial z} - \sigma \frac{\partial^2 w}{\partial y \partial z} = \pm \tau \frac{\partial u}{\partial x} \pm \tau \frac{\partial w}{\partial z}. \quad (3.39)$$

Using the continuity equations (3.5) and (3.7), we obtain

$$\frac{\sigma}{\varepsilon} \frac{\partial^2 \langle v \rangle^s}{\partial y^2} - \sigma \frac{\partial^2 v}{\partial y^2} = \pm \tau \frac{\partial v}{\partial y}. \quad (3.40)$$

In order to obtain the last interface condition, we sum the second x -derivative of (3.9d) to the second z -derivative of equation (3.9d). We have

$$\frac{\partial^2 p}{\partial x^2} + \frac{\partial^2 p}{\partial z^2} = \frac{\partial^2 \langle p \rangle}{\partial x^2} + \frac{\partial^2 \langle p \rangle}{\partial z^2}. \quad (3.41)$$

Then, we exploit Poisson's equations (3.17) and (3.25), to obtain

$$\frac{\partial^2 p}{\partial y^2} - \left(\frac{\partial HU}{\partial x} + \frac{\partial HV}{\partial y} + \frac{\partial HW}{\partial z} \right) = \frac{\partial^2 \langle p \rangle}{\partial y^2}. \quad (3.42)$$

To eliminate pressure from the above equations, we take the y -derivatives of equation (3.15)

$$\frac{\partial^2 p}{\partial y^2} = -\frac{\partial^2 v}{\partial t \partial y} + \frac{1}{\text{Re}} \nabla^2 \frac{\partial v}{\partial y} + \frac{\partial HV}{\partial y}, \quad (3.43)$$

and (3.24)

$$\frac{\partial^2 \langle p \rangle}{\partial y^2} = -\frac{1}{\varepsilon} \frac{\partial^2 \langle v \rangle^s}{\partial t \partial y} + \frac{1}{\varepsilon \text{Re}} \nabla^2 \frac{\partial \langle v \rangle^s}{\partial y} - \frac{1}{\sigma^2 \text{Re}} \frac{\partial \langle v \rangle^s}{\partial y}. \quad (3.44)$$

Substituting (3.43) and (3.44) in (3.42), and using (3.36), we obtain

$$\begin{aligned} \left(1 - \frac{1}{\varepsilon}\right) \frac{\partial}{\partial t} \frac{\partial v}{\partial y} - \frac{1}{\text{Re}} \left[\left(1 - \frac{1}{\varepsilon}\right) \left(\frac{\partial^2}{\partial x^2} + \frac{\partial^2}{\partial z^2} \right) \frac{\partial v}{\partial y} + \frac{\partial^3 v}{\partial y^3} - \frac{1}{\varepsilon} \frac{\partial^3 \langle v \rangle^s}{\partial y^3} \right] + \\ - \frac{1}{\sigma^2 \text{Re}} \frac{\partial v}{\partial y} = - \left[\frac{\partial HU}{\partial x} + \frac{\partial HW}{\partial z} \right]. \end{aligned} \quad (3.45)$$

Finally, the the six interface conditions can be summarized as follows

$$v = \langle v \rangle^s, \quad (3.46a)$$

$$\eta = \langle \eta \rangle^s, \quad (3.46b)$$

$$\frac{\partial v}{\partial y} = \frac{\partial \langle v \rangle^s}{\partial y}, \quad (3.46c)$$

$$\frac{\sigma}{\varepsilon} \frac{\partial \langle \eta \rangle^s}{\partial y} - \sigma \frac{\partial \eta}{\partial y} = \pm \tau \eta, \quad (3.46d)$$

$$\frac{\sigma}{\varepsilon} \frac{\partial^2 \langle v \rangle^s}{\partial y^2} - \sigma \frac{\partial^2 v}{\partial y^2} = \pm \tau \frac{\partial v}{\partial y}, \quad (3.46e)$$

$$\begin{aligned} \left(1 - \frac{1}{\varepsilon}\right) \frac{\partial}{\partial t} \frac{\partial v}{\partial y} - \frac{1}{\text{Re}} \left[\left(1 - \frac{1}{\varepsilon}\right) \left(\frac{\partial^2}{\partial x^2} + \frac{\partial^2}{\partial z^2} \right) \frac{\partial v}{\partial y} + \frac{\partial^3 v}{\partial y^3} - \frac{1}{\varepsilon} \frac{\partial^3 \langle v \rangle^s}{\partial y^3} \right] + \\ - \frac{1}{\sigma^2 \text{Re}} \frac{\partial v}{\partial y} = - \left[\frac{\partial HU}{\partial x} + \frac{\partial HW}{\partial z} \right]. \end{aligned} \quad (3.46f)$$

Chapter 4

Non-modal stability

The following chapter is organized in three parts. At the beginning we linearize the v - η equations governing the flow within the fluid and porous regions, and then we write the same equations in wavenumber space. Second part deals with non-modal stability theory. We define a measure of the disturbances suitable for the geometry of our problem and then, we present a discretized version of the energy growth function. In the third part, we discuss the numerical implementation of the stability analysis. We discretize the problem by means of the Chebyshev collocation spectral method, write the discrete eigenvalue problem and discuss the imposition of the boundary conditions. Next, we define the errors used to control the accuracy of the results and we present the algorithm that has been used to compute the maximum value of the energy growth function over the parameter space. Finally, we validate our program recovering the transient growth of Poiseuille flow, as permeability tends to zero.

4.1 Disturbances equations

We linearize the governing equations (3.4) and (3.6) with respect of the laminar velocity profile and we obtain the equations for the perturbations. Then, we exploit the periodicity of the flow in the spanwise and streamwise direction to write the above-mentioned equations into wavenumber space. Finally, we assume that disturbances have an exponential dependence on time, and we write the Orr-Sommerfeld Squire equations for the channel flow, together with their analogous version for the flow thorough the porous medium.

4.1.1 Base flow

In this section, we review the laminar velocity profile obtained by Tilton and Cortelezzi [51]. The expression for the base flow can be obtained by solving equations (2.1) and (2.41) for a steady, plane and parallel flow, driven by a

pressure gradient uniform over the three layers. The problem simplifies to

$$\frac{d^2 u}{dy^2} = \frac{1}{\mu} \frac{dp}{dx}, \quad (4.1)$$

$$\frac{K_j}{\varepsilon_j} \frac{d^2 \langle u \rangle^s}{dy^2} - \langle u \rangle^s = \frac{K_j}{\mu} \frac{dp}{dx}, \quad (4.2)$$

where we replaced $d\langle p \rangle^f/dx$ with dp/dx because the same pressure gradient drives the fluid in the three regions. Note that all the quantities are dimensional. Equations (4.1) and (4.2) are coupled at the interfaces, $y = \pm h$, by the Ochoa-Tapia and Withaker boundary conditions (2.57). The porous regions are assumed to be semi-infinite, causing the laminar profile to lack the boundary layers at the solid walls. This assumption can be motivated in two ways. Firstly, in the momentum equation (2.41) governing the porous layer the base flow does not appear explicitly; secondly, we can recover the presence of the impermeable walls when we impose the boundary conditions of the discretized eigenvalue problem. This assumption simplifies the numerical evaluation of the base flow near the solid walls, when the permeability is small. The non-dimensional laminar velocity profile in the channel region is

$$U = C \left[y^2 + \frac{B_1 - B_2}{A_1 - A_2} y + \frac{D}{A_1 - A_2} \right], \quad (4.3)$$

while in the porous region the profile is

$$\langle U_j \rangle^s = C \left\{ \left[2\sigma_j^2 + 1 + \frac{\pm(B_2 - B_1) + D}{A_1 - A_2} \right] e^{(1 \pm y) \frac{\sqrt{\varepsilon_j}}{\sigma_j}} - 2\sigma_j^2 \right\}, \quad j = 1, 2, \quad (4.4)$$

where

$$\begin{aligned} D &= B_1 A_2 - B_2 A_1, \\ C &= \left[\frac{1}{3} + \frac{D}{A_1 - A_2} \right]^{-1}, \\ A_j &= \pm 1 \pm \sigma_j \left[\frac{1}{\sqrt{\varepsilon_j}} - \tau_j \right]^{-1}, \quad j = 1, 2, \\ B_j &= 2\sigma_j^2 + 1 + 2\sigma_j [1 + \tau_j \sigma_j] \left[\frac{1}{\sqrt{\varepsilon_j}} - \tau_j \right]^{-1}, \quad j = 1, 2. \end{aligned}$$

4.1.2 Linearized equations

We start considering the v - η equations (3.18) and (3.14) derived in subsection 3.2.1, that we report here for convenience,

$$\frac{\partial \eta}{\partial t} = \frac{\partial H U}{\partial z} - \frac{\partial H W}{\partial x} + \frac{1}{\text{Re}} \nabla^2 \eta$$

$$\frac{\partial \nabla^2 v}{\partial t} = -\frac{\partial^2 HU}{\partial y \partial x} - \frac{\partial^2 HW}{\partial y \partial z} + \frac{\partial^2 HV}{\partial x^2} + \frac{\partial^2 HV}{\partial z^2} + \frac{1}{\text{Re}} \nabla^2 \nabla^2 v.$$

To linearize the above equations, we write the velocity as the superimposition of the base flow $\mathbf{U} = (U(y), 0, 0)$ with small amplitude perturbations $\bar{\mathbf{u}}(x, y, z, t)$ as

$$\mathbf{u} = \mathbf{U} + \bar{\mathbf{u}}. \quad (4.5)$$

where

$$\frac{\|\bar{\mathbf{u}}\|}{\|\mathbf{U}\|} \ll 1.$$

Note that the hypothesis of parallel flow implies that the v - η perturbed variables are

$$v = \bar{v}, \quad \eta = \bar{\eta}. \quad (4.6)$$

The first step of the linearization is to substitute the perturbed variables (4.5) into the non-linear terms (3.12), (3.16) and (3.13). We have

$$HU = -2\bar{u} \frac{\partial \bar{u}}{\partial x} - \bar{v} \frac{\partial \bar{u}}{\partial y} - \bar{w} \frac{\partial \bar{u}}{\partial z} - U \frac{\partial \bar{u}}{\partial x} - U' \bar{v}, \quad (4.7a)$$

$$HV = -\bar{u} \frac{\partial \bar{v}}{\partial x} - 2\bar{v} \frac{\partial \bar{v}}{\partial y} - \bar{w} \frac{\partial \bar{v}}{\partial z} - U \frac{\partial \bar{v}}{\partial x} - \bar{v} \frac{\partial \bar{u}}{\partial x} - \bar{v} \frac{\partial \bar{w}}{\partial z}, \quad (4.7b)$$

$$HW = -\bar{u} \frac{\partial \bar{w}}{\partial x} - \bar{v} \frac{\partial \bar{w}}{\partial y} - 2\bar{w} \frac{\partial \bar{w}}{\partial z} - U \frac{\partial \bar{w}}{\partial x} - \bar{w} \frac{\partial \bar{u}}{\partial x} - \bar{w} \frac{\partial \bar{v}}{\partial y}, \quad (4.7c)$$

where the subscript " ' " denotes a derivative with respect to the wall-normal direction. After substituting the above relations into equations (3.18) and (3.14), and neglecting second and higher order terms, we obtain the linearized version of the v - η equations for the purely fluid region, as follows

$$\left(\frac{\partial}{\partial t} + U \frac{\partial}{\partial x} \right) \nabla^2 \bar{v} - \frac{\partial \bar{v}}{\partial x} - \frac{1}{\text{Re}} \nabla^4 \bar{v} = 0 \quad (4.8)$$

$$\left(\frac{\partial}{\partial t} + U \frac{\partial}{\partial x} \right) \bar{\eta} - \frac{1}{\text{Re}} \nabla^2 \bar{\eta} = -U' \frac{\partial \bar{v}}{\partial z}. \quad (4.9)$$

Now, we focus on the equations (3.26) and (3.23) that govern the flow in the porous regions. We observe that they are already linear and consequently, the equations for the perturbations are

$$\left(\frac{\partial}{\partial t} - \frac{\varepsilon}{\sigma^2 \text{Re}} \right) \nabla^2 \bar{v} - \frac{1}{\text{Re}} \nabla^4 \langle \bar{v} \rangle^s = 0, \quad (4.10)$$

$$\left(\frac{\partial}{\partial t} - \frac{\varepsilon}{\sigma^2 \text{Re}} \right) \bar{\eta} - \frac{1}{\text{Re}} \nabla^2 \langle \bar{\eta} \rangle^s = 0, \quad (4.11)$$

where $\langle \bar{v} \rangle^s$ and $\langle \bar{\eta} \rangle^s$ are the perturbed volume-averaged variables, deriving from the decomposition

$$\langle \mathbf{u} \rangle^s = \langle \mathbf{U} \rangle^s + \langle \bar{\mathbf{u}} \rangle^s. \quad (4.12)$$

Equations (4.10) and (4.11) governing the flow through a porous medium, differently from (4.8) and (4.9), are fully uncoupled and do not involve the base flow in the porous regions.

Finally, we consider the boundary conditions (3.8) and (3.46). Among all, equation (3.46f) is the only relation which contains non-linear terms. Linearization yields to

$$\begin{aligned} \left(1 - \frac{1}{\varepsilon}\right) \frac{\partial}{\partial t} \frac{\partial \bar{v}}{\partial y} - \frac{1}{\text{Re}} \left[\left(1 - \frac{1}{\varepsilon}\right) \left(\frac{\partial^2}{\partial x^2} + \frac{\partial^2}{\partial z^2} \right) \frac{\partial \bar{v}}{\partial y} + \frac{\partial^3 \bar{v}}{\partial y^3} - \frac{1}{\varepsilon} \frac{\partial^3 \langle \bar{v} \rangle^s}{\partial y^3} \right] + \\ - \frac{1}{\sigma^2 \text{Re}} \frac{\partial^2 \bar{v}}{\partial x \partial y} + U \frac{\partial \bar{v}}{\partial y} - U' \frac{\partial \bar{v}}{\partial x} = 0. \end{aligned} \quad (4.13)$$

The first derivative of the base flow $U'(y)$ is discontinuous at the interface between the purely fluid region and the porous layer. Following Tilton and Cortelezzi [51], we will evaluate such a derivative using the value assumed at the fluid side of the interface.

4.1.3 Modal equations

Our study considers a flow periodic in the streamwise and spanwise directions. This property can be exploited by expressing the perturbed variables in terms of harmonic functions. In the purely fluid region we have

$$\bar{v}(x, y, z, t) = \hat{v}(y, t) e^{i(\alpha x + \beta z)}, \quad (4.14)$$

$$\bar{\eta}(x, y, z, t) = \hat{\eta}(y, t) e^{i(\alpha x + \beta z)}, \quad (4.15)$$

while for each porous layer we have

$$\langle \bar{v} \rangle^s(x, y, z, t) = \hat{v}_p(y, t) e^{i(\alpha x + \beta z)}, \quad (4.16)$$

$$\langle \bar{\eta} \rangle^s(x, y, z, t) = \hat{\eta}_p(y, t) e^{i(\alpha x + \beta z)}, \quad (4.17)$$

where \hat{v} , $\hat{\eta}$, \hat{v}_p and $\hat{\eta}_p$ are the Fourier coefficients of the perturbations, for given wavenumbers α and β , and the subscript p is used to denote volume-averaged quantities in the porous medium. By substituting the above relations into equations (4.8)-(4.11), we obtain for the purely fluid region

$$\left[\left(\frac{\partial}{\partial t} + i\alpha U \right) (D^2 - k^2) - i\alpha U'' - \frac{1}{\text{Re}} (D^2 - k^2)^2 \right] \hat{v} = 0, \quad (4.18)$$

$$\left[\left(\frac{\partial}{\partial t} + i\alpha U \right) - \frac{1}{\text{Re}} (D^2 - k^2) \right] \hat{\eta} = -i\beta U' \hat{v}, \quad (4.19)$$

and for each porous layer

$$\left[\left(\frac{\partial}{\partial t} - \frac{\varepsilon}{\sigma^2 \text{Re}} \right) (D^2 - k^2) - \frac{1}{\text{Re}} (D^2 - k^2)^2 \right] \hat{v}_p = 0, \quad (4.20)$$

$$\left[\left(\frac{\partial}{\partial t} - \frac{\varepsilon}{\sigma^2 \text{Re}} \right) - \frac{1}{\text{Re}} (D^2 - k^2) \right] \hat{\eta}_p = 0, \quad (4.21)$$

where symbol D denotes the derivative with respect to the wall-normal coordinate, and k is the magnitude of the wave vector $\mathbf{k} = (\alpha, 0, \beta)$, defined as

$$k^2 = \alpha^2 + \beta^2. \quad (4.22)$$

The above equations are first-order differential equations in time, describing the temporal evolution of the Fourier coefficients. Also, note that equations (4.20) and (4.21) are not valid for high values of the wavenumbers α and β , because the disturbances may have wavelengths of the order of the radius of the averaging volumes.

We assume a harmonic time dependence of the perturbations, i.e.,

$$\hat{v}(y, t) = \tilde{v}(y)e^{-i\omega t}, \quad (4.23)$$

$$\hat{\eta}(y, t) = \tilde{\eta}(y)e^{-i\omega t}, \quad (4.24)$$

$$\hat{v}_p(y, t) = \tilde{v}_p(y)e^{-i\omega t}, \quad (4.25)$$

$$\hat{\eta}_p(y, t) = \tilde{\eta}_p(y)e^{-i\omega t}, \quad (4.26)$$

where the frequency is defined as $\omega = \alpha c$. Therefore, the perturbations are traveling waves characterized by a wave vector \mathbf{k} and phase c . The amplitude of this disturbances is a function of the wall-normal direction only. Since in this study we focus on a temporal stability analysis, the wavenumbers α and β are chosen real, while the phase speed and amplitude functions are in general complex. If we write $c = c_r + ic_i$, a perturbation becomes unstable if $c_i > 0$. By substituting the above relations into equations (4.18) and (4.19), we obtain the well-known Orr-Sommerfeld Squire equations,

$$\left[(\alpha U - \omega) (D^2 - \kappa^2) - \alpha U'' - \frac{1}{i\text{Re}} (D^2 - \kappa^2)^2 \right] \tilde{v}(y) = 0, \quad (4.27)$$

$$\left[(\alpha U - \omega) - \frac{1}{i\text{Re}} (D^2 - \kappa^2) \right] \tilde{\eta}(y) = -\beta U' \tilde{v}, \quad (4.28)$$

while, by substituting relations (4.23)-(4.26) into equations (4.20) and (4.21), we obtain

$$\left[\left(\frac{\varepsilon}{i\sigma^2 \text{Re}} - \omega \right) (D^2 - \kappa^2) - \frac{1}{i\text{Re}} (D^2 - \kappa^2)^2 + \right] \tilde{v}_p(y) = 0, \quad (4.29)$$

$$\left[\frac{\varepsilon}{i\sigma^2 \text{Re}} - \omega - \frac{1}{i\text{Re}} (D^2 - \kappa^2) \right] \tilde{\eta}_p(y) = 0, \quad (4.30)$$

which can be seen as the porous counterpart of the Orr-Sommerfeld Squire equations.

At the impermeable walls, volume-averaged variables satisfy no-penetration

and no-slip conditions,

$$\tilde{v}_p = 0, \quad (4.31a)$$

$$\tilde{\eta}_p = 0, \quad (4.31b)$$

$$\frac{d\tilde{v}_p}{dy} = 0, \quad (4.31c)$$

while at the interface between the porous layer and the porous fluid region, we have the momentum transfer conditions

$$\tilde{v} = \tilde{v}_p, \quad (4.32a)$$

$$\tilde{\eta} = \tilde{\eta}_p, \quad (4.32b)$$

$$\frac{d\tilde{v}}{dy} = \frac{d\tilde{v}_p}{dy}, \quad (4.32c)$$

$$\frac{\sigma}{\varepsilon} \frac{d\tilde{\eta}_p}{dy} - \sigma \frac{d\tilde{\eta}}{dy} = \pm \tau \tilde{\eta}, \quad (4.32d)$$

$$\frac{\sigma}{\varepsilon} \frac{d^2 \tilde{v}_p}{dy^2} - \sigma \frac{d^2 \tilde{v}}{dy^2} = \pm \tau \frac{d\tilde{v}}{dy}, \quad (4.32e)$$

$$\left[\left(\frac{1}{\varepsilon} - 1 \right) \left(i\omega - \frac{\kappa^2}{\text{Re}} \right) - \frac{1}{\sigma^2 \text{Re}} + i\alpha U \right] \frac{d\tilde{v}}{dy} + \frac{1}{\varepsilon \text{Re}} \frac{d^3 \tilde{v}_p}{dy^3} - \frac{1}{\text{Re}} \frac{d^3 \tilde{v}}{dy^3} - i\alpha U' \tilde{v} = 0. \quad (4.32f)$$

Considering the geometry of our problem, we write equations (4.27)-(4.30) in matrix form, as follows

$$-i\omega \begin{pmatrix} k^2 - D^2 & 0 \\ 0 & 1 \end{pmatrix} \begin{pmatrix} \tilde{v}_2 \\ \tilde{\eta}_2 \end{pmatrix} + \begin{pmatrix} \mathcal{L}_2^{OS} & 0 \\ 0 & \mathcal{L}_2^{SQ} \end{pmatrix} \begin{pmatrix} \tilde{v}_2 \\ \tilde{\eta}_2 \end{pmatrix} = 0, \quad (4.33a)$$

$$-i\omega \begin{pmatrix} k^2 - D^2 & 0 \\ 0 & 1 \end{pmatrix} \begin{pmatrix} \tilde{v} \\ \tilde{\eta} \end{pmatrix} + \begin{pmatrix} \mathcal{L}^{OS} & 0 \\ i\beta U' & \mathcal{L}^{SQ} \end{pmatrix} \begin{pmatrix} \tilde{v} \\ \tilde{\eta} \end{pmatrix} = 0, \quad (4.33b)$$

$$-i\omega \begin{pmatrix} k^2 - D^2 & 0 \\ 0 & 1 \end{pmatrix} \begin{pmatrix} \tilde{v}_1 \\ \tilde{\eta}_1 \end{pmatrix} + \begin{pmatrix} \mathcal{L}_1^{OS} & 0 \\ 0 & \mathcal{L}_1^{SQ} \end{pmatrix} \begin{pmatrix} \tilde{v}_1 \\ \tilde{\eta}_1 \end{pmatrix} = 0, \quad (4.33c)$$

and

$$(4.34)$$

where

$$\mathcal{L}^{OS} = i\alpha U (k^2 - D^2) + i\alpha U'' + \frac{1}{\text{Re}} (k^2 - D^2)^2, \quad (4.35)$$

$$\mathcal{L}^{SQ} = i\alpha U + \frac{1}{\text{Re}} (k^2 - D^2), \quad (4.36)$$

$$\mathcal{L}_j^{OS} = \frac{\varepsilon_j}{i\sigma_j^2 \text{Re}} (k^2 - D^2) + \frac{1}{\text{Re}} (k^2 - D^2)^2, \quad j = \dots 1, 2 \quad (4.37)$$

$$\mathcal{L}_j^{SQ} = \frac{\varepsilon_j}{i\sigma_j^2 \text{Re}} + \frac{1}{\text{Re}} (k^2 - D^2), \quad j = \dots 1, 2. \quad (4.38)$$

Furthermore, if we define the state vector

$$\hat{\boldsymbol{\zeta}} = \begin{pmatrix} \hat{v}_2 \\ \hat{\eta}_2 \\ \hat{v} \\ \hat{\eta} \\ \hat{v}_1 \\ \hat{\eta}_1 \end{pmatrix}, \quad (4.39)$$

we can assemble equations (4.33) into a more compact form. We have

$$\mathcal{L}\hat{\boldsymbol{\zeta}} = -i\omega\mathcal{M}\hat{\boldsymbol{\zeta}}, \quad (4.40)$$

where

$$\mathcal{L} = \begin{pmatrix} \mathcal{L}_2^{OS} & 0 & 0 & 0 & 0 & 0 \\ 0 & \mathcal{L}_2^{SQ} & 0 & 0 & 0 & 0 \\ 0 & 0 & \mathcal{L}^{OS} & 0 & 0 & 0 \\ 0 & 0 & \mathcal{L}^C & \mathcal{L}^{SQ} & 0 & 0 \\ 0 & 0 & 0 & 0 & \mathcal{L}_1^{OS} & 0 \\ 0 & 0 & 0 & 0 & 0 & \mathcal{L}_1^{SQ} \end{pmatrix}, \quad (4.41)$$

and

$$\mathcal{M} = \begin{pmatrix} k^2 - D^2 & 0 & 0 & 0 & 0 & 0 \\ 0 & 1 & 0 & 0 & 0 & 0 \\ 0 & 0 & k^2 - D^2 & 0 & 0 & 0 \\ 0 & 0 & 0 & 1 & 0 & 0 \\ 0 & 0 & 0 & 0 & k^2 - D^2 & 0 \\ 0 & 0 & 0 & 0 & 0 & 1 \end{pmatrix}. \quad (4.42)$$

Equation (4.40) is a generalized eigenvalue problem, where the eigenvalue is the frequency ω and the eigenfunction is $\hat{\boldsymbol{\zeta}}$. Note that matrix \mathcal{M} is block diagonal, whereas block diagonal matrix \mathcal{L} has the off-diagonal block entry \mathcal{L}^C . This block one-way couples the Orr-Sommerfeld with the Squire equations in the fluid region. Finally, we rewrite the momentum transfer conditions (4.32) in matrix form, as follows

$$\mathcal{C}\hat{\boldsymbol{\zeta}} = \mathbf{0}, \quad (4.43)$$

where

$$\mathbf{C} = \begin{pmatrix} 1 & 0 & -1 & 0 & 0 & 0 \\ 0 & 0 & -1 & 0 & 1 & 0 \\ 0 & 1 & 0 & -1 & 0 & 0 \\ 0 & 0 & 0 & -1 & 0 & 1 \\ D & 0 & -D & 0 & 0 & 0 \\ 0 & 0 & -D & 0 & D & 0 \\ 0 & \frac{\sigma_2}{\varepsilon_2} D & 0 & -\sigma_2 D - \tau_2 & 0 & 0 \\ 0 & 0 & 0 & -\sigma_1 D + \tau_1 & 0 & \frac{\sigma_1}{\varepsilon_1} \\ \frac{\sigma_2}{\varepsilon_2} D^2 & 0 & -\sigma_2 D^2 - \tau_2 D & 0 & 0 & 0 \\ 0 & 0 & -\sigma_1 D^2 + \tau_1 D & 0 & \frac{\sigma_1}{\varepsilon_1} D^2 & 0 \\ \frac{1}{\varepsilon_2 \text{Re}} D^3 & 0 & q(\varepsilon_2, \sigma_2) & 0 & 0 & 0 \\ 0 & 0 & q(\varepsilon_1, \sigma_1) & 0 & 1/(\varepsilon_1 \text{Re}) D^3 & 0 \end{pmatrix}, \quad (4.44)$$

where

$$q(\varepsilon, \sigma) = \left[\left(\frac{1}{\varepsilon} - 1 \right) \left(i\omega - \frac{\kappa^2}{\text{Re}} \right) - \frac{1}{\sigma^2 \text{Re}} + i\alpha U \right] D - \frac{1}{\text{Re}} D^3 - i\alpha U'. \quad (4.45)$$

By observing the matrix \mathbf{C} , we note that the interface conditions couple the modal equations that govern the flow in the porous regions with the Orr-Sommerfeld Squire equations.

4.2 Non-modal analysis

In wall-bounded flows such as plane Poiseuille and plane Couette flows, the critical Reynolds number predicted by linear stability analysis is in disagreement with the experimentally observed transitional Reynolds number [42]. This discrepancy is theoretically justified by the transient growth of the amplitude of perturbations, which can occur even if the base flow is linearly stable, see e.g. [19, 37]. Transient growth is possible because the eigenvectors of modal problems are non-orthogonal, allowing for non-monotonic growth of the energy of the disturbances [38]. Non-modal analysis studies the maximum possible energy growth that can occur for all the possible non zero initial conditions. If the amplitude of disturbances grows sufficiently, the non-linear terms become dominant and transition to turbulence may occur.

4.2.1 Energy of the disturbances

We choose a norm proportional to the kinetic energy of the perturbations to study the short-time impact of the disturbances. Other choices are possible,

but we preferred a kinetic energy based norm because it is physical meaningful and can be measured in experiments. Considering the layered geometry of our problem, kinetic energy of disturbances per spanwise and streamwise unit length can be expressed as

$$E = \frac{1}{2} \int_{-1-2h_1}^{-1} \langle \mathbf{u}_1 \rangle^s \cdot \langle \mathbf{u}_1 \rangle^s dy + \int_{-1}^1 \mathbf{u} \cdot \mathbf{u} dy + \int_1^{1+2h_2} \langle \mathbf{u}_2 \rangle^s \cdot \langle \mathbf{u}_2 \rangle^s dy. \quad (4.46)$$

Following Gustavsson [20], we rewrite the previous equation in Fourier space in terms of the variables v - η , as follows

$$\begin{aligned} E &= \frac{1}{2k^2} \int_{-1-2h_1}^{-1} (|\mathrm{D} \hat{v}_1|^2 + |\hat{v}_1|^2 + |\hat{\eta}_1|) dy + \\ &+ \frac{1}{2k^2} \int_{-1}^1 (|\mathrm{D} \hat{v}|^2 + |\hat{v}|^2 + |\hat{\eta}|) dy + \\ &+ \frac{1}{2k^2} \int_1^{1+2h_2} (|\mathrm{D} \hat{v}_2|^2 + |\hat{v}_2|^2 + |\hat{\eta}_2|) dy. \end{aligned} \quad (4.47)$$

Analogously to Reddy and Hennigson [37], we define the inner scalar product associated to the kinetic energy

$$\begin{aligned} (\hat{\boldsymbol{\zeta}}_r, \hat{\boldsymbol{\zeta}}_s) &= \int_{-1-2h_1}^{-1} (\mathrm{D} \hat{v}_{1r}^* \mathrm{D} \hat{v}_{1s} + \hat{v}_{1r}^* \hat{v}_{1s} + \hat{\eta}_{1r}^* \hat{\eta}_{1s}) dy + \\ &+ \int_{-1}^1 (\mathrm{D} \hat{v}_r^* \mathrm{D} \hat{v}_s + \hat{v}_r^* \hat{v}_s + \hat{\eta}_r^* \hat{\eta}_s) dy + \\ &+ \int_1^{1+2h_2} (\mathrm{D} \hat{v}_{2r}^* \mathrm{D} \hat{v}_{2s} + \hat{v}_{2r}^* \hat{v}_{2s} + \hat{\eta}_{2r}^* \hat{\eta}_{2s}) dy, \end{aligned} \quad (4.48)$$

where the subscripts r and s denote two arbitrary eigenfunctions of the problem (4.40). As a consequence, the related induced norm is

$$\|\hat{\boldsymbol{\zeta}}\|_E^2 = (\hat{\boldsymbol{\zeta}}, \hat{\boldsymbol{\zeta}}), \quad (4.49)$$

which is proportional to the kinetic energy (4.47).

4.2.2 Maximum energy growth

In order to quantify the transient growth of disturbances in our problem, we are interested in the maximum possible amplification of their energy, described by the following function

$$G(t) = \max_{\hat{\boldsymbol{\zeta}}_0 \neq 0} \frac{\|\hat{\boldsymbol{\zeta}}(t)\|_E^2}{\|\hat{\boldsymbol{\zeta}}_0\|_E^2}, \quad (4.50)$$

where $\hat{\zeta}_0 = \zeta(t = 0)$ is a given initial condition. To compute numerically $G(t)$, we derive a discrete version of equation 4.50 following the procedure described in [37]. First, we approximate the Fourier coefficients $\hat{\zeta}$ as

$$\hat{\zeta}(y, t) \approx \hat{\zeta}_K(y, t) = \sum_{j=1}^K \kappa_j(t) \tilde{\zeta}_j(y), \quad (4.51)$$

where $\tilde{\zeta}_j(y)$ are the first K eigenfunctions of the problem (4.40), ordered with decreasing imaginary part, and $\kappa_j(t)$ are time dependent coefficients. Note that approximation (4.51) is valid only if the problem is linearly stable and K is sufficiently large. Then, the discrete version of the growth function is

$$G_K(t) = \sup_{\hat{\zeta}_{K,0} \neq 0} \frac{\|\hat{\zeta}_K(t)\|_E^2}{\|\hat{\zeta}_{K,0}\|_E^2}, \quad (4.52)$$

which converges to the function $G(t)$ as $K \rightarrow \infty$. By exploiting the discretization introduced with equation (4.51), we express the inner product (4.48) in matrix form, as follows

$$(\hat{\zeta}_r, \hat{\zeta}_s) = \boldsymbol{\kappa}_r^H \mathbf{W} \boldsymbol{\kappa}_s, \quad (4.53)$$

where $\boldsymbol{\kappa} = (\kappa_1, \dots, \kappa_K)^T$ is the vector collecting the time coefficients $\kappa_j(t)$ associated to $\hat{\zeta}$, and \mathbf{W} is a weight matrix, whose elements are

$$W_{ij} = (\tilde{\zeta}_i, \tilde{\zeta}_j), \quad i, j = 1, \dots, K. \quad (4.54)$$

Next, we factor the weight matrix \mathbf{W} as

$$\mathbf{W} = \mathbf{F}^H \mathbf{F}. \quad (4.55)$$

Note that matrix \mathbf{F} satisfies the identity

$$\|\mathbf{B}\|_E = \|\mathbf{F} \mathbf{B} \mathbf{F}^{-1}\|_2, \quad (4.56)$$

where $\|\cdot\|_2$ is the Euclidean two-norm, and \mathbf{B} is a complex matrix. Finally, by exploiting identity (4.56), we obtain a practical formula for evaluating $G_K(t)$. We have

$$G_K(t) = \|\mathbf{F} \exp(-it\boldsymbol{\Omega}) \mathbf{F}^{-1}\|_2^2, \quad (4.57)$$

where $\boldsymbol{\Omega} = \text{diag}\{\omega_1, \dots, \omega_K\}$ is a diagonal matrix in which the diagonal terms are the first K eigenvalues ordered with decreasing imaginary part.

4.3 Numerical implementation

In this section we present the numerical methodology used to compute the discrete growth function $G_K(t)$. To this end, we express the amplitude of the perturbations by means of the Chebyshev polynomial expansions and then, we collocate

the modal equations (4.27), (4.28), (4.29), (4.30) and the related boundary conditions, on a grid of Gauss-Lobatto nodes placed along the wall-normal coordinate. Next, we assemble the discrete counterpart of eigenvalue problem (4.40) and we discuss the numerical imposition of the boundary conditions. Finally, we define the discretization errors used to ensure accuracy of the results, present the adaptive algorithm used to explore the parameter space with given error tolerances, and validate our program.

4.3.1 Chebyshev collocation method

According Orszag [33], the use of the Chebyshev polynomials to discretize the Orr-Sommerfeld and Squire operators, allows one to obtain results of greater accuracy at lower computational cost, than finite differences methods. We refer the reader to [7, 18] for the details concerning Chebyshev polynomial theory, and to [42, 49, 51] for the application of the method to fluid dynamics stability problems.

Because Chebyshev polynomials are defined in the interval $[-1, 1]$, we start mapping the wall-normal coordinate in each of the three-layers to this interval. We have the identity map

$$\begin{aligned} y(\xi) : [-1, 1] &\longrightarrow [-1, 1], \\ y &= \xi, \end{aligned} \tag{4.58}$$

for the central fluid region, while for the two porous layers we have

$$\begin{aligned} y(\xi_1) : [-1, 1] &\longrightarrow [-1 - 2h_1, -1], \\ y &= -1 + h_1(\xi_1 - 1), \end{aligned} \tag{4.59}$$

and

$$\begin{aligned} y(\xi_2) : [-1, 1] &\longrightarrow [1, 1 + 2h_2], \\ y &= 1 + h_2(\xi_2 + 1). \end{aligned} \tag{4.60}$$

Then, we approximate the amplitude functions using the following Chebyshev expansions

$$\begin{aligned} \tilde{v} &= \sum_{n=0}^N r_n T_n(\xi), & \tilde{\eta} &= \sum_{n=0}^N \rho_n T_n(\xi), \\ \tilde{v}_1 &= \sum_{n=0}^N f_n T_n(\xi_1), & \tilde{\eta}_1 &= \sum_{n=0}^N \phi_n T_n(\xi_1), \\ \tilde{v}_2 &= \sum_{n=0}^N g_n T_n(\xi_2), & \tilde{\eta}_2 &= \sum_{n=0}^N \gamma_n T_n(\xi_2), \end{aligned} \tag{4.61}$$

where the symbol $\mathbf{0}$ denotes a $(N + 1) \times (N + 1)$ matrix full of zeros. Equation (4.65) represents in matrix form a system of $6N + 6$ equations in $6N + 6$ unknowns. However, boundary conditions must be imposed in order to compute the correct eigenvalues. This can be done by substituting the Chebyshev expansions (4.61) into the boundary conditions at the impermeable walls (4.31) and into the momentum transfer conditions (4.32) at each interface. In the following we list the resulting eighteen relations. Note that for simplicity $\sum_{k=0}^N$ is implied.

- At the upper impermeable wall, the volume-averaged perturbation amplitudes \tilde{v}_2 and $\tilde{\eta}_2$ satisfy no-penetration and no-slip conditions,

$$g_n T_n(1) = 0, \quad (4.68a)$$

$$g_n \frac{1}{h_2} T_n^{(1)}(1) = 0, \quad (4.68b)$$

$$\gamma_n T_n(1) = 0. \quad (4.68c)$$

- At the upper interface, momentum transfer conditions (4.32) couple \tilde{v}_2 and $\tilde{\eta}_2$ with \tilde{v} and $\tilde{\eta}$,

$$r_n T_n(1) - g_n T_n(-1) = 0, \quad (4.68d)$$

$$r_n T_n^{(1)}(1) - g_n \frac{1}{h_2} T_n^{(1)}(-1) = 0, \quad (4.68e)$$

$$-g_n \frac{\sigma_2}{\varepsilon_2 h_2^2} T_n^{(2)}(-1) + r_n (\sigma_2 T_n^{(2)}(1) - \tau_2 T_n^{(1)}(1)) = 0, \quad (4.68f)$$

$$\rho_n T_n(1) - \gamma_n T_n(-1) = 0, \quad (4.68g)$$

$$\gamma_n \frac{\sigma_2}{\varepsilon_2 h_2} T_n^{(1)}(-1) + \rho_n (-\sigma_2 T_n^{(1)}(1) + \tau_2 T_n^{(0)}(1)) = 0, \quad (4.68h)$$

$$\begin{aligned} r_n \left(\left(- \left(\frac{1}{\varepsilon_2} - 1 \right) \frac{\kappa^2}{\text{Re}} - \frac{1}{\sigma_2^2 \text{Re}} + i\alpha U(y = h) \right) T_n^{(1)}(1) + \right. \\ \left. - \frac{1}{\text{Re}} T_n^{(3)}(1) - i\alpha U'(y = h) T_n(1) \right) + g_n \frac{1}{\varepsilon_2 \text{Re} h_2^3} T_n^{(3)}(-1) = \\ = -\omega r_n i \left(\frac{1}{\varepsilon_2} - 1 \right) T_n^{(1)}(1), \end{aligned} \quad (4.68i)$$

- At the lower interface, momentum transfer conditions (4.32) couple \tilde{v}_1 and

$\tilde{\eta}_1$ with \tilde{v} and $\tilde{\eta}$,

$$r_n T_n(-1) - f_n T_n(1) = 0, \quad (4.68j)$$

$$r_n T_n^{(1)}(-1) - f_n \frac{1}{h_1} T_n^{(1)}(1) = 0, \quad (4.68k)$$

$$-f_n \frac{\sigma_1}{\varepsilon_1 h_1^2} T_n^{(2)}(1) + r_n (\sigma_1 T_n^{(2)}(-1) + \tau_1 T_n^{(1)}(-1)) = 0, \quad (4.68l)$$

$$\rho_n T_n(-1) - \phi_n T_n(1) = 0, \quad (4.68m)$$

$$\phi_n \frac{\sigma_1}{\varepsilon_1 h_1} T_n^{(1)}(1) + \rho_n (-\sigma_1 T_n^{(1)}(-1) - \tau_1 T_n^{(0)}(-1)) = 0, \quad (4.68n)$$

$$\begin{aligned} r_n \left(\left(- \left(\frac{1}{\varepsilon_1} - 1 \right) \frac{\kappa^2}{\text{Re}} - \frac{1}{\sigma_1^2 \text{Re}} + i\alpha U(y = -h) \right) T_n^{(1)}(-1) + \right. \\ \left. - \frac{1}{\text{Re}} T_n^{(3)}(-1) - i\alpha U'(y = -h) T_n(-1) \right) + f_n \frac{1}{\varepsilon_1 \text{Re} h_1^3} T_n^{(3)}(1) = \\ = -\omega r_n i \left(\frac{1}{\varepsilon_1} - 1 \right) T_n^{(1)}(-1). \end{aligned} \quad (4.68o)$$

- At the lower impermeable wall, volume-averaged perturbation amplitudes satisfy no-penetration and no slip conditions,

$$\phi_n T_n(-1) = 0, \quad (4.68p)$$

$$f_n T_n(-1) = 0, \quad (4.68q)$$

$$f_n \frac{1}{h_1} T_n^{(1)}(-1) = 0. \quad (4.68r)$$

In the above equations, $T_n^{(j)}$ denotes the j th derivative with respect to y of the n th Chebyshev polynomial.

To impose the boundary conditions we replace eighteen rows of the matrix problem (4.65) with eighteen relations (4.68). Note that discrete conditions in which the eigenvalue ω does not appear explicitly have the form

$$(e_1 \cdots e_i \cdots e_{6N+6}) \mathbf{x} = (0 \cdots 0 \cdots 0) \mathbf{x}, \quad (4.69)$$

where e_i are coefficients that depend on considered relation among the (4.68). Therefore, replacing rows of the matrix problem (4.65) with relations like the (4.69), produces rows of zeros in matrix \mathbf{B} , which becomes singular. Following Schmid and Henningson [42], we rewrite (4.69) as

$$(e_1 \cdots e_i \cdots e_{6N+6}) \mathbf{x} = m(e_1 \cdots e_i \cdots e_{6N+6}) \mathbf{x}, \quad (4.70)$$

where m is an imaginary number. As consequence, we introduce a number of spurious eigenvalue equal to the number of conditions that have been modified

using formula (4.70). Such non-physical eigenvalues have real part equal to zero, and imaginary part equal to m , and so they can be removed easily. Rows to be substituted by the boundary conditions (4.68) can not be chosen randomly, but they have to satisfy to the following constraints:

- No-slip and no-penetration conditions for normal velocity shall replace two rows of the matrices \mathcal{A}_j^{OS} and \mathcal{B}_j^{OS} for $j = 1, 2$.
- No-slip condition for normal vorticity shall replace one row of the matrices \mathcal{A}_j^{SQ} and \mathcal{B}_j^{SQ} for $j = 1, 2$.
- Two momentum transfer condition for normal velocity shall replace two rows of the matrices \mathcal{A}_j^{OS} and \mathcal{B}_j^{OS} for $j = 1, 2$, while the remaining shall replace two rows of the matrices \mathcal{A}^{OS} and \mathcal{B}^{OS} . Note that the choice of the two rows is arbitrary.
- One momentum transfer condition for normal vorticity shall replace one row of the matrices \mathcal{A}_j^{SQ} and \mathcal{B}_j^{SQ} for $j = 1, 2$, while the remaining shall replace one row of the matrices \mathcal{A}^{SQ} and \mathcal{B}^{SQ} . Note that the choice of the row is arbitrary.

To compute the weight matrix \mathbf{W} , we first rewrite its components as follows

$$W_{ij} = \int_{-1}^1 \tilde{\zeta}_i^H \begin{pmatrix} Mh_2 & \mathbf{0} & \mathbf{0} \\ \mathbf{0} & M & \mathbf{0} \\ \mathbf{0} & \mathbf{0} & Mh_1 \end{pmatrix} \tilde{\zeta}_j d\xi, \quad i, j = 1, \dots, K \quad (4.71)$$

where $\tilde{\zeta}_i$ and $\tilde{\zeta}_j$ are the i th and j th eigenvectors of the problem (4.40), and

$$M = \begin{pmatrix} k^2 - D^2 & 0 \\ 0 & 1 \end{pmatrix} \quad (4.72)$$

To express the eigenfunction $\tilde{\zeta}$ in terms of the Chebyshev expansion coefficients x , we first define

$$\mathbf{t} = (\boldsymbol{\theta}, \boldsymbol{\theta}, \boldsymbol{\theta}, \boldsymbol{\theta}, \boldsymbol{\theta}, \boldsymbol{\theta}), \quad \boldsymbol{\theta} = (T_0, T_1, \dots, T_N), \quad (4.73)$$

and then we write the elements of the weight matrix as follows

$$W_{ij} = \mathbf{x}_i^H \left(\int_{-1}^1 \mathbf{t}^T M \mathbf{t} d\xi \right) \mathbf{x}_j, \quad (4.74)$$

where

$$M = \begin{pmatrix} Mh_2 & \mathbf{0} & \mathbf{0} \\ \mathbf{0} & M & \mathbf{0} \\ \mathbf{0} & \mathbf{0} & Mh_1 \end{pmatrix}. \quad (4.75)$$

We refer the reader to [18, 42] for details concerning the numerical discretization of the differential operator D . Finally, in order to factorize the weight matrix as $\mathbf{W} = \mathbf{F}^H \mathbf{F}$ we perform a singular value decomposition. We have

$$\mathbf{W} = \mathbf{U} \mathbf{S} \mathbf{V}^H, \quad (4.76)$$

where \mathbf{U} and \mathbf{V} are the left and right matrix of the singular eigenvectors, respectively, and \mathbf{S} is a diagonal matrix whose elements are the singular values of matrix \mathbf{W} . Following the procedure described by Schmid and Henningson [42], we compute

$$\tilde{\mathbf{F}} = \sqrt{\mathbf{S}} \mathbf{U}^H \quad (4.77)$$

$$(4.78)$$

instead of \mathbf{F} . Note that $\tilde{\mathbf{F}}^H \tilde{\mathbf{F}} \neq \mathbf{W}$, however, $\tilde{\mathbf{F}}$ satisfies the identity (4.56), and therefore equation (4.57). Moreover, the inverse of matrix $\tilde{\mathbf{F}}$ can be computed by exploiting the singular value decomposition (4.76), as follows

$$\tilde{\mathbf{F}}^{-1} = \mathbf{U} (\sqrt{\mathbf{S}})^{-1}. \quad (4.79)$$

4.3.2 Error evaluation

The numerical evaluation of the energy growth function requires to choose intelligently both the maximum order N of Chebyshev expansions (4.61) and the number of modes K used to evaluate equation (4.57). Therefore, we define two types of error in order to control the accuracy of our results. To quantify the purity of the approximation of the eigenvalues of the problem (4.65), we first compute the quantity

$$\mathbf{e}_{N_e} = |\boldsymbol{\omega}_N - \boldsymbol{\omega}_{N+\Delta N}|, \quad (4.80)$$

where $\boldsymbol{\omega}_N$ and $\boldsymbol{\omega}_{N+\Delta N}$ are vectors containing the first N_e eigenvalues, ordered with decreasing imaginary part and obtained using as number of Chebyshev polynomials N and $N + \Delta N$, respectively. Note that the value of N_e is yet to be determined. Then, we compute

$$e_m = \|\mathbf{e}\|_\infty, \quad (4.81)$$

where m denotes the position of the maximum extracted by the norm $\|\cdot\|$. Finally, the relative error on the Chebyshev resolution is defined as

$$e_N = \frac{e_m}{|\omega_m|}, \quad (4.82)$$

where ω_m is the m th element of $\boldsymbol{\omega}_N$.

To determine the number of modes K necessary for the accurate computation of $G(t)$, we define the error,

$$e_K = \frac{|G_K^{max} - G_{K+\Delta K}^{max}|}{|G_K^{max}|}, \quad (4.83)$$

where $G_K^{max} = \max_{t \geq 0} \{G_K(t)\}$. Note that finding numerically G_K^{max} requires to choose a time interval $[0, t_1]$. In our study, we used

$$t_1 = 2t^*, \quad (4.84)$$

where $t^* = 0.076\text{Re}$ is the instant at which maximum possible amplification over the wavenumber space, $\max_{\alpha, \beta} G^{max}$, occurs in Poiseuille flow [52].

4.3.3 Structure of the program

Our aim is to study the maximum of the transient growth function in the parameter space defined by

$$\text{Re}, \alpha, \beta, h_p, \sigma, \epsilon, \tau,$$

varying simultaneously. Each parameter may influence both the number of Chebyshev polynomials N needed to solve accurately the spectrum and the number of modes K to be used to compute the energy growth. To ensure a chosen accuracy for each case, we implement an adaptive algorithm that selects autonomously the correct values of N and K . The algorithm is initialized with a reasonable value of Chebyshev polynomials N_{min} and a number of modes K_{min} . The program starts computing the eigenvalues for a given set of the parameters using a number N of Chebyshev polynomials. Then, a cycle that determines the number of modes to compute precisely $G(t)$ begins. In this cycle the program computes the maximum value of the energy growth using both K and $K + \Delta K$ modes, and then evaluates the error e_K expressed by equation (4.83). If the error e_K is greater than the tolerance ϵ_K , the program increase of ΔK the number of modes used to compute the transient growth. Once the appropriate number of modes has been found, the program verify the accuracy of the eigenvalues corresponding to the used modes. To this end, the program computes the spectrum using a higher number of Chebyshev polynomials $N + \Delta N$, and then, evaluates the error e_N defined in (4.82), using $N_e = K$. If ϵ_N is less than the tolerance ϵ_N , the program saves the maximum of the energy growth. Otherwise, the cycle on K starts again using the modes obtained with the Chebyshev expansion of order $N + \Delta N$. A flowchart describing the algorithm is shown in figure 4.1.

4.3.4 Validation

We ensure the correctness of the eigenvalues by comparing the less stable (unstable) eigenvalue with the ones reported by Tilton [49] and Tilton and Cortezzi

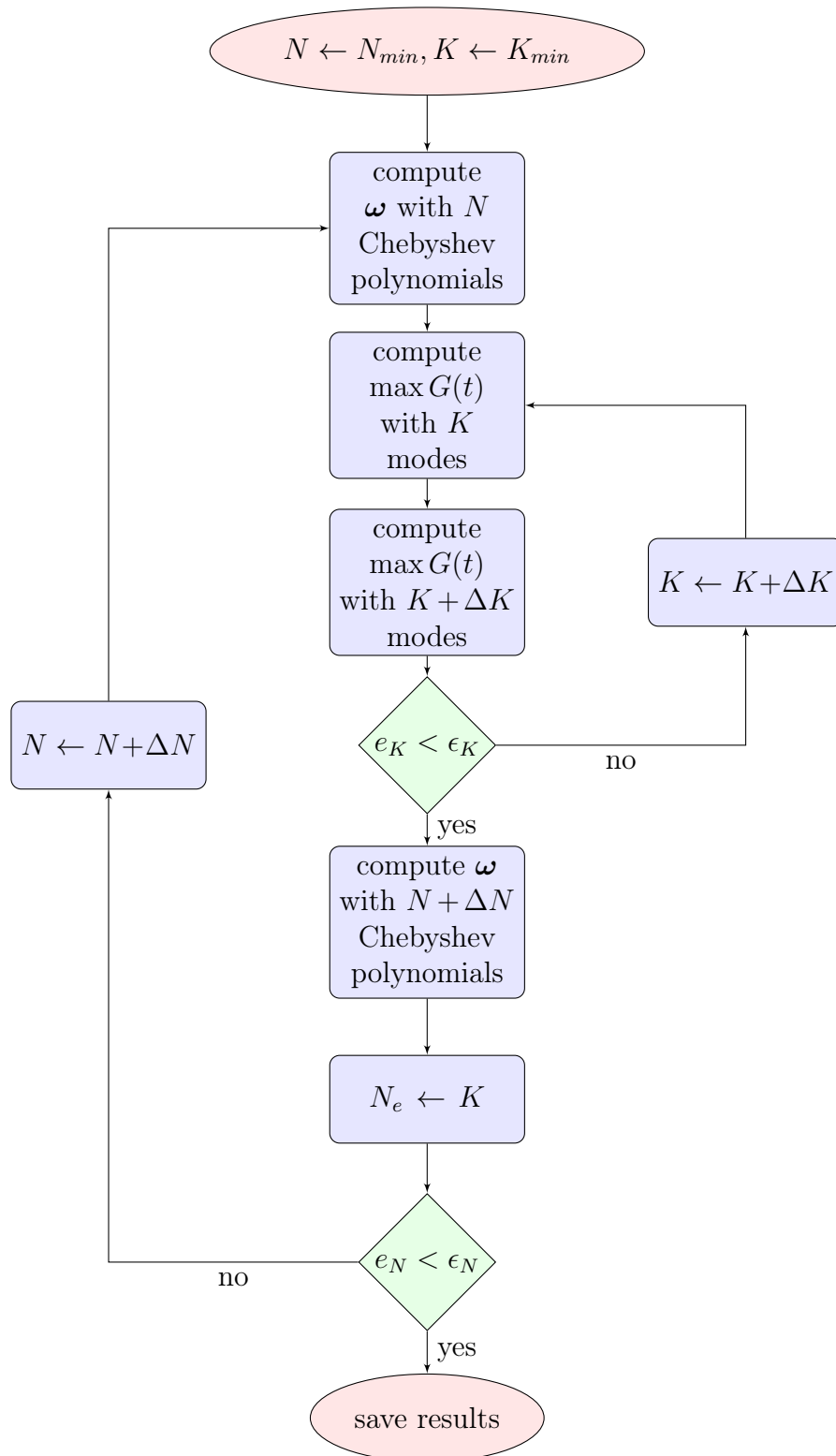


Figure 4.1: Flowchart of the algorithm implemented in the program for the non-modal stability study.

[51] for different cases. Secondly, we ensure that the maximum value of the energy growth function is computed correctly. In this case we exploit the fact that eigenvalues converge to the ones of Poiseuille flow when the wall permeability approximates zero [51], and therefore, the transient energy growth becomes identical to Poiseuille flow one. Figure 4.2(a) represents the function $G(t)$ for channel flow over porous walls (red solid line) which converges to the transient growth of Poiseuille flow (black dash-dotted line), as permeability tends to zero. Figure 4.2(b) represents the corresponding values of

$$\delta_G = \frac{G_{max}(t) - G_{max}^P(t)}{G_{max}^P(t)}, \quad (4.85)$$

where $G_{max}^P(t)$ is the the maximum value of the transient growth for Poiseuille flow. Note that δ_G tends to zero as σ approximates a impermeable wall.

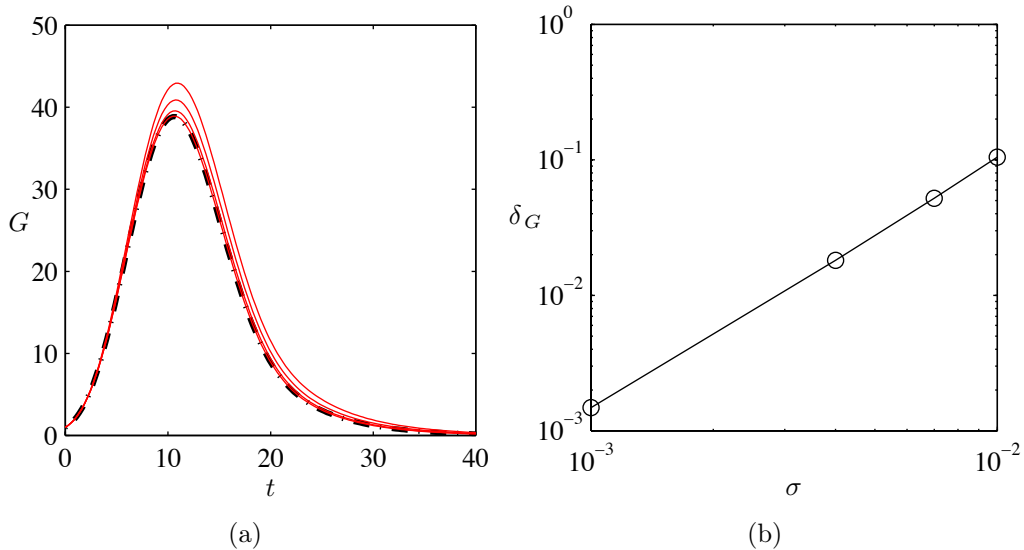


Figure 4.2: For parameters $Re = 500$, $\alpha = 1$, $\beta = 1.5$, $h = 1$, $\varepsilon = 0.6$ and $\tau = 0$, (a) A comparison between the transient energy growth for channel flow over porous walls with $\sigma_1 = \sigma_2 = 0.02, 0.014, 0.008, 0.002$ (red solid line) and of Poiseuille flow at the same Reynolds number (black dashed line). (b) Corresponding values of δ_G .

Chapter 5

Results

In this study we analyze the non-modal stability of laminar and fully-developed flows in channels with two identical porous walls. We solve numerically the eigenvalue problem (4.40) arising from the modal Navier-Stokes equations (4.27) and (4.28) that govern the flow in the fluid region, and from the modal Volume-Averaged Navier-Stokes equations (4.29) and (4.30) that govern the flow in the porous regions, and then, we compute the maximum value of the transient growth function (4.57). Since the porous layers are identical, we drop the subscript $j = 1, 2$ and use h_p , σ , ε and τ to denote the half height, permeability, porosity and momentum transfer coefficient, respectively.

In order to study the non-modal stability of our system, we consider the discrete parameter space

$$\begin{aligned} \text{Re} &\in \{500, 750, 1000\}, \\ \alpha &\in \{0, 0.1, \dots, 1.9, 2\}, \\ \beta &\in \{0, 0.1, \dots, 3.9, 4\}, \\ h_p &\in \{1\}, \\ \sigma &\in \{0.002, 0.0065, 0.011, 0.0155, 0.02\}, \\ \varepsilon &\in \{0.3, 0.4, 0.5, 0.6, 0.7, 0.8\}, \\ \tau &\in \{-1, -0.75, \dots, 0.75, 1\}. \end{aligned}$$

We have chosen the bounds for wavenumbers α and β because plane Poiseuille flow shows in such region most of its interesting non-modal behavior. We have chosen the higher possible values of permeability σ that allow us to consider the inertial effects negligible in most of the cases. The coefficient τ is not precisely physical meaningful, so we have considered it as an error bar. We have chosen to vary τ between -1 and 1 according to Ochoa-Tapia and Whitaker, who theoretically estimated that $|\tau|$ is of the order of one [29]. We have chosen the values of the porosity to study its impact on the non-modal and linear stability, since Tilton and Cortelezzi reported results for $\varepsilon = 0.6$ [51]. We have chosen the value

of the height of the porous layer $h_p = 1$, because Tilton and Cortelezzi used this value in many of the cases they reported [51]. Finally, we have chosen Reynolds numbers below the critical value of Poiseuille flow.

We perform our computations using the algorithm described in subsection 4.3.3, where the minimum number of Chebyshev polynomials is $N_{min} = 80$, and the minimum number of modes to compute $G(t)$ is $K_{min} = 50$. In order to evaluate the error e_N defined in (4.82) we use a reference solution computed with $N + \Delta N$ Chebyshev polynomials, with $\Delta N = 10$, while to compute the error e_K defined in (4.83), we use a transient growth function computed with $K + \Delta K$ modes, with $K = 20$. We chose error tolerances $\epsilon_N = 10^{-5}$ and $\epsilon_K = 10^{-2}$ as a trade-off between numerical accuracy and computational cost.

Our parameter space is six-dimensional and it has been discretized on a grid of 697410 points. Therefore, to show how the various parameters influence transient growth with respect to the plane Poiseuille flow, we have to draw the contour levels of the function $G^{max}(\text{Re}, \alpha, \beta, h_p, \sigma, \varepsilon, \tau)$ by fixing at least four parameters.

In this thesis we follow the standard practice to plot the contour levels of $G^{max}(\alpha, \beta)$, to compare our results with Poiseuille flow. We start focusing on a representative point of the parameter space. We choose $\text{Re} = 500$, $h_p = 1$, $\sigma = 0.0155$, $\varepsilon = 0.4$, $\tau = 0$, because it allow us for significant comparisons when we vary the parameters. Then, we analyze the transient growth and the optimal initial condition in the point of the wavespace where the effects of the permeable walls are maximum. Subsequently, we discuss the effects that permeability, interface momentum transfer coefficient and porosity have on G^{max} and on the optimal initial condition, with respect to the case above-mentioned.

5.1 A reference case

5.1.1 Maximum amplification in wavespace

We start analyzing the maximum value of the transient energy growth for the representative point of the parameter space

$$\text{Re} = 500, h_p = 1, \sigma = 0.0155, \varepsilon = 0.4, \tau = 0$$

as a function of wavenumbers α and β . Figure 5.1(a) illustrates the contour lines of G^{max} in red solid line, and of G_P^{max} for Poiseuille flow in black dotted line. Note that contour levels are the same for the two cases. We observe that permeable walls affect the maximum of the transient growth altering the shape of the contour lines. In particular, the effects of permeability diminish for values of the wavenumber α approximating zero and for the wavenumber β greater than ≈ 2 . The maximum value of G_{max} over the considered wavespace nearl does not change with respect to Poiseuille flow. In order to quantify the differences of G^{max} induced by the wall permeability, we analyze over the wavespace the relative

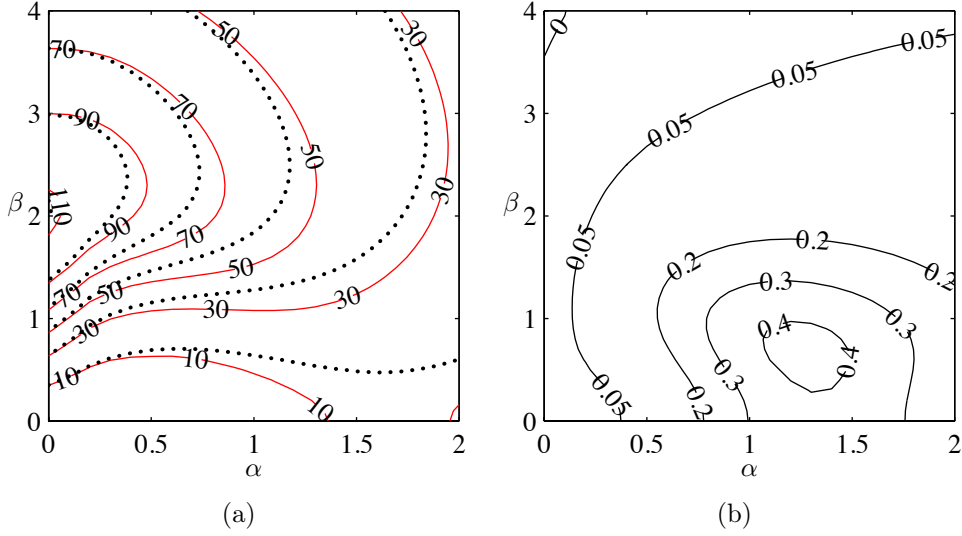


Figure 5.1: For parameters $Re = 500$, $h_p = 1$, $\sigma = 0.0155$, $\varepsilon = 0.4$, $\tau = 0$, (a) contour levels of G^{max} for the flow over porous walls (red solid line) and Poiseuille flow at the same Reynolds number (black dotted line) and (b), corresponding contour levels of δG .

difference δG defined in equation (4.85). Figure 5.1(b) shows the contour lines of δG . For $\alpha \gtrsim 0.5$ and $\beta \lesssim 2.5$, porous walls cause a significant relative increment (up to $\approx 40\%$) of G_{max} at $\alpha = 1.3$ and $\beta = 0.7$, while for α approximating zero δG is very small. For $\alpha \approx 0$ and $\beta \approx 4$, there is a small region in which permeability decreases G^{max} .

5.1.2 Transient growth function

In this section, we focus on the pair of wavenumbers for which δG is maximum, to investigate how permeable walls can amplify G^{max} of $\approx 40\%$ with respect to the Poiseuille flow. To this end, we consider the spectrum of the eigenvalues, reported in figure 5.2, where red dots are the eigenvalues of the flow over porous walls, and black circles are the ones for Poiseuille flow. In the upper part of the spectrum, figure 5.2(a), we recognize the wall and center modes, that correspond to the left and right branches of the Y. Porous walls cause the eigenvalues to move on the complex plane and, in particular, we see the less stable wall modes move towards the positive imaginary semi-plane, as showed by Tilton and Cortelezzi [51]. The lower part of the spectrum, figure 5.2(b), is characterized by the presence of the couple of eigenvalues B, and a series of aligned eigenvalues C. Modes B are called coupling modes, and represent the the momentum transfer conditions at the interface between the porous layers and the fluid region. Modes C represent the eigenvalues associated to the Volume-Averaged equations, which govern the flow in the porous layers. Figure 5.3 plots the growth function that achieves the

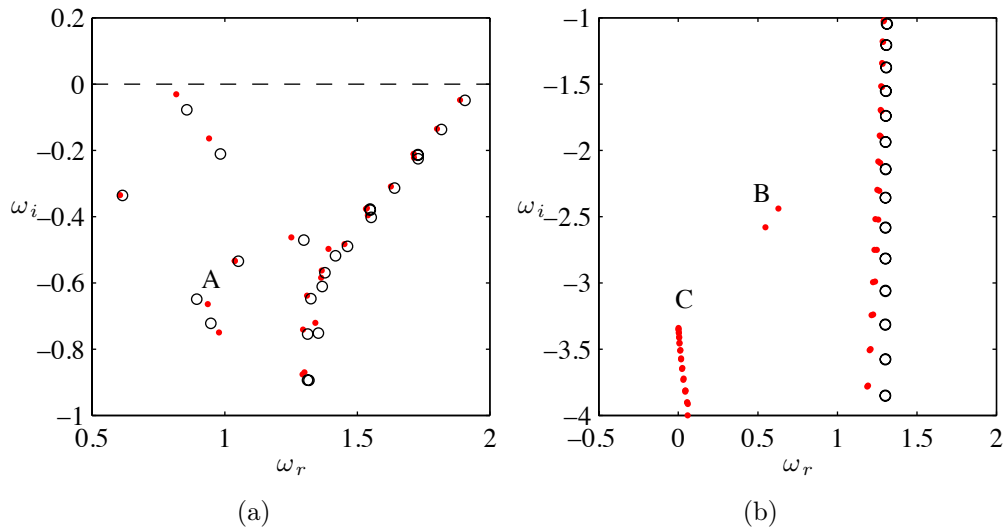


Figure 5.2: Spectrum for porous flow $\text{Re} = 500$, $\alpha = 1.3$, $\beta = 0.7$, $h_p = 1$, $\sigma = 0.0155$, $\varepsilon = 0.4$, $\tau = 0$ (red dots), and for Poiseuille flow at the same Reynolds number (black circles). (a) Upper part of the spectrum, with A, the 22nd mode. (b) Lower part of the spectrum, with coupling modes B and porous modes C.

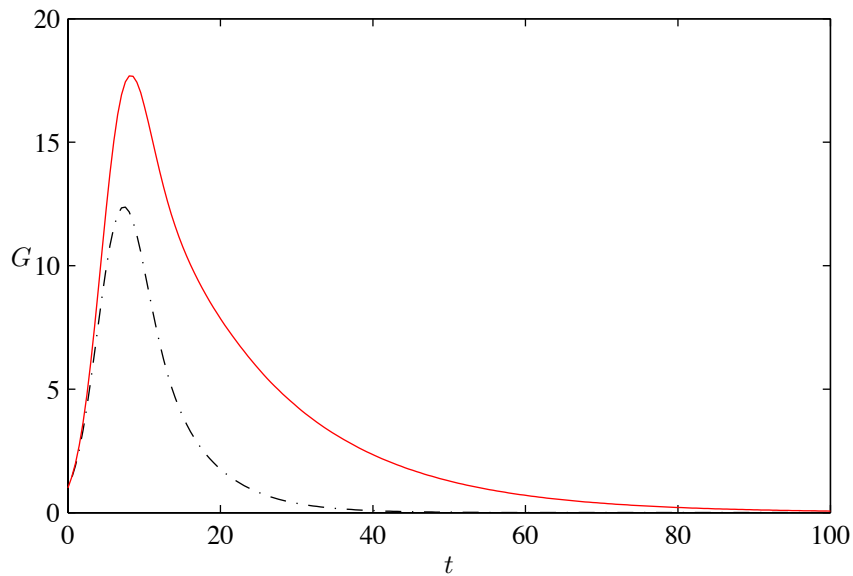


Figure 5.3: A comparison between the the growth function $G_K(t)$ for $\text{Re} = 500$, $\alpha = 1.3$, $\beta = 0.7$, $h_p = 1$, $\sigma = 0.0155$, $\varepsilon = 0.4$, $\tau = 0$ (red solid line) with the one of Poiseuille flow at the same Reynolds number (black dash-dotted line).

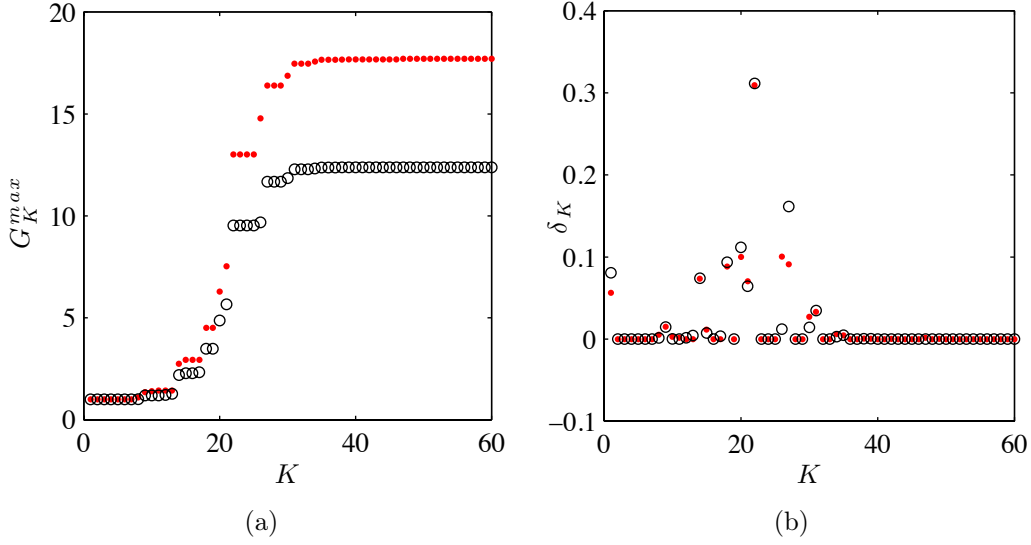


Figure 5.4: For parameters $\text{Re} = 500$, $\alpha = 1.3$, $\beta = 0.7$, $h = 1$, $\sigma = 0.0155$, $\varepsilon = 0.4$, $\tau = 0$, (a) successive approximations of G^{max} obtained with increasing dimension K of the reduced base, comparison between flow over porous walls (red points), and Poiseuille flow at the same Reynolds number (black circles). (b) Corresponding values of δ_K .

maximum relative increment δG in red solid line, compared with the Poiseuille case, plotted in black dash-dotted line. We observe that in both cases there is a steep slope before the maximum value and then a decay as $t \rightarrow \infty$. The maximum is reached almost at the same instant, while the decay is much slower in the porous case.

It is interesting to consider how G^{max} changes when we increase the number K of eigenvectors used to compute $G_K(t)$ with the formula (4.57). Figure 5.4(a) shows $G_K^{max} = G^{max}(K)$ for the flow over porous walls (red dots) and for Poiseuille flow (black circles). In both cases, we need to use about 40 eigenvectors to compute numerically and precisely the maximum energy growth. Note that when we include modes B ($K = 44, 47$) and modes C ($K > 54$), G_K^{max} nearly does not change. Therefore, in this case we are able to describe correctly the transient growth for a flow in a channel with porous walls by including only the modes associated to the homogeneous fluid region. To investigate which values of K produce the most significant contributions, we define

$$\delta_K = \frac{G_K^{max} - G_{K-1}^{max}}{G^{max}}, \quad (5.1)$$

where the normalizing factor G^{max} is the G_K^{max} which satisfies to the constraint $e_K < \epsilon_K$. Figure 5.4(b) presents δ_K . We observe that in both cases, most of the significant increments of δ_K occur when K is large enough to include the modes near the intersection of the branches of the Y, coherently to the results

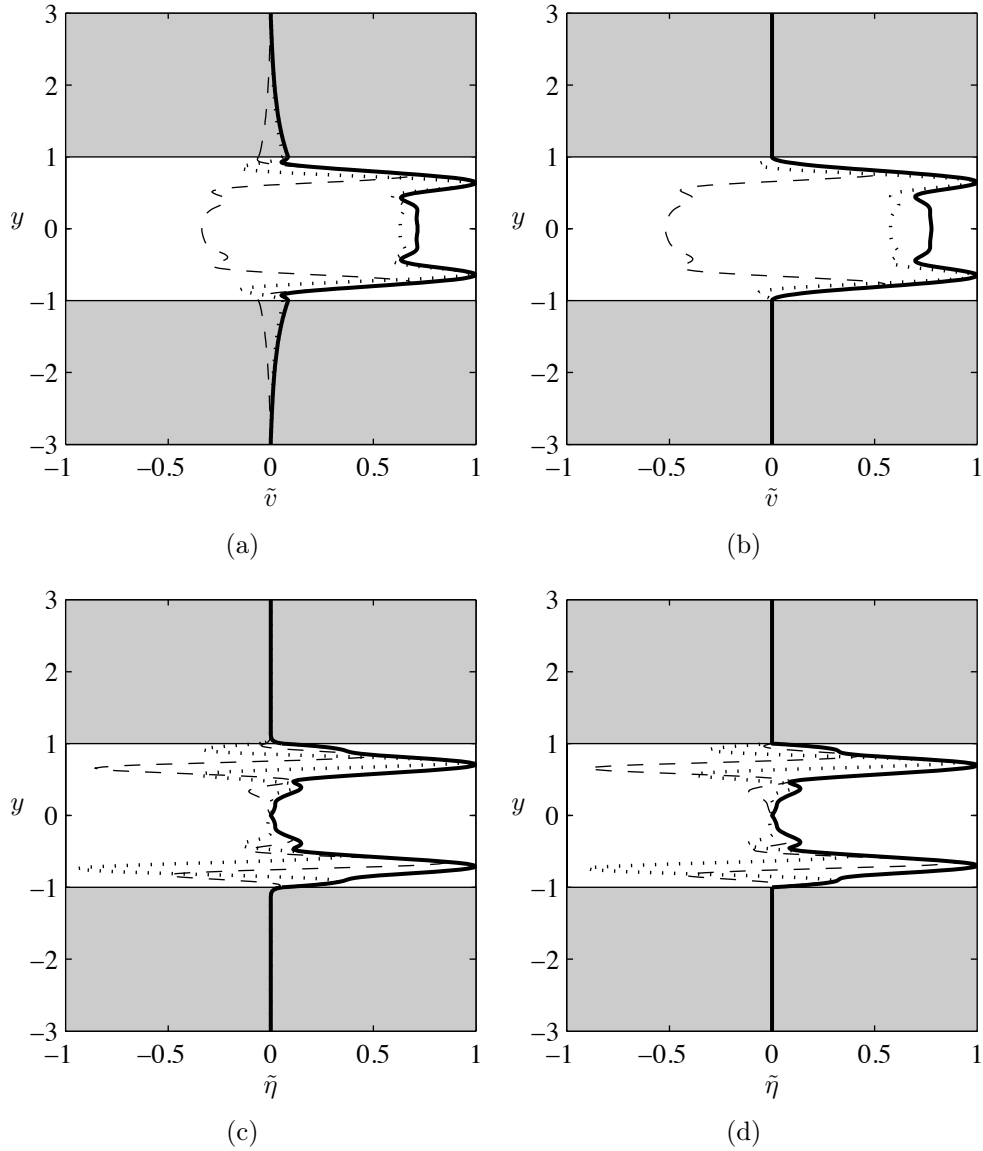


Figure 5.5: Eigenfunctions of mode A, modulus (solid line), real part(dotted line) and imaginary part(dashed line). A comparison between the flow over porous walls, for $\text{Re} = 500$, $\alpha = 1.3$, $\beta = 0.7$, $h = 1$, $\sigma = 0.0155$, $\varepsilon = 0.4$, $\tau = 0$ (left column), and Poiseuille flow for at the same Reynolds number (right column).

of Reddy and Henningson [37]. We have the maximum relative increment when we include the 22nd mode, which is the same eigenvector for both porous and channel flows, and it is associated to the eigenvalue denoted by the letter A in figure 5.2(a). Figure 5.5 illustrates the eigenfunction of the mode A for the normal velocity (top) and normal vorticity (bottom), both for the flow over porous walls (left column) and Poiseuille flow (right column). Note that A is a wall mode

with symmetric normal velocity and anti-symmetric normal vorticity. The wall-normal velocity perturbation penetrates deeply into the porous layer, while the wall-normal vorticity perturbation does not. In particular, we observe that the velocity profile of $|\tilde{v}|$ presents an oscillation on the fluid side of the interface. The effect of the permeability is lost around the centerline of the channel, where the velocity profile remains nearly unchanged.

5.1.3 Optimal initial condition

The transient growth, $G(t)$, represents the maximum energy amplification which can occur at each instant t . To investigate how the presence of the porous walls can amplify the transient growth with respect to the channel flow, we construct the initial condition $\hat{\zeta}_{0,opt}$ that produces the maximum energy amplification. To this end, we first compute the matrix

$$\mathbf{Q}_{max} = \tilde{\mathbf{F}} \exp(-i\mathbf{\Omega}t_{max})\tilde{\mathbf{F}}^{-1}, \quad (5.2)$$

where $\mathbf{\Omega}$ and $\tilde{\mathbf{F}}$ have been defined in subsections 4.2.2 and 4.3.1, respectively, and t_{max} is the instant at which maximum amplification, G^{max} , occurs; then we perform the singular value decomposition

$$\mathbf{Q}_{max} = \bar{\mathbf{U}}\bar{\mathbf{S}}\bar{\mathbf{V}}^H. \quad (5.3)$$

It can be shown [42], that the optimal initial condition is

$$\hat{\zeta}_{0,opt} = \tilde{\mathbf{F}}^{-1}\mathbf{u}, \quad (5.4)$$

where \mathbf{u} is the first column of the matrix $\bar{\mathbf{U}}$.

We now construct the optimal initial condition for the wavenumbers $\alpha = 1.3$, $\beta = 0.7$, which generates the maximum increase of G^{max} , with respect to the Poiseuille flow. Figure 5.6(a) and 5.6(c) show the optimal normal velocity and normal vorticity perturbations for the flow over porous walls, while figure 5.6(b) and 5.6(d) show the corresponding perturbations for Poiseuille flow. The normal velocity profiles are symmetric, and they are similar in the fluid region around the centerline, while they become different approaching the interface. In the Poiseuille flow, the normal velocity is zero at the interface because of the no-penetration condition (the porous layer can be seen as a porous medium with permeability equal to zero), while in the flow with porous walls there is significant flow across the interface. Moreover, the optimal normal velocity perturbation extends into the porous layers, deeply than the theoretical thickness of the Brinkmann layer. On the contrary, the optimal normal vorticity profiles are antisymmetric and very similar over the entire fluid region, in both flows. Interestingly, the optimal normal vorticity perturbation does not penetrate into the porous layers below a very thin layer at the interface.

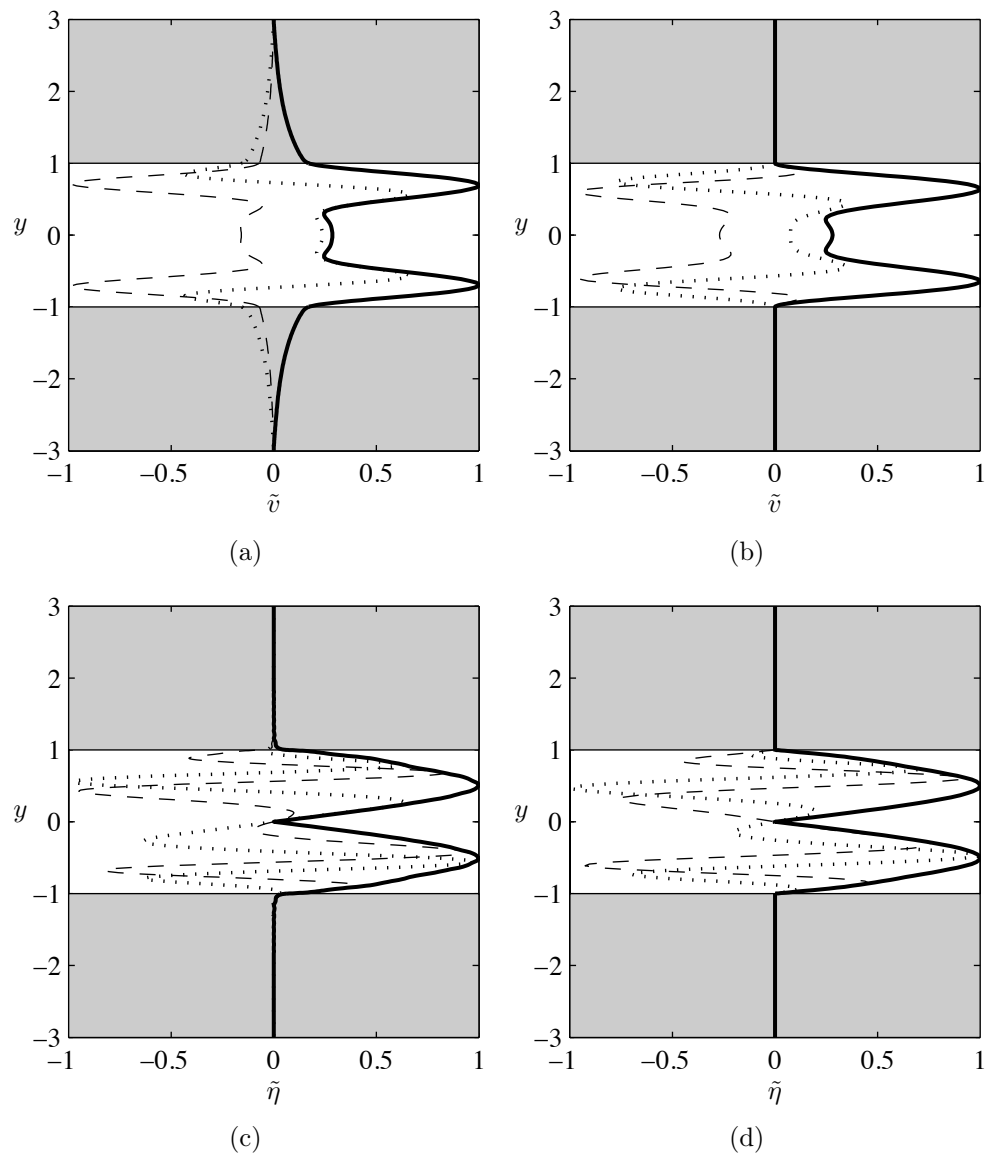


Figure 5.6: Optimal initial condition, modulus (solid line), real part(dotted line) and imaginary part(dashed line). A comparison between flow over porous walls, for $\text{Re} = 500$, $\alpha = 1.3$, $\beta = 0.7$, $h = 1$, $\sigma = 0.0155$, $\varepsilon = 0.4$, $\tau = 0$ (left column), and Poiseuille flow at the same Reynolds number (right column).

5.2 Effects of permeability

We investigate the effects of permeability on maximum value of transient growth G^{max} for parameters $Re = 500$, $h_p = 1$, $\varepsilon = 0.4$, $\tau = 0$. We start by considering the contours lines of G^{max} and δG for $\sigma = 0.0065$, illustrated in figure 5.7(a) and 5.7(b), respectively. With respect to the case with $\sigma = 0.0155$ discussed in subsection 5.1.1, we observe that the effects on the maximum value of energy growth reduced considerably, and G^{max} becomes closer to the values of Poiseuille flow. Maximum of δG reduces from $\approx 42\%$ to $\approx 7\%$ and it is located at $\alpha = 1.3$ and $\beta = 0.7$. Moreover, we observe that the region in which δG is negative has become wider. However, maximum reduction is small ($\approx 0.004\%$), so permeability tends to increase dominantly the maximum transient growth in the considered wavespace. Figures 5.7(c) and 5.7(d) show the effect of permeability when it is increased up to $\sigma = 0.02$. Note that the flow in this case is linearly unstable for all the points of the wavespace in the grey shaded area and therefore, in these points $G^{max} \rightarrow \infty$. Note also that plane Poiseuille flow becomes linearly unstable at $Re \approx 3848$. Secondly, the relative local amplification δG increased significantly, reaching ≈ 0.8 near the boundary of the unstable region. Maximum of G^{max} over the wavespace is located at $\alpha = 0$ and $\beta = 2$ and it is only $\approx 2\%$ greater than channel maximum. Moreover, we note that in the considered wavespace, the region characterized by $\delta G < 0$ is not present. Note that the bubble on contour level $\delta G = 0.3$ is caused by a numerical error produced when the program tries to find the maximum of the transient growth. In particular, the maximum search algorithm may not converge to the correct value when function $G(t)$ admits two local maximum very close to each other, instead of a single absolute maximum or well-separated peaks.

To investigate in detail how permeability can produce such a relevant increment in G^{max} , we consider the reference case in the point $\alpha = 1.3$ and $\beta = 0.7$ that we discussed in subsection 5.1.2. Figure 5.8(a) shows the transient growth for $\sigma = 0.0065$ (dotted line), $\sigma = 0.0155$ (solid line) and $\sigma = 0.02$ (dash-dotted line). High values of permeability generate both a relevant amplification of G^{max} and a longer decay, while t_{max} experiences an increase of the order of 10%. Figure 5.8(b) illustrates the corresponding modulus of the optimal initial normal velocity. We observe that an increase in the value of the permeability produces higher normal velocity at the interface and a deeper penetration of the perturbation into the porous layer. Also, note that the optimal perturbation profile at the interface experiences a smoother change in the derivative with respect to y for high values of the wall permeability.

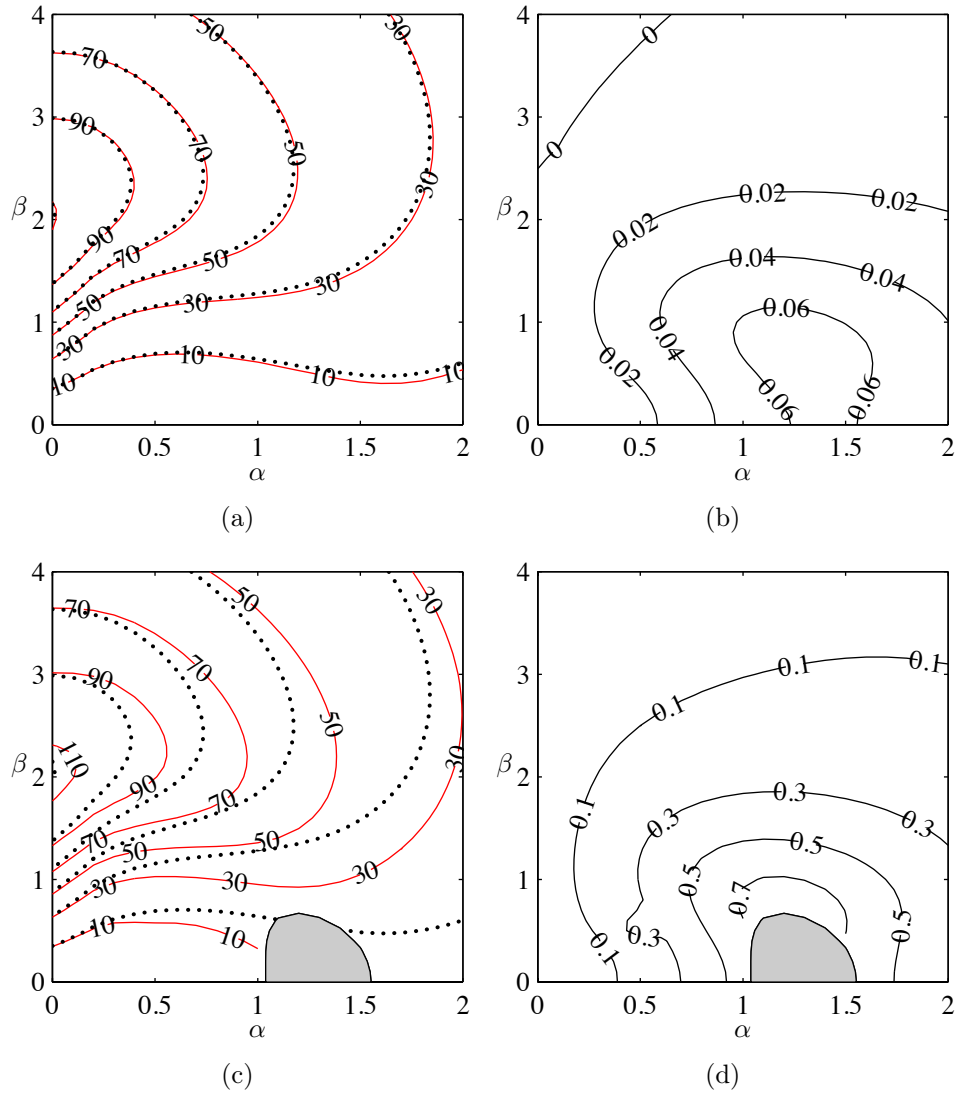


Figure 5.7: For parameters $Re = 500$, $h = 1$, $\varepsilon = 0.4$, $\tau = 0$, (a) and (c) contours of G^{max} , with $\sigma = 0.0065, 0.02$, respectively. (b) and (d) contour levels of δG , with $\sigma = 0.0065, 0.02$, respectively. Red solid line denotes flow over porous walls, while black dash dotted line denotes Poiseuille flow at the same Reynolds number. The gray area marks the linearly unstable region.

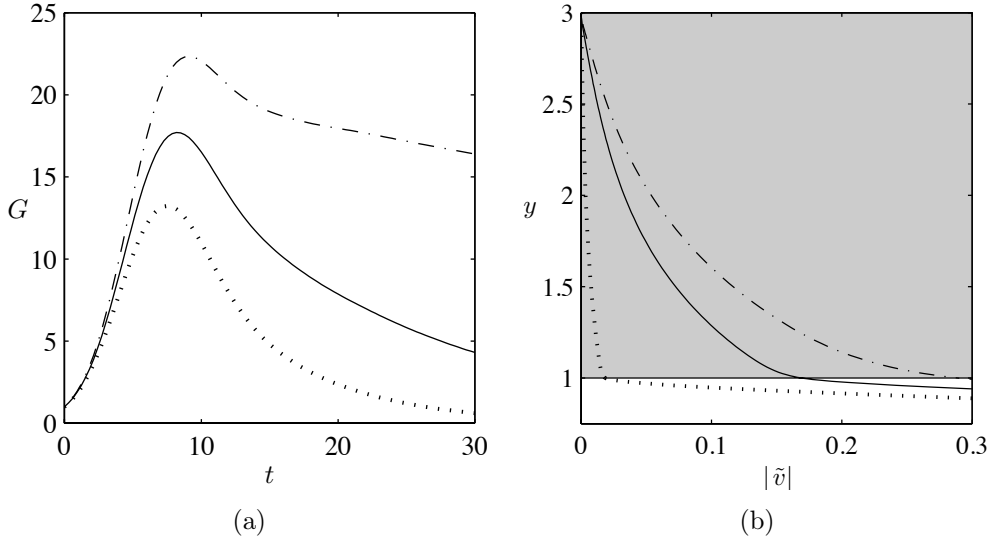


Figure 5.8: For parameters $\text{Re} = 500$, $\alpha = 1.3$, $\beta = 0.7$, $h_p = 1$, $\varepsilon = 0.4$, $\tau = 0$, (a) the effects of permeability on the transient growth function, and (b), the effects of permeability on the modulus of the optimal initial normal velocity. Permeability are $\sigma = 0.0065$ (dotted line), $\sigma = 0.0155$ (solid line) and $\sigma = 0.02$ (dash-dotted line).

5.3 Effects of the momentum transfer coefficient

Figure 5.9 shows the effects of τ on G^{max} , for a porous channel with $h_p = 1$, $\varepsilon = 0.4$, and (a) $\sigma = 0.0155$, $\text{Re} = 500$, (b) $\sigma = 0.02$, $\text{Re} = 500$, (c) $\sigma = 0.0155$, $\text{Re} = 750$ and (d) $\sigma = 0.02$, $\text{Re} = 750$. We report the results obtained using $\tau = 0$, indicated by the solid line, $\tau = 1$, indicated by the dashed line and $\tau = -1$ indicated by the dotted line. When we lower the interface coefficient to $\tau = -1$, the maximum value G^{max} nearly does not change, while when we raise the coefficient up to $\tau = 1$ we observe that in most of the wavenumber, locally G^{max} diminishes with respect to the case with $\tau = 0$. The effect of the interface coefficient tends to increase as the streamwise wavenumber does. Also, by increasing the Reynolds number and the permeability, we note that τ has a slightly stronger influence on G^{max} over the considered wavenumber. Overall, τ has a significant impact on linear stability. More precisely, the shaded areas denote linearly unstable regions, for $\tau = -1$ (darkest gray), 0, 1 (lightest gray). Note how $\tau = 1$ has a stabilizing effect, while the region for $\tau = -1$ is nearly coincident with the one for $\tau = 0$.

We study the effects of the momentum transfer coefficient by considering the reference case in the point $\alpha = 1.3$ and $\beta = 0.7$ that we discussed in subsection 5.1.2. Figure 5.10(a) shows the transient growth for $\tau = -1$ (dotted line), $\tau = 0$ (solid line) and $\tau = 1$ (dashed line). First, we note that maximum amplification of the perturbation energy remains nearly unchanged, as we expect by observing

figure 5.9(a). However, $G(t)$ evaluated with $\tau = 1$ decays faster as time increases. Figure 5.10(b) illustrates the modulus of the initial optimal normal velocity for the cases above discussed. Differently from the permeability, the momentum transfer coefficient nearly does not change the normal velocity at the interface, neither how deeply the perturbation penetrates into the porous layer. However, in the case with $\tau = 1$, the optimal normal velocity in the porous layer is slightly smaller than in the other cases.

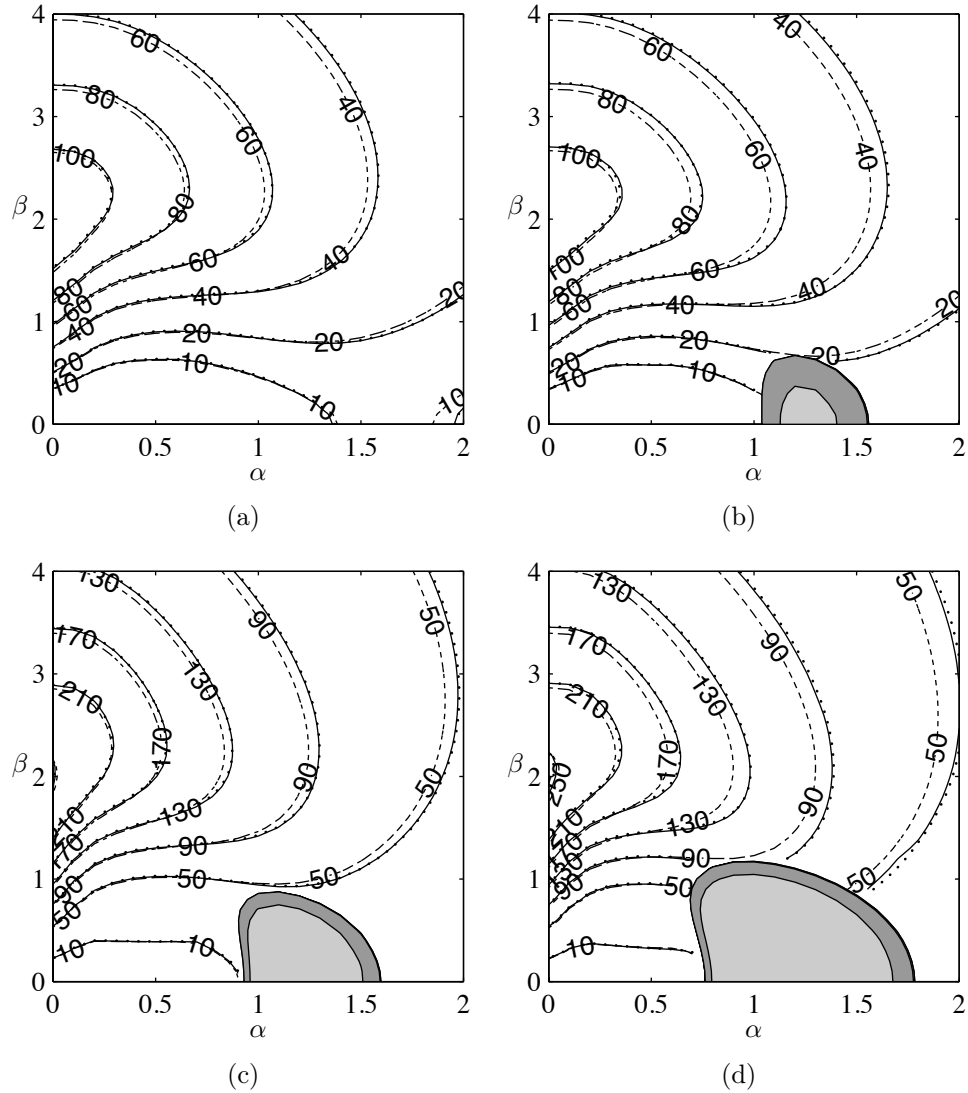


Figure 5.9: For parameters $h_p = 1$, $\varepsilon = 0.4$, the contour levels of G^{\max} using $\tau = 0$ (solid line), $\tau = 1$ (dashed line) and $\tau = -1$ (dotted line). Shaded areas are linearly unstable regions for $\tau = -1$ (darkest gray), 0, 1 (lightest gray). Permeability and Reynolds number are: (a) $\sigma = 0.0155$, $Re = 500$; (b) $\sigma = 0.0155$, $Re = 750$; (c) $\sigma = 0.02$, $Re = 500$; (d) $\sigma = 0.02$, $Re = 750$.

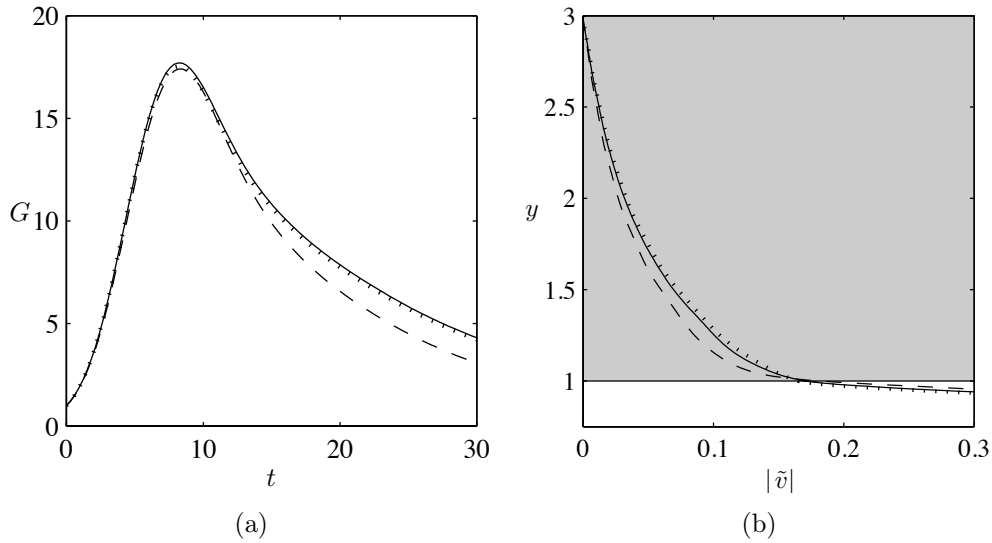


Figure 5.10: For parameters $Re = 500$, $\alpha = 1.3$, $\beta = 0.7$, $h_p = 1$, $\sigma = 0.0155$, $\varepsilon = 0.4$, (a) the effects of τ on the transient growth function, and (b), the effects of τ on the magnitude of the optimal initial normal velocity. The values of the interface coefficient are $\tau = -1$ (dotted line), $\tau = 0$ (solid line) and $\tau = 1$ (dashed line).

5.4 Effects of porosity

Figure 5.11 shows the effects of the porosity on G^{max} , for a porous channel with $h_p = 1$, $\tau = 0$, and (a) $\sigma = 0.0155$, $Re = 500$, (b) $\sigma = 0.02$, $Re = 500$, (c) $\sigma = 0.0155$, $Re = 750$ and (d) $\sigma = 0.02$, $Re = 750$. We report the results obtained using $\varepsilon = 0.3$, indicated by the dotted line, $\varepsilon = 0.4$, indicated by the solid line and $\varepsilon = 0.8$, indicated by the dashed line. We observe that varying the porosity produces changes of the maximum transient growth smaller than the ones associated to the interface coefficient, which we discussed in section 5.3. The effects of the porosity are negligible in all the reported cases, with $\alpha < 0.5$, while in the rest of the wavenumber space there are different behaviors depending on the wavenumbers α and β . In particular, there are regions in which a high value of ε produces a higher value of G^{max} , with respect to $\varepsilon = 0.4$, and vice versa. As we noted for the coefficient τ , higher values of the Reynolds number and permeability amplify the effects of varying ε . Varying the porosity affects the linear stability of the problem. More precisely, the shaded areas denote linearly unstable regions, for $\varepsilon = 0.3$ (lightest gray), 0.4, 0.8 (darkest gray). The linearly unstable region becomes wider as the porosity is increased. It is interesting to note that varying ε from 0.4 to 0.3 produces effects comparable to the ones obtained varying ε from 0.4 to 0.8.

We consider the reference case discussed in subsection 5.1.2 to investigate in detail the effect of the porosity on the transient growth function. Figure

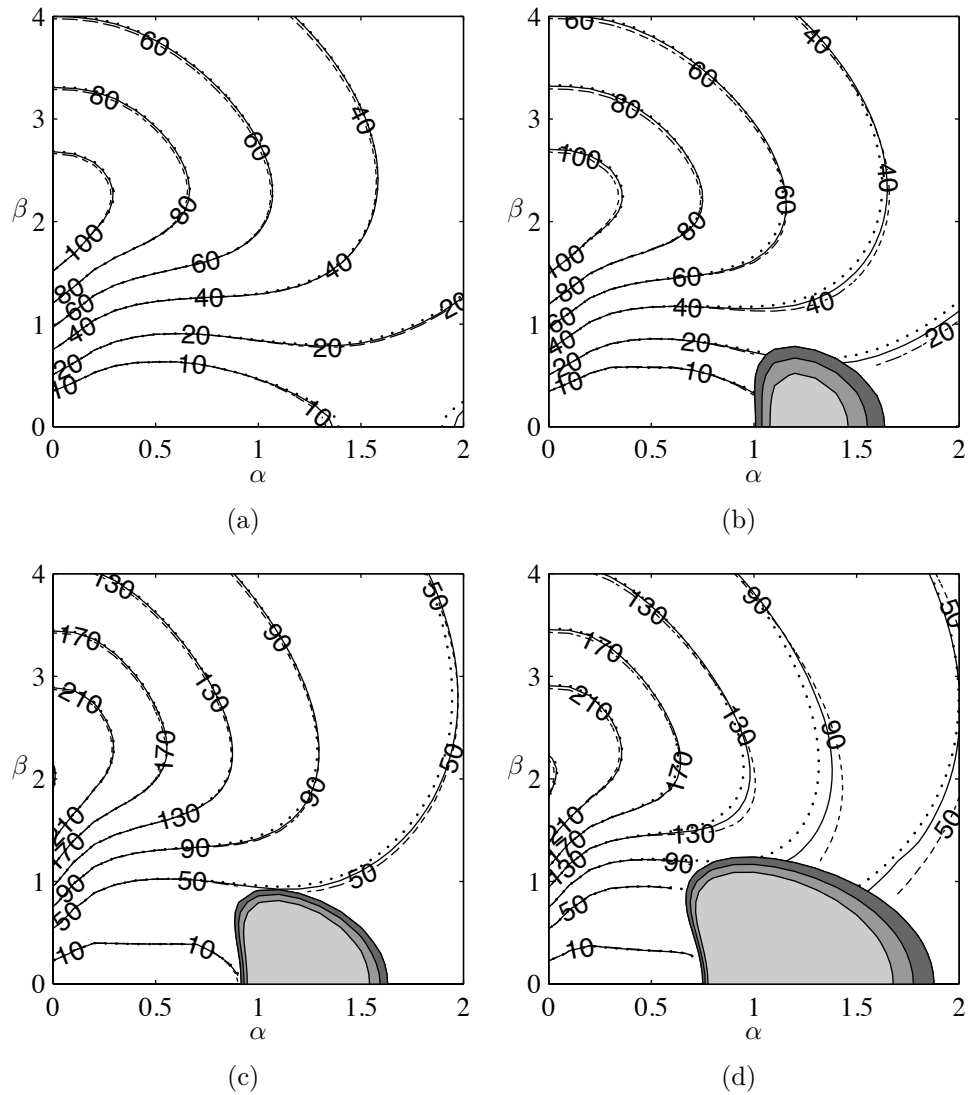


Figure 5.11: For parameters $h_p = 1$, $\tau = 0$, the contour levels of G^{max} using $\epsilon = 0.4$ (solid line), $\epsilon = 0.8$ (dashed line) and $\epsilon = 0.3$ (dotted line). Shaded areas are linearly unstable regions for $\epsilon = 0.3$ (lightest gray), $0.4, 0.8$ (darkest gray). Permeability and Reynolds number are: (a) $\sigma = 0.0155$, $Re = 500$; (b) $\sigma = 0.0155$, $Re = 750$; (c) $\sigma = 0.02$, $Re = 500$; (d) $\sigma = 0.02$, $Re = 750$.

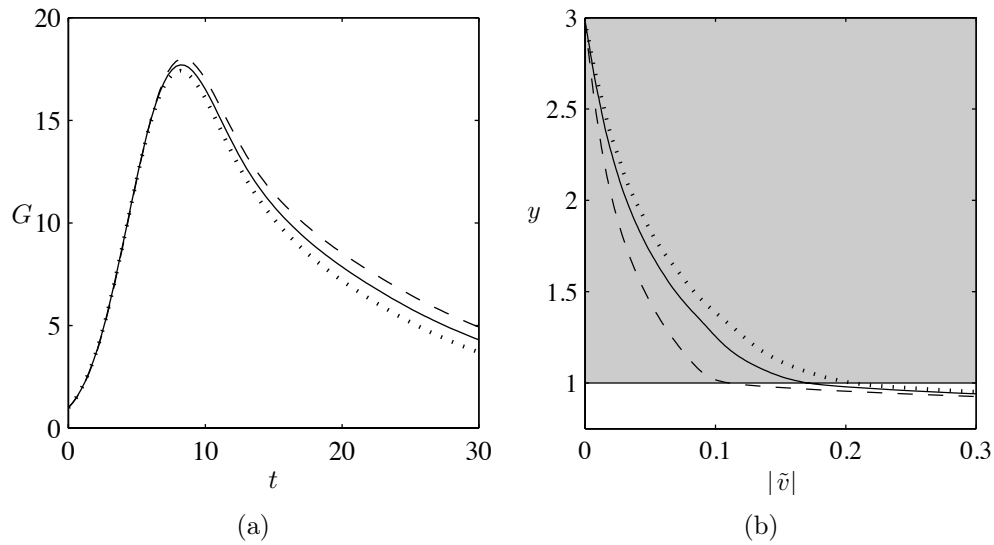


Figure 5.12: For parameters $\text{Re} = 500$, $\alpha = 1.3$, $\beta = 0.7$, $h_p = 1$, $\sigma = 0.0155$, $\tau = 0$, (a) the effects of the porosity on the transient growth function, and (b), the effects of the porosity on the magnitude of the optimal initial normal velocity. The values of the porosity are $\varepsilon = 0.3$ (dotted line), $\varepsilon = 0.4$ (solid line) and $\varepsilon = 0.8$ (dashed line).

5.12(a) illustrates $G(t)$ for $\varepsilon = 0.3$ (dotted line), $\varepsilon = 0.4$ (solid line) and $\varepsilon = 0.8$ (dashed line). We observe that $G(t)$ nearly does not change until the maximum, and after that, introduces small delays in the decay. Figure 5.12(b) shows the corresponding modulus of the initial optimal normal velocity. We observe that the optimal perturbation penetrates deeper into the porous layer as the porosity is increased.

Chapter 6

Conclusions and future work

In this thesis we reported selected results from a large parametric study on the non-modal stability of a laminar channel flow over porous walls, in comparison to the plane Poiseuille flow. We modeled the flow in the fluid region using the Navier-Stokes equations, and the flow in the porous layer using the Volume-Averaged Navier-Stokes equations. We imposed the momentum transfer conditions at the interface between the porous fluid region and the porous medium in order to couple the fluid velocity and pressure of the two layers. We derived the modal equations by exploiting the periodicity of the problem and by assuming that the disturbances depend on time through a complex exponential. We solved numerically the resulting generalized eigenvalue problem using the Chebyshev collocation spectral method, and we computed numerically the maximum value of the transient energy growth, G^{max} , by using the first K modes, ordered by decreasing imaginary part. We considered a channel bounded by two identical porous walls, and analyzed the effects of permeable walls for a single case, Reynolds number $Re = 500$, height of the porous layer $h_p = 1$, permeability $\sigma = 0.0155$, porosity $\varepsilon = 0.4$ and momentum transfer coefficient $\tau = 0$. We compared the results introducing the normalized amplification of G^{max} with respect to the Poiseuille flow, δG . Then, we focused on the wavenumber point $\alpha = 1.3$, $\beta = 0.7$, for which δG assumes the maximum value over the considered wavenumber space. Subsequently, we varied the permeability, momentum transfer coefficient and porosity with respect to the case above mentioned, and we analyzed how these parameters influence the behavior of the maximum of energy growth over the wavenumber space. To study the effects of the momentum transfer coefficient and porosity on non-modal stability, we varied also Reynolds number and permeability. Finally, we focused on the point $\alpha = 1.3$, $\beta = 0.7$ and we investigated the effects of the porous parameters on both the transient growth function and the magnitude of the optimal initial normal velocity.

For $Re = 500$, $h_p = 1$, $\sigma = 0.0155$, $\varepsilon = 0.4$, $\tau = 0$, we discovered that the wall permeability amplifies G^{max} over the wavenumber space $(\alpha, \beta) \in [0, 2] \times [0, 4]$, with respect to the Poiseuille flow. We observed that maximum of G^{max} , located at $\alpha = 0$,

$\beta = 2$, remains nearly unchanged, while for $\alpha = 1.3$ and $\beta = 0.7$ the relative amplification δG assumes the maximum value ($\approx 40\%$). For this special point, we computed the transient growth function and the optimal initial condition. We discovered that the number of modes K , used to compute accurately G^{max} , does not have to be as large as to include the modes associated to the Volume-Averaged Navier-Stokes equations and to the interface momentum transfer conditions. The optimal initial normal velocity profile involves deeply the porous layers while the optimal initial normal vorticity does not. Moreover, near the centerline of the channel the perturbation profiles are very similar to the ones of Poiseuille flow.

The permeability showed a considerable impact on G^{max} . When we lowered the permeability to $\sigma = 0.0065$, the maximum of the relative amplification δG significantly reduced to 7%. On the contrary, when we increased the permeability up to $\sigma = 0.02$ the flow became linearly unstable around the region where δG is max. Next, we analyzed the point $\alpha = 1.3$, $\beta = 0.7$, and we discovered that when we increase the permeability, we increase also the value of the optimal normal velocity assumed both at the interface and deeply into the porous layer.

The interface coefficient τ accounts for the distribution of the momentum at the boundary between the porous layer and the fluid region. Theoretically, Ochoa-Tapia and Whitaker estimated that $|\tau| \approx 1$ [29], however, this coefficient has to be determined experimentally. In our work, we ranged τ in the interval $[-1, 1]$ to estimate the error bar due to the uncertainty of τ . We discovered that τ has a weaker effect on G^{max} with respect to permeability. In particular, $\tau = -1$ nearly does not change G^{max} , with respect to the case computed with $\tau = 0$, while $\tau = 1$ locally diminish the maximum of the transient growth, for α sufficiently large. Also, we confirmed that the interface coefficient affects considerably the linear stability of our problem, as discovered by Tilton and Cortelezzi [51]. More precisely, $\tau = 1$ reduces the linearly unstable region in the wavenumber space, with respect to $\tau = -0$, while $\tau = -1$ negligibly extends such a region. Next, we analyzed the transient growth and the optimal initial condition for the point $\alpha = 1.3$, $\beta = 0.7$. The interface coefficient nearly does not vary G^{max} , however, for $\tau = 1$ the decay of $G(t)$ becomes faster. The optimal normal velocity profile shows that the interface coefficient does not change neither the velocity at the interface nor how deeply the perturbation penetrates into the porous layer.

We analyzed G^{max} computed using $\varepsilon = 0.3$ and $\varepsilon = 0.8$ and we found that porosity has a smaller influence with respect to the interface coefficient. For the streamwise wavenumber less than 0.5, the effects on G^{max} are negligible, while for the rest of the wavenumber space, there are different behaviors depending on the wavenumbers α and β . In particular, there are regions in which a high value of ε produces a higher value of G^{max} , with respect to $\varepsilon = 0.4$, and vice versa. We reported that for increasing permeability and Reynolds number, the effects of ε amplify. Also, we discovered that porosity is able to alter significantly the linear stability properties of our problem. More precisely, the linearly unstable region becomes significantly wider for increasing values of ε .

To solve our problem, we made the hypothesis that the inertial effects induced on the fluid motion through the porous structure, were negligible both at the interfaces and in the porous itself. Following Tilton and Cortelezzi [51], a criterion to establish the importance of the neglected terms is to check that $u_i < 0.05$, where u_i is the non-dimensional laminar velocity at the interface. For the majority of the cases discussed we satisfy to the above mentioned constraint. Exceptions are for $\tau = 1$ and $\varepsilon = 0.4$, when $\sigma = 0.0155, 0.02$. In these cases, we have $u_i = 0.069$ and $u_i = 0.096$, respectively. However, Costa *et al.* demonstrated experimentally that the inertial effects tend to growth gradually as permeability and volume-averaged velocity increase [14]. Therefore, it is not possible to define a critical value of u_i , and results should be considered in this view.

Our work showed that, depending on the wavenumbers α and β , the maximum energy growth of a flow through a channel with permeable and porous walls can be larger as 40% with respect to Poiseuille flow. The increment is associated to a significant flow across the interface between the porous layer and the fluid region. If perturbations grow enough such that non-linear terms become important, linear stability results may not be valid anymore, and in addition, transition to turbulence can occur. We could expect that our findings could contribute to the research devoted to the study of the mechanisms that trigger transition in flows over permeable walls. Moreover, we hope that our study could have technological implications in applications such as the laminar boundary layer control. Braslow reports the usage of perforated plates and wholly porous surfaces to implement suction of boundary layers in aeronautical test campaigns such as those performed at the NACA Langley Research center by Burrows and Visconti in the 1940s, and the experiments on the Vampire aircraft performed by the British Royal Aircraft Establishment [8]. Also, suction through a porous medium is actually implemented in a technology used for boundary layer control in wind tunnel testing [6]. We hope that our study could help to predict more accurately the transitional Reynolds number for porous wall-bounded flows, allowing for obtaining more reliable numerical results in projects in which the above mentioned technologies are involved, and therefore, diminishing the amount of expensive test campaigns.

Because of the huge dimension of the data that we have computed, in this work we have analyzed the effects of the porosity and of the interface coefficient separately, and moreover, we have considered only the case with $h_p = 1$. Future work should explore deeply the parameter space to investigate the effects on the transient growth of the parameters, when they vary simultaneously. Other possible extensions to our work could be a monotonic stability study, in order to determine the critical Reynolds number beyond which transient growth occurs, or to analyze the response to an external harmonic forcing, which can represent for example, wall-roughness, the input of an open-loop control system, terms neglected when modeling the problem. Future work could be also oriented to extend the model of channel flow over porous walls including the inertial effects,

allowing for considering higher permeability porous materials. Tilton estimated that for the cases considered in his work, the inertial effects become important at the interface, before than in the porous layers [49]. This suggests to model the flow through the porous layers using again the Volume-Averaged Naviers Stokes equations, and to modify only the momentum transfer conditions to include the inertial effects.

Bibliography

- [1] B. Alazmi and K. Vafai. Analysis of fluid flow and heat transfer interfacial conditions between a porous medium and a fluid layer. *International Journal of Heat and Mass Transfer*, 44(9):1735–1749, 2001.
- [2] J. Bear. *Dynamics of fluids in porous media*. Dover publications, 1988.
- [3] G.S. Beavers and D.D. Joseph. Boundary conditions at a naturally permeable wall. *J. Fluid Mech*, 30(1):197–207, 1967.
- [4] G.S. Beavers, E.M. Sparrow, and R.A. Magnuson. Experiments on coupled parallel flows in a channel and a bounding porous medium. *Journal of Basic Engineering*, 92:843, 1970.
- [5] GS Beavers, EM Sparrow, and DE Rodenz. Influence of bed size on the flow characteristics and porosity of randomly packed beds of spheres. *Journal of Applied Mechanics*, 40:655, 1973.
- [6] Jeroen Bink. Boundary layer control system for wind tunnels, Patent EP 2098848 A1.
- [7] John P Boyd. Chebyshev and fourier spectral methods. 2001. *Courier Dover*.
- [8] Albert L Braslow. A history of suction-type laminar-flow control with emphasis on flight research, 1999.
- [9] W. P. Breugem. *The influence of wall permeability on laminar and turbulent flows*. PhD thesis, Delft University of Technology, 2005.
- [10] WP Breugem and BJ Boersma. Direct numerical simulations of turbulent flow over a permeable wall using a direct and a continuum approach. *Physics of fluids*, 17:025103, 2005.
- [11] WP Breugem, BJ Boersma, and RE Uittenbogaard. The laminar boundary layer over a permeable wall. *Transport in porous media*, 59(3):267–300, 2005.
- [12] WP Breugem, BJ Boersma, and RE Uittenbogaard. The influence of wall permeability on turbulent channel flow. *Journal of Fluid Mechanics*, 562(1):35–72, 2006.

-
- [13] X. Chen, P. Yu, SH Winoto, and H.T. Low. A numerical method for forced convection in porous and homogeneous fluid domains coupled at interface by stress jump. *International journal for numerical methods in fluids*, 56(9):1705–1729, 2008.
- [14] UMS Costa, Jr JS Andrade, HA Makse, and HE Stanley. The role of inertia on fluid flow through disordered porous media. *Physica A: Statistical Mechanics and its Applications*, 266(1):420–424, 1999.
- [15] VAF Costa, LA Oliveira, and BR Baliga. Implementation of the stress jump condition in a control-volume finite-element method for the simulation of laminar coupled flows in adjacent open and porous domains. *Numerical Heat Transfer, Part B: Fundamentals*, 53(5):383–411, 2008.
- [16] H. Darcy. Les fontaines publiques de la ville de dijon, 1856. *Dalmont, Paris*, 70.
- [17] T. Giorgi. Derivation of the forchheimer law via matched asymptotic expansions. *Transport in porous media*, 29(2):191–206, 1997.
- [18] David Gottlieb, Steven A Orszag, and CAMBRIDGE HYDRODYNAMICS INC MA. *Numerical analysis of spectral methods*, volume 2. SIAM, 1977.
- [19] L Hårkan Gustavsson. Energy growth of three-dimensional disturbances in plane poiseuille flow. *Journal of Fluid Mechanics*, 224(1):241–260, 1991.
- [20] L Hårkan Gustavsson. Energy growth of three-dimensional disturbances in plane poiseuille flow. *Journal of Fluid Mechanics*, 224(1):241–260, 1991.
- [21] Seonghyeon Hahn, Jongdoo Je, and Haecheon Choi. Direct numerical simulation of turbulent channel flow with permeable walls. *Journal of Fluid Mechanics*, 450:259–286, 2002.
- [22] DD Joseph, DA Nield, and G. Papanicolaou. *Nonlinear equation governing flow in a saturated porous medium*. Defense Technical Information Center, 1981.
- [23] AV Kuznetsov. Analytical investigation of the fluid flow in the interface region between a porous medium and a clear fluid in channels partially filled with a porous medium. *Applied scientific research*, 56(1):53–67, 1996.
- [24] JL Lage. The fundamental theory of flow through permeable media from darcy to turbulence. *Transport phenomena in porous media*, pages 1–30, 1998.

-
- [25] M. Lesieur and O. Metais. New trends in large-eddy simulations of turbulence. *Annual Review of Fluid Mechanics*, 28(1):45–82, 1996.
- [26] F. Liu, BM Chen, and L. Wang. Experimental and numerical estimation of slip coefficient in a partially porous cavity. *Experimental Thermal and Fluid Science*, 2012.
- [27] Qianlong Liu and Andrea Prosperetti. Pressure-driven flow in a channel with porous walls. *Journal of Fluid Mechanics*, 679(1):77–100, 2011.
- [28] G. Neale and W. Nader. Practical significance of brinkman’s extension of darcy’s law: coupled parallel flows within a channel and a bounding porous medium. *The Canadian Journal of Chemical Engineering*, 52(4):475–478, 1974.
- [29] J.A. Ochoa-Tapia and S. Whitaker. Momentum transfer at the boundary between a porous medium and a homogeneous fluid—i. theoretical development. *International Journal of Heat and Mass Transfer*, 38(14):2635–2646, 1995.
- [30] J.A. Ochoa-Tapia and S. Whitaker. Momentum transfer at the boundary between a porous medium and a homogeneous fluid—ii. comparison with experiment. *International Journal of Heat and Mass Transfer*, 38(14):2647–2655, 1995.
- [31] JA Ochoa-Tapia and S. Whitaker. Momentum jump condition at the boundary between a porous medium and a homogeneous fluid: inertial effects. *Journal of Porous Media*, 1:201–218, 1998.
- [32] William M’F Orr. The stability or instability of the steady motions of a perfect liquid and of a viscous liquid. part ii: A viscous liquid. In *Proceedings of the Royal Irish Academy. Section A: Mathematical and Physical Sciences*, volume 27, pages 69–138. JSTOR, 1907.
- [33] Steven A Orszag. Accurate solution of the orr-sommerfeld stability equation. *J. Fluid Mech*, 50(4):689–703, 1971.
- [34] M. Quintard and S. Whitaker. Transport in ordered and disordered porous media i: The cellular average and the use of weighting functions. *Transport in Porous Media*, 14(2):163–177, 1994.
- [35] M. Quintard and S. Whitaker. Transport in ordered and disordered porous media ii: Generalized volume averaging. *Transport in porous media*, 14(2):179–206, 1994.
- [36] Lord Rayleigh. On the stability, or instability, of certain fluid motions. *Proceedings of the London Mathematical Society*, 1(1):57–72, 1879.

-
- [37] Satish C Reddy and Dan S Henningson. Energy growth in viscous channel flows. *Journal of Fluid Mechanics*, 252:209–209, 1993.
- [38] Satish C Reddy, Peter J Schmid, and Dan S Henningson. Pseudospectra of the orr-sommerfeld operator. *SIAM Journal on Applied Mathematics*, 53(1):15–47, 1993.
- [39] Osborne Reynolds. An experimental investigation of the circumstances which determine whether the motion of water shall be direct or sinuous, and of the law of resistance in parallel channels. *Proceedings of the Royal Society of London*, 35(224-226):84–99, 1883.
- [40] S. Richardson. A model for the boundary condition of a porous material. part 2. *J. Fluid Mech*, 49(2):327–336, 1971.
- [41] P.G. Saffman. On the boundary condition at the surface of a porous medium. *Stud. Appl. Math*, 50(2):93–101, 1971.
- [42] Peter J Schmid and Dan S Henningson. *Stability and transition in shear flows*, volume 142. Springer Verlag, 2001.
- [43] U. Shavit, R. Rosenzweig, and S. Assouline. Free flow at the interface of porous surfaces: a generalization of the taylor brush configuration. *Transport in porous media*, 54(3):345–360, 2004.
- [44] J.C. Slattery. *Momentum, energy, and mass transfer in continua*. RE Krieger Publishing Company, 1978.
- [45] Arnold Sommerfeld. Ein beitrag zur hydrodynamischen erklärung der turbulenten flüssigkeitsbewegungen. *Atti del*, 4:116–124, 1908.
- [46] Ephraim M Sparrow, GS Beavers, TS Chen, and JR Lloyd. Breakdown of the laminar flow regime in permeable-walled ducts. *Journal of Applied Mechanics*, 40:337, 1973.
- [47] H. Tan and K.M. Pillai. Finite element implementation of stress-jump and stress-continuity conditions at porous-medium, clear-fluid interface. *Computers & Fluids*, 38(6):1118–1131, 2009.
- [48] GI Taylor. A model for the boundary condition of a porous material. part 1. *Journal of Fluid Mechanics*, 49(02):319–326, 1971.
- [49] N. Tilton. *The Effects of Wall Permeability on the Linear Stability of Channel Flows and the Asymptotic Suction Boundary Layer*. PhD thesis, McGill University, 2009.

-
- [50] N. Tilton and L. Cortelezzi. The destabilizing effects of wall permeability in channel flows: A linear stability analysis. *Physics of Fluids*, 18(5):051702–051702, 2006.
- [51] N. Tilton and L. Cortelezzi. Linear stability analysis of pressure-driven flows in channels with porous walls. *Journal of Fluid Mechanics*, 604:411–446, 2008.
- [52] Lloydn Trefethen, Annee Trefethen, Satish Reddy, Tobina Driscoll, et al. Hydrodynamic stability without eigenvalues.
- [53] F.J. Valdés-Parada, B. Goyeau, and J.A. Ochoa-Tapia. Jump momentum boundary condition at a fluid–porous dividing surface: Derivation of the closure problem. *Chemical engineering science*, 62(15):4025–4039, 2007.
- [54] Claus Wagner and Rainer Friedrich. Dns of turbulent flow along passively permeable walls. *International journal of heat and fluid flow*, 21(5):489–498, 2000.
- [55] S. Whitaker. Advances in theory of fluid motion in porous media. *Industrial & Engineering Chemistry*, 61(12):14–28, 1969.
- [56] S. Whitaker. Flow in porous media i: A theoretical derivation of darcy’s law. *Transport in porous media*, 1(1):3–25, 1986.
- [57] S. Whitaker. The forchheimer equation: a theoretical development. *Transport in Porous media*, 25(1):27–61, 1996.
- [58] D.C. Wilcox. *Turbulence modeling for CFD*, volume 3. DCW industries La Cañada, CA, 2006.
- [59] P. Yu, TS Lee, Y. Zeng, and HT Low. A numerical method for flows in porous and homogenous fluid domains coupled at the interface by stress jump. *International journal for numerical methods in fluids*, 53(11):1755–1775, 2007.
- [60] Quan Zhang and Andrea Prosperetti. Pressure-driven flow in a two-dimensional channel with porous walls. *Journal of Fluid Mechanics*, 631:1, 2009.

